Effective QCD and transport description of dilepton and photon production in heavy-ion collisions and elementary processes

O. Linnyk[a], E. L. Bratkovskaya[b], W. Cassing[a]

[a] *Institut für Theoretische Physik, Justus Liebig Universität Giessen, 35392 Giessen, Germany*
[b] *Institut für Theoretische Physik, Goethe Universität Frankfurt am Main, 60438 Frankfurt am Main, Germany*

arXiv:1512.08126v1 [nucl-th] 26 Dec 2015

Abstract

In this review we address the dynamics of relativistic heavy-ion reactions and in particular the information obtained from electromagnetic probes that stem from the partonic and hadronic phases. The out-of-equilibrium description of strongly interacting relativistic fields is based on the theory of Kadanoff and Baym. For the modeling of the partonic phase we introduce an effective dynamical quasiparticle model (DQPM) for QCD *in equilibrium*. In the DQPM, the widths and masses of the dynamical quasiparticles are controlled by transport coefficients that can be compared to the corresponding quantities from lattice QCD. The resulting off-shell transport approach is denoted by Parton-Hadron-String Dynamics (PHSD) which includes covariant dynamical transition rates for hadronization and keeps track of the hadronic interactions in the final phase. It is shown that the PHSD captures the bulk dynamics of heavy-ion collisions from lower SPS to LHC energies and thus provides a solid basis for the evaluation of the electromagnetic emissivity on the basis of the same dynamical parton propagators that are employed for the dynamical evolution of the partonic system. The production of *direct* photons in elementary processes and heavy-ion reactions is discussed and the present status of the photon v_2 "puzzle" – a large elliptic flow v_2 of the *direct* photons experimentally observed in heavy-ion collisions - is addressed for nucleus-nucleus reactions at RHIC and LHC energies. The role of hadronic and partonic sources for the photon spectra and the flow coefficients v_2 and v_3 are considered as well as the possibility to subtract the QGP signal from the experimental observables. Furthermore, the production of e^+e^- or $\mu^+\mu^-$ pairs in elementary processes and A+A reactions is addressed. The calculations within the PHSD from SIS to LHC energies show an increase of the low mass dilepton yield essentially due to the in-medium modification of the ρ-meson and at the lowest energy also due to a multiple regeneration of Δ-resonances. Furthermore, pronounced traces of the partonic degrees-of-freedom are found in the intermediate dilepton mass regime (1.2 GeV $< M <$ 3 GeV) at relativistic energies, which will also shed light on the nature of the very early degrees-of-freedom in nucleus-nucleus collisions.

Keywords: QCD, Quasi-particle models, Photons, Dileptons, Heavy-Ion collisions

Contents

1 Introduction **2**

2 Relativistic dynamics of many-body systems and off-shell transport **4**
2.1 Two-point functions 4
2.2 The Dyson-Schwinger equation 5
2.3 Kadanoff-Baym equations 6
2.4 Spectral function 7
2.5 The equilibrium distribution 8
2.6 Derivation of the off-shell relativistic transport theory 8
2.7 Test-particle representation and numerical solution 11

3 Dynamical quasiparticle model for hot QCD **12**
3.1 Quasiparticle properties 13
3.2 Spectral functions 14
3.3 Thermodynamics of QCD 15

3.4 Partonic mean-field potentials from the DQPM . . . 16
3.5 DQPM at finite quark chemical potential . . . 16

4 The PHSD approach 17
4.1 Hadronization . . . 17
4.2 Initial conditions . . . 19
4.3 System evolution . . . 19
4.4 Transport coefficients of the QGP . . . 21
4.5 Application to Au+Au or Pb+Pb collisions . . . 25

5 Implementation of photon and dilepton production in transport approaches 31
5.1 Photon sources in relativistic heavy-ion collisions . . . 31
5.2 Photon production by dynamical quasiparticles in the QGP . . . 33
5.3 Thermal rates and the Landau-Migdal-Pomeranchuk effect . . . 36
5.4 Bremsstrahlung $m + m \to m + m + \gamma$ beyond the soft-photon approximation . . . 38
5.5 Binary meson+meson and meson+nucleon reactions . . . 45
5.6 Dilepton sources . . . 47
5.7 Vector-meson spectral functions . . . 47
5.8 Off-shell propagation and the time-integration method . . . 48
5.9 e^+e^- bremsstrahlung in $p + p$ and $p + n$ reactions . . . 50

6 Results on photon production in $p + A$ and $A + A$ collisions 51
6.1 Direct photon spectra from SPS to LHC energies . . . 53
6.2 Elliptic flow of *direct* photons . . . 57
6.3 Triangular flow of direct photons . . . 63

7 Results on dilepton production in heavy-ion collisions 65
7.1 SIS energies . . . 65
7.2 AGS energies . . . 68
7.3 SPS energies . . . 68
7.4 RHIC energies . . . 69
7.5 LHC energies . . . 70

8 Summary 72

1. Introduction

Present experiments at the Relativistic Heavy-Ion Collider (RHIC) or the Large Hadron Collider (LHC) have reached for short time scales the conditions met in the first micro-seconds in the evolution of the universe after the 'Big Bang'. The 'Big Bang' scenario implies that on these time scales the entire state has emerged from a partonic system of quarks, antiquarks and gluons – a quark-gluon plasma (QGP) – to color neutral hadronic matter consisting of interacting hadronic states (and resonances) in which the partonic degrees-of-freedom are confined. The nature of confinement and the dynamics of this phase transition is still an outstanding question of today's physics. Early concepts of the QGP were guided by the idea of a weakly interacting system of massless partons which might be described by perturbative QCD (pQCD). However, experimental observations at RHIC and LHC indicated that the new medium created in ultra-relativistic heavy-ion collisions is interacting more strongly than hadronic matter. It is presently widely accepted that this medium is an almost perfect liquid of partons as suggested experimentally from the strong radial expansion and the scaling of the elliptic flow $v_2(p_T)$ of mesons and baryons with the number of constituent quarks and antiquarks. While the last years have been devoted to explore the collective and transport properties of this partonic medium, the present focus lies on the electromagnetic emissivity of the new type of matter, i.e. its emission of *direct* photons or dilepton pairs. Since the system is initially far from equilibrium and no clear evidence has been achieved so far that an early equilibration at times of the order of 0.5 - 1.0 fm/c is achieved, microscopic studies based on non-equilibrium dynamics are mandatory.

Non-equilibrium many-body theory or transport theory has become a major topic of research in nuclear physics, in cosmological particle physics as well as condensed matter physics. The multidisciplinary aspect arises due to a common interest to understand the various relaxation phenomena of quantum dissipative systems. Important questions in nuclear and particle physics at the highest energy densities are: i) how do nonequilibrium systems in extreme environments evolve, ii) how do they eventually thermalize, iii) how phase transitions occur in real time with possibly nonequilibrium remnants? The dynamics of heavy-ion collisions at various bombarding energies provide the laboratory of choice for research on nonequilibrium quantum many-body physics and relativistic quantum-field theories, since the initial state of a collision resembles an extreme non-equilibrium configuration while the final state might even exhibit a certain degree of thermalization.

Especially the powerful method of the 'Schwinger-Keldysh' [1, 2, 3, 4, 5] or 'closed time path' (CTP) real-time Greens functions – being the essential degrees-of-freedom – has been shown to provide an appropriate basis for the formulation of the complex problems in the various areas of nonequilibrium quantum many-body physics. Within this framework one can derive valid approximations - depending, of course, on the problem under consideration - by preserving overall consistency relations. Originally, the resulting causal Dyson-Schwinger equation of motion for the one-particle Greens functions (or two-point functions), i.e. the Kadanoff-Baym (KB) equations [6], have served as the underlying scheme for deriving various transport phenomena and generalized transport equations. For review articles on the Kadanoff-Baym equations in the various areas of nonequilibrium quantum physics we refer the reader to Refs. [7, 8, 9, 10, 11, 12, 13].

On the other hand, kinetic transport theory is a convenient tool to study many-body nonequilibrium systems, non-relativistic or relativistic. Kinetic equations, which do play the central role in more or less all practical simulations, can be derived from KB equations within suitable approximations. Hence, a major impetus in the past has been to derive semi-classical Boltzmann-like transport equations within the standard quasi-particle approximation. Additionally, off-shell extensions by means of a gradient expansion in the space-time inhomogeneities - as already introduced by Kadanoff and Baym [6] - have been formulated for various directions in physics: from a relativistic electron-photon plasma [14] to the transport of nucleons at intermediate heavy-ion reactions [15], for transport of particles in scalar Φ^4-theory [12, 16] to the transport of partons in high-energy heavy-ion reactions [17, 18, 19, 20, 21, 22]. We recall that on the formal level of the KB-equations the various forms assumed for the self-energy have to fulfill consistency relations in order to preserve symmetries of the fundamental Lagrangian [6, 23, 24]. This allows also for a unified treatment of stable and unstable (resonance) particles. In this review we will briefly sketch the derivation of the KB equations and of the off-shell transport equations in first-order gradient expansion in Section 2.

The perspectives to solve QCD in Minkowski space for out of equilibrium configurations and non-vanishing quark densities will be very low also in the next years such that effective approaches are necessary to model the dominant properties of QCD in equilibrium, i.e. the thermodynamic quantities as well as transport coefficients. To this aim the dynamical quasiparticle model (DQPM) has been introduced which is based on partonic propagators with sizeable imaginary parts (or broad spectral functions). We will briefly recall the basic definitions in the DQPM and its results for the QCD equation of state in Section 3.

By merging off-shell transport theory (Section 2) and the DQPM (Section 3) we obtain the Parton-Hadron-String-Dynamics (PHSD) transport approach that incorporates additionally a dynamical transition from partonic to hadronic degrees-of-freedom without violating the second law of thermodynamics (Section 4). This approach will provide the background dynamics for the study of the electromagnetic emissivity from relativistic heavy-ion collisions. Before proceeding to the actual results on the photon and dilepton production, the PHSD calculations are first confronted with differential hadron spectra and single-particle collective flow coefficients v_2 and v_3 of charged hadrons produced in heavy-ion collisions from the lower Super-Proton-Synchrotron (SPS) to LHC energies.

Section 5 is devoted to the implementation of the photon and dilepton production channels in a non-equilibrium off-shell transport approach and the computation of the individual production cross sections. The radiation from the interactions of the broad quasiparticles as effective degrees-of-freedom in the QGP is calculated, thus employing the same effective propagators in the evaluation of the electromagnetic radiation as used for the time evolution of the partonic system. Additionally, electromagnetic radiation by hadron decays and their mutual interactions is implemented for an extended number of hadronic species. In particular, the photon production in the bremsstrahlung processes such as $\pi + \pi \to \pi + \pi + \gamma$ is calculated beyond the soft-photon approximation (SPA) using the full cross sections within a one-boson-exchange (OBE) model.

In Section 6, we present the results on the production of real photons in heavy-ion reactions where we will

focus on the transverse momentum spectra (at midrapidity) and the collective flow of the *direct* photons in order to shed some light on the present "photon v_2 puzzle". Results from PHSD for the triangular flow v_3 at RHIC and LHC energies will be presented, too. In Section 7, we continue with the production of dilepton pairs from elementary and heavy-ion collisions from SIS up to LHC energies. Special attention here is paid to the low-mass enhancement of the dilepton pairs (0.2 GeV$< M <$ 0.7 GeV) and to the intermediate mass range (1.2 GeV $< M <$ 3 GeV) in order to explore the possible contribution from a QGP phase and/or in-medium modifications of vector mesons in the hadronic phase. A summary in Section 8 completes this review.

2. Relativistic dynamics of many-body systems and off-shell transport

Relativistic formulations of the many-body problem are essentially described within covariant field theory. Since the fields themselves are distributions in space-time $x = (t, \mathbf{x})$ one uses the Heisenberg picture for convenience. In the Heisenberg picture the time evolution of the system is described by time-dependent operators that are evolved with the help of the time-evolution operator $\hat{U}(t, t')$ which follows

$$i\frac{\partial \hat{U}(t,t_0)}{\partial t} = \hat{H}(t)\hat{U}(t,t_0), \tag{1}$$

with $\hat{H}(t)$ denoting the Hamilton operator of the system at time t. Eq. (1) is formally solved by

$$\hat{U}(t,t_0) = T\left(\exp\left[-i\int_{t_0}^{t} \mathrm{d}z\ \hat{H}(z)\right]\right) = \sum_{n=0}^{\infty} \frac{T[-i\int_{t_0}^{t}\mathrm{d}z\ \hat{H}(z)]^n}{n!}, \tag{2}$$

where T denotes the time-ordering operator, which is also denoted as Dyson series. Let's assume that the initial state is given by some density matrix $\hat{\rho}$, which may be a pure or mixed state, then the time evolution of any operator $\hat{O}$ in the Heisenberg picture from time t_0 to t is given by

$$O(t) = \langle \hat{O}_H(t)\rangle = \mathrm{Tr}\left(\hat{\rho}\,\hat{O}_H(t)\right) = \mathrm{Tr}\left(\hat{\rho}\,\hat{U}(t_0,t)\hat{O}\,\hat{U}(t,t_0)\right) = \mathrm{Tr}\left(\hat{\rho}\,\hat{U}^\dagger(t,t_0)\hat{O}\,\hat{U}(t,t_0)\right). \tag{3}$$

Eq. (3) implies that first the system is evolved from t_0 to t and then backward from t to t_0. This may be expressed as a time integral along the (Keldysh-)contour shown in Fig. 1.

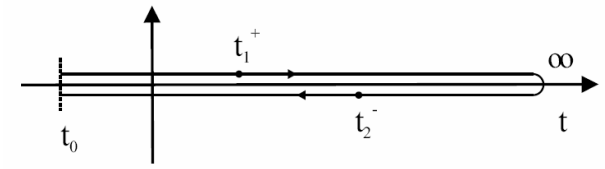


Figure 1: The Keldysh-contour for the time integration in the Heisenberg picture.

2.1. Two-point functions

Now Green functions on the Keldysh-contour may have time arguments on the same branch of the contour or on opposite branches. This gives four possibilities for the Green functions defined – in case of a field theory with only scalar fields $\phi(x)$ (for sake of illustration) – by

$$iG^c(x,y) = iG^{++}(x,y) = \langle\, \hat{T}^c(\phi(x)\phi(y))\,\rangle \tag{4}$$
$$iG^<(x,y) = iG^{+-}(x,y) = \langle\phi(y)\phi(x)\rangle \tag{5}$$
$$iG^>(x,y) = iG^{-+}(x,y) = \langle\phi(x)\phi(y)\rangle \tag{6}$$
$$iG^a(x,y) = iG^{--}(x,y) = \langle\, \hat{T}^a(\phi(x)\phi(y))\,\rangle\,, \tag{7}$$

which are not independent! Here $x = (x^0, \mathbf{x})$ and $y = (y^0, \mathbf{y})$. Time-ordering has to be fulfilled if both time arguments are on the same axis. The causal time-ordering operator T^c places fields at later times to the left

while the anticausal operator T^a places fields at later times to the right. The Green functions $G^>$ and $G^<$ are denoted as **Wightman functions** and will play the essential role in the dynamical description of the system. One may also write the Green function on the Keldysh-contour in terms of a 2x2 matrix

$$G(x,y) = \begin{array}{c} \\ + \\ - \end{array} \begin{array}{c} \begin{array}{cc} + & - \end{array} \\ \begin{pmatrix} G^c(x,y) & G^<(x,y) \\ G^>(x,y) & G^a(x,y) \end{pmatrix} \end{array}. \tag{8}$$

Note that the Green functions defined in Eqs. (4) to (7) are two-point functions, i.e. they correspond to a single-particle degree-of-freedom!

The further derivation starts with the Dyson equation for $G(x,y)$,

$$G(x,y) = G_0(x,y) + [G_0 \Sigma G](x,y), \tag{9}$$

with $G_0(x,y)$ denoting the bare Green function. The selfenergy $\Sigma(x,y)$ has the meaning of a one-body mean-field potential and in lowest order for fermions is given by the Hartree-Fock potential ($\times 2M$) since in the relativistic case Σ has the dimension [energy]^2.

The relation to the one-body density matrix ρ - as employed in density-matrix theory [25] - is given by

$$\rho(\mathbf{x},\mathbf{x}';t) = iG^<(\mathbf{x},\mathbf{x}';t,t), \tag{10}$$

since the time diagonal Green function can be identified with an integral over the energy variable ω using

$$G^<(\mathbf{x},\mathbf{x}';\omega,t) = \int_{-\infty}^{\infty} d(\tau-\tau')\ \exp(i\omega(\tau-\tau'))\ G^<(\mathbf{x},\mathbf{x}';\tau,\tau') \tag{11}$$

(for $t = (\tau+\tau')/2$), i.e.

$$G^<(\mathbf{x},\mathbf{x}';t) = \int_{-\infty}^{\infty} \frac{d\omega}{2\pi}\ G^<(\mathbf{x},\mathbf{x}';\omega,t). \tag{12}$$

Two-point functions F on the closed-time-path (CTP) generally can be expressed by retarded and advanced components as

$$\begin{aligned} F^R(x,y) &= F^c(x,y) - F^<(x,y) = F^>(x,y) - F^a(x,y), \\ F^A(x,y) &= F^c(x,y) - F^>(x,y) = F^<(x,y) - F^a(x,y) \end{aligned} \tag{13}$$

giving in particular the relation

$$F^R(x,y) - F^A(x,y) = F^>(x,y) - F^<(x,y). \tag{14}$$

Note that the advanced and retarded components of the Green functions only contain spectral and no statistical information,

$$G^{R/A}(x,y) = G_0(x,y)\ \delta(t_1-t_2) \pm \Theta(\pm(t_1-t_2))\ [G^>(x,y) - G^<(x,y)]. \tag{15}$$

2.2. The Dyson-Schwinger equation

The Dyson-Schwinger equation (9) on the closed-time path reads in matrix form:

$$\begin{pmatrix} G^c(x,y) & G^<(x,y) \\ G^>(x,y) & G^a(x,y) \end{pmatrix} = \begin{pmatrix} G_0^c(x,y) & G_0^<(x,y) \\ G_0^>(x,y) & G_0^a(x,y) \end{pmatrix} +$$

$$\begin{pmatrix} G_0^c(x,x') & G_0^<(x,x') \\ G_0^>(x,x') & G_0^a(x,x') \end{pmatrix} \odot \begin{pmatrix} \Sigma^c(x',y') & -\Sigma^<(x',y') \\ -\Sigma^>(x',y') & \Sigma^a(x',y') \end{pmatrix} \odot \begin{pmatrix} G^c(y',y) & G^<(y',y) \\ G^>(y',y) & G^a(y',y) \end{pmatrix}, \tag{16}$$

where the symbol $\odot$ stands for an intermediate integration over space-time on the CTP, i.e. x' or y'. The selfenergy Σ on the CPT is defined along Eq. (13) and incorporates interactions of higher order. In lowest order $\Sigma/2M$ is given by the Hartree or Hartree-Fock mean-field in the non-relativistic limit (in case of fermions) but it follows a nonperturbative expansion [7].

2.3. Kadanoff-Baym equations

To derive the **Kadanoff-Baym equations** one multiplies Eq. (16) with the inverse free Green function (operator) $G_{0x}^{-1} = -(\partial_\mu^x \partial_x^\mu + m^2)$ from the left. This gives four equations which can be cast into the form:

$$-(\partial_\mu^x \partial_x^\mu + m^2) G^{R/A}(x,y) = \delta(x-y) + \Sigma^{R/A}(x,x') \odot G^{R/A}(x',y), \tag{17}$$

$$-(\partial_\mu^x \partial_x^\mu + m^2) G^{<}(x,y) = \Sigma^{R}(x,x') \odot G^{<}(x',y) + \Sigma^{<}(x,x') \odot G^{A}(x',y), \tag{18}$$

$$-(\partial_\mu^x \partial_x^\mu + m^2) G^{>}(x,y) = \Sigma^{R}(x,x') \odot G^{>}(x',y) + \Sigma^{>}(x,x') \odot G^{A}(x',y). \tag{19}$$

The propagation of the Green functions in the variable y is defined by the adjoint equations:

$$-(\partial_\mu^y \partial_y^\mu + m^2) G^{R/A}(x,y) = \delta(x-y) + G^{R/A}(x,x') \odot \Sigma^{R/A}(x',y), \tag{20}$$

$$-(\partial_\mu^y \partial_y^\mu + m^2) G^{<}(x,y) = G^{R}(x,x') \odot \Sigma^{<}(x',y) + G^{<}(x,x') \odot \Sigma^{A}(x',y), \tag{21}$$

$$-(\partial_\mu^y \partial_y^\mu + m^2) G^{>}(x,y) = G^{R}(x,x') \odot \Sigma^{>}(x',y) + G^{>}(x,x') \odot \Sigma^{A}(x',y). \tag{22}$$

Note again that the evolution of the retarded/advanced Green functions only depends on retarded/advanced quantities.

Definition of selfenergies

For the solution of the KB equations the computation/fixing of the (two-point) selfenergies Σ is mandatory. In the context of field theory the latter is extracted from the effective action

$$\Gamma[G] = \Gamma^0[G_0] + \frac{i}{2}[\ln(1 - G_0\Sigma) + G\Sigma] + \Phi[G] \tag{23}$$

assuming a vanishing vacuum expectation value $\langle 0|\phi(x)|0\rangle$. Here $\Gamma^0[G_0]$ only depends on the free Green function G_0 and can be considered as constant in the following. Note that all internal and external integrations in (23) have to be performed over the CTP. In $\Phi[G]$ all closed two-particle irreducible (2PI) diagrams are included in lowest (nontrivial) order. We recall that 2PI diagrams are those that cannot be separated in two disjunct diagrams by cutting two propagator lines; formally this implies that after second order differentiation with respect to G no separate diagrams survive.

For the derivation of selfenergies one now considers the variation of the action $\Gamma[G]$ with respect to G requiring $\delta\Gamma = 0$,

$$\delta\Gamma = 0 = \frac{i}{2}\Sigma\,\delta G - \frac{i}{2}\frac{G_0}{1 - G_0\,\Sigma}\delta\Sigma + \frac{i}{2}G\,\delta\Sigma + \delta\Phi = \frac{i}{2}\Sigma\,\delta G - \frac{i}{2}\underbrace{\frac{1}{G_0^{-1} - \Sigma}}_{=G}\delta\Sigma + \frac{i}{2}G\,\delta\Sigma + \delta\Phi = \frac{i}{2}\Sigma\,\delta G + \delta\Phi. \tag{24}$$

$$\Rightarrow \Sigma = 2i\frac{\delta\Phi}{\delta G}. \tag{25}$$

The selfenergies thus are obtained by opening of a propagator-line in the irreducible diagrams Φ. Note that this definition of the selfenergy preserves all conservation laws of the theory (as well as causality) and does not introduce additional conserved currents. In principle the Φ-functional includes irreducible diagrams up to infinite order, but here we will consider only the contributions up to second order in the coupling (2PI). For our present purpose this approximation is sufficient since we include the leading mean-field effects as well as the leading order scattering processes that pave the way to thermalization.

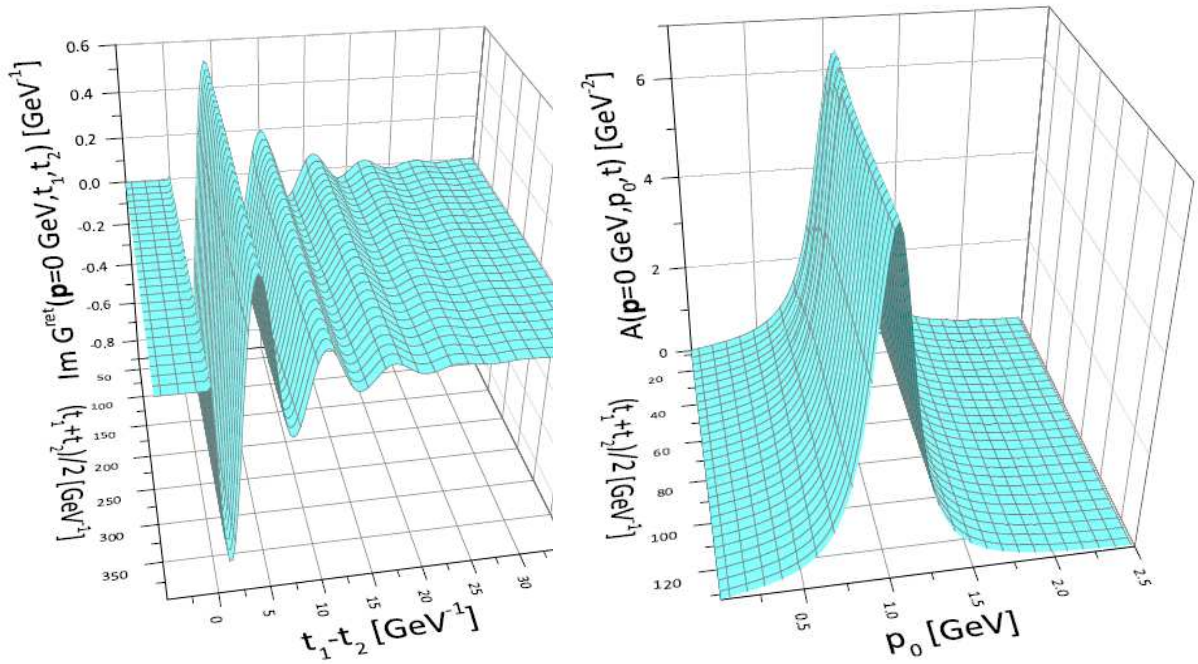


Figure 2: (l.h.s.) The imaginary part of the retarded Green function as a function of $t_1 - t_2$ and the average time $(t_1 + t_2)/2$ for ϕ^4 -theory in strong coupling as emerging from the Kadanoff-Baym approach (cf. Ref. [26]. (r.h.s.) The Fourier transform (28) in energy p_0 for the momentum mode $\mathbf{p} = 0$ is displayed on the l.h.s. in case of ϕ^4-theory for strong coupling.

2.4. Spectral function

The spectral function of the fields ϕ is of particular interest since it follows from the field commutator at unequal times and reflects the quantization of the theory. For scalar, symmetric fields ϕ it is given by

$$A(x,y) = \langle\, [\phi(x), \phi(y)]_- \,\rangle = i[G^>(x,y) - G^<(x,y)] = i[G^R(x,y) - G^A(x,y)]. \tag{26}$$

For homogenous systems in space we have in momentum-time representation

$$A(\mathbf{p}, t_1, t_2) = i[G^>(\mathbf{p}, t_1, t_2) - G^<(\mathbf{p}, t_1, t_2)] = i\left[-[G^<(\mathbf{p}, t_1, t_2)]^* - G^<(\mathbf{p}, t_1, t_2)\right]. \tag{27}$$

The quantity (27) is displayed in Fig. 2 (l.h.s.) as a function of $\Delta t = t_1 - t_2$ and $t = (t_1 + t_2)/2$ for a low lying momentum mode in case of the ϕ^4-theory for strong coupling λ as evaluted numerically in Ref. [26]. We observe a damped oscillation in Δt (for $\Delta t \geq 0$) in all cases with characteristic time scale $1/\gamma$ which practically does not depend on the average time t. This pattern is very similar for all momentum modes (cf. Ref. [26]).

The spectral function in energy-momentum representation is obtained by Fourier transformation with respect to the time difference $\Delta t = (t_1 - t_2)$ for each average time t:

$$A(\mathbf{p}, p_0, t) = \int_{-\infty}^{\infty} d\Delta t \;\; \exp(i\Delta t\, p_0) A(\mathbf{p}, t_1 = t + \Delta t/2, t_2 = t - \Delta t/2). \tag{28}$$

Since the spectral function essentially shows a damped oscillation in $t_1 - t_2$ (cf. Fig. 2, l.h.s.)) this implies that the Fourier transform (28) is of relativistic Breit-Wigner shape with a width γ that describes the decay in the relative time Δt (r.h.s. of Fig. 2). The spectral shape can be well approximated by

$$A(p_0, \mathbf{p}) \;= \frac{\gamma}{2\tilde{E}}\left(\frac{1}{(p_0 - \tilde{E})^2 + \gamma^2} - \frac{1}{(p_0 + \tilde{E})^2 + \gamma^2}\right) = \frac{2p_0\gamma}{(p_0^2 - \mathbf{p}^2 - M^2)^2 + 4\gamma^2 p_0^2} \tag{29}$$

with $\tilde{E}^2 = \mathbf{p}^2 + M^2 - \gamma^2$ where M denotes the mass of the degrees-of-freedom. We will come back to this functional form in Section 3.

2.5. The equilibrium distribution

Now we introduce the energy and momentum-dependent distribution function $N(\mathbf{p}, p_0, \bar{t})$ at any system time $\bar{t}$ in case of scalar bosons by the definition

$$\begin{aligned} i\,G^{<}(\mathbf{p}, p_0, \bar{t}) &= A(\mathbf{p}, p_0, \bar{t})\;\; N(\mathbf{p}, p_0, \bar{t})\,, \\ i\,G^{>}(\mathbf{p}, p_0, \bar{t}) &= A(\mathbf{p}, p_0, \bar{t})\,[\,N(\mathbf{p}, p_0, \bar{t}) + 1\,]\,, \end{aligned} \tag{30}$$

since $G^{<}(\mathbf{p}, p_0, \bar{t})$ and $G^{>}(\mathbf{p}, p_0, \bar{t})$ are known from the integration of the Kadanoff-Baym equations as well as $A(\mathbf{p}, p_0, \bar{t})$. In equilibrium (at temperature T) the Green functions obey the Kubo-Martin-Schwinger relation (KMS) for all momenta $\mathbf{p}$,

$$G^{>}_{eq}(\mathbf{p}, p_0) \;=\; e^{p_0/T}\; G^{<}_{eq}(\mathbf{p}, p_0) \qquad\qquad \forall\;\; \mathbf{p}\,. \tag{31}$$

If there exists a conserved quantum number in the theory we have, furthermore, a contribution of the corresponding chemical potential in the exponential function which leads to a shift of arguments: $p_0/T \to (p_0 - \mu)/T$. In case of ϕ^4-theory, however, there is no conserved quantum number and thus the equilibrium state has $\mu = 0$.

From the KMS condition of the Green functions (31) the equilibrium form of the distribution function (30) at temperature T is obtained as

$$N_{eq}(\mathbf{p}, p_0) \;=\; N_{eq}(p_0) \;=\; \frac{1}{e^{p_0/T} - 1} \;=\; N_{bose}(p_0/T)\,, \tag{32}$$

from

$$\frac{G^{<}}{G^{>}} = e^{-p_0/T} = \frac{N_{eq}}{N_{eq} + 1},$$

which is the well-known Bose distribution. As is obvious from Eq. (32) the equilibrium distribution can only be a function of energy p_0 and not of the momentum variable $\mathbf{p}$ in addition [26].

2.6. Derivation of the off-shell relativistic transport theory

Formal derivations of off-shell transport equations have been presented more than 50 years ago by Kadanoff and Baym [6] but actual solutions have barely been addressed [27, 28]. This Subsection is devoted to a brief derivation of generalized transport equations in first order gradient expansion including a generalized test-particle ansatz for the solution of the off-shell transport equation following Ref. [29].

The derivation of generalized transport equations starts by rewriting the Kadanoff-Baym equation for the Wightman functions in coordinate space ($x_1 = (t_1, \mathbf{x}_1), x_2 = (t_2, \mathbf{x}_2)$) (18) as

$$[\,\partial^{\mu}_{x_1}\partial^{x_1}_{\mu} + m^2 + \Sigma^{\delta}(x_1)\,]\;\; iG^{\lessgtr}(x_1, x_2) \;=\; i\,I_1^{\lessgtr}(x_1, x_2), \tag{33}$$

where the collision terms on the r.h.s. of Eq. (33) are given in $D = d + 1$ space-time dimensions by convolution integrals over coordinate-space selfenergies and Green functions:

$$I_1^{\lessgtr}(x_1, x_2) = -\int_{t_0}^{t_1} d^D z\;\; \left[\Sigma^{>}(x_1, z) - \Sigma^{<}(x_1, z)\right] G^{\lessgtr}(z, x_2) + \int_{t_0}^{t_2} d^D z \Sigma^{\lessgtr}(x_1, z)\left[G^{>}(z, x_2) - G^{<}(z, x_2)\right]. \tag{34}$$

In the general case of an arbitrary (scalar) quantum field theory Σ^{δ} is the local (non-dissipative tadpole) part of the path self-energy while $\Sigma^{\lessgtr}$ resemble the non-local collisional self-energy contributions. In the representation (34) the integration boundaries are exclusively given for the time coordinates, while the integration over the spatial coordinates extends over the whole spatial volume from $-\infty$ to $+\infty$ in d dimensions.

Since transport theories are formulated in phase-space one changes to the Wigner representation via Fourier transformation with respect to the rapidly varying ('intrinsic') relative coordinate $\Delta x = x_1 - x_2$ and treats the system evolution in terms of the ('macroscopic') mean space-time coordinate $x = (x_1 + x_2)/2$ and the four-momentum $p = (p_0, \mathbf{p})$. The functions in Wigner space are obtained as

$$\bar{F}(p, x) \;=\; \int_{-\infty}^{\infty} d^D \Delta x \;\;\; e^{+i\,\Delta x_{\mu}\,p^{\mu}} \;\; F(x_1 = x + \Delta x/2,\, x_2 = x - \Delta x/2)\,. \tag{35}$$

For the formulation of transport theory in the Wigner representation we have to focus not only on the transformation properties of ordinary two-point functions as given in Eq. (35), but also of convolution integrals as appearing in Eq. (34). A convolution integral in D dimensions (for arbitrary functions F, G),

$$H(x_1, x_2) \;=\; \int_{-\infty}^{\infty} d^D z \; F(x_1, z) \; G(z, x_2) \tag{36}$$

transforms as

$$\begin{aligned} \bar{H}(p,x) \;&=\; \int_{-\infty}^{\infty} d^D\Delta x \;\; e^{+i\,\Delta x_\mu\, p^\mu} \;\; H(x_1,x_2) = \int_{-\infty}^{\infty} d^D\Delta x \;\; e^{+i\,\Delta x_\mu\, p^\mu} \;\; \int_{-\infty}^{\infty} d^D z \;\; F(x_1,z) \;\; G(z,x_2) \\ &=\; e^{+i\,\frac{1}{2}\,(\partial_p^\mu\cdot\,\partial_\mu^{x'} \,-\, \partial_x^\mu\cdot\,\partial_\mu^{p'})} \;\; \left[\; \bar{F}(p,x) \;\; \bar{G}(p',x')\right]\Big|_{x'=x,\; p'=p} . \end{aligned} \tag{37}$$

In accordance with the standard assumption of transport theory we assume that all functions only smoothly evolve in the mean space-time coordinates and thus restrict to first order derivatives. All terms proportional to second or higher order derivatives in the mean space-time coordinates (also mixed ones) will be dropped. Thus the Wigner transformed convolution integrals (36) are given in *first order gradient approximation* by,

$$\bar{H}(p,x) \;=\; \bar{F}(p,x) \;\; \bar{G}(p,x) \;+\; i\,\frac{1}{2}\,\{\,\bar{F}(p,x)\,,\,\bar{G}(p,x)\,\} \;+\; \mathcal{O}(\partial_x^2)\,, \tag{38}$$

using the relativistic generalization of the Poisson bracket

$$\{\,\bar{F}(p,x)\,,\,\bar{G}(p,x)\,\} \;:=\; \partial_\mu^p\,\bar{F}(p,x)\cdot\partial_x^\mu\,\bar{G}(p,x) \;-\; \partial_x^\mu\,\bar{F}(p,x)\cdot\partial_\mu^p\,\bar{G}(p,x)\;. \tag{39}$$

In order to obtain the dynamics for the spectral functions within the approximate (first order gradient) scheme we start with the Dyson-Schwinger equations for the retarded and advanced Green functions in coordinate space (17). – Note that the convolution integrals in (17) extend over the whole space and time range in contrast to the equations of motion for the Wightman functions given in Eqs. (18) and (19)! – The further procedure consists in the following steps:
i) First we transform the above equations into the Wigner representation and apply the first order gradient approximation. In this limit the convolution integrals yield the product terms and the general Poisson bracket of the selfenergies and the Green functions $\{\,\Sigma^{R/A}, G^{R/A}\,\}$. We, further on, represent both equations in terms of real quantities by the decomposition of the retarded and advanced Green functions and selfenergies as

$$\begin{aligned} \bar{G}^{R/A} \;&=\; \Re\,\bar{G}^R \,\pm\, i\,\Im\,\bar{G}^R \;=\; \Re\,\bar{G}^R \,\mp\, i\,\bar{A}/2\,, \qquad & \bar{A} \;&=\; \mp 2\,\Im\,\bar{G}^{R/A}\,, \\ \bar{\Sigma}^{R/A} \;&=\; \Re\,\bar{\Sigma}^R \,\pm\, i\,\Im\,\bar{\Sigma}^R \;=\; \Re\,\bar{\Sigma}^R \,\mp\, i\,\bar{\Gamma}/2\,, \qquad & \bar{\Gamma} \;&=\; \mp 2\,\Im\,\bar{\Sigma}^{R/A}\,. \end{aligned} \tag{40}$$

We find that in Wigner space the real parts of the retarded and advanced Green functions and selfenergies are equal, while the imaginary parts have opposite sign and are proportional to the spectral function $\bar{A}$ and the width $\bar{\Gamma}$, respectively. The next step consists in
ii) the separation of the real part and the imaginary part of the two equations for the retarded and advanced Green functions, that have to be fulfilled independently. Thus we obtain four real-valued equations for the self-consistent retarded and advanced Green functions. In the last step
iii) we get simple relations by linear combination of these equations, i.e. by adding/subtracting the relevant equations.

This finally leads to two algebraic relations for the spectral function $\bar{A}$ and the real part of the retarded Green function $Re\,\bar{G}^R$ in terms of the width $\bar{\Gamma}$ and the real part of the retarded self-energy $Re\,\bar{\Sigma}^R$ as [29]:

$$[\,p_0^2 - \mathbf{p}^{\,2} - m^2 - \bar{\Sigma}^\delta + \Re\,\bar{\Sigma}^R\,]\,\Re\,\bar{G}^R \;=\; 1 \;+\; \frac{1}{4}\,\bar{\Gamma}\,\bar{A}\,, \tag{41}$$

$$[\,p_0^2 - \mathbf{p}^{\,2} - m^2 - \bar{\Sigma}^\delta + \Re\,\bar{\Sigma}^R\,]\,\bar{A} \;=\; \bar{\Gamma}\,\Re\,\bar{G}^R\,. \tag{42}$$

Note that all terms with first order gradients have disappeared in Eqs. (41) and (42). A first consequence of (42) is a direct relation between the real and the imaginary parts of the retarded/advanced Green function, which reads (for $\bar{\Gamma} \neq 0$):

$$\Re\,\bar{G}^R \;=\; \frac{p_0^2 - \mathbf{p}^{\,2} - m^2 - \bar{\Sigma}^\delta - \Re\,\bar{\Sigma}^R}{\bar{\Gamma}}\;\bar{A}\,. \tag{43}$$

Inserting Eq. (43) in Eq. (41) we end up with the following result for the spectral function and the real part of the retarded Green function

$$\bar{A} = \frac{\bar{\Gamma}}{[\,p_0^2 - \mathbf{p}^2 - m^2 - \bar{\Sigma}^\delta - \Re\,\bar{\Sigma}^R\,]^2 + \bar{\Gamma}^2/4} = \frac{\bar{\Gamma}}{\bar{M}^2 + \bar{\Gamma}^2/4}\,, \tag{44}$$

$$\Re\,\bar{G}^R = \frac{[\,p_0^2 - \mathbf{p}^2 - m^2 - \bar{\Sigma}^\delta - \Re\,\bar{\Sigma}^R\,]}{[\,p_0^2 - \mathbf{p}^2 - m^2 - \bar{\Sigma}^\delta - \Re\,\bar{\Sigma}^R\,]^2 + \bar{\Gamma}^2/4} = \frac{\bar{M}}{\bar{M}^2 + \bar{\Gamma}^2/4}\,, \tag{45}$$

where we have introduced the mass-function $\bar{M}(p,x)$ in Wigner space:

$$\bar{M}(p,x) = p_0^2 - \mathbf{p}^2 - m^2 - \bar{\Sigma}^\delta(x) - \Re\,\bar{\Sigma}^R(p,x)\,. \tag{46}$$

The spectral function (44) shows a typical Breit-Wigner shape with energy- and momentum-dependent self-energy terms. Although the above equations are purely algebraic solutions and contain no derivative terms, they are valid up to the first order in the gradients!

In addition, subtraction of the real parts and adding up the imaginary parts lead to the time evolution equations

$$p^\mu\,\partial^x_\mu\,\bar{A} = \frac{1}{2}\,\{\,\bar{\Sigma}^\delta + \Re\,\bar{\Sigma}^R\,,\,\bar{A}\,\} + \frac{1}{2}\,\{\,\bar{\Gamma}\,,\,\Re\,\bar{G}^R\,\}\,, \tag{47}$$

$$p^\mu\,\partial^x_\mu\,\Re\,\bar{G}^R = \frac{1}{2}\,\{\,\bar{\Sigma}^\delta + \Re\,\bar{\Sigma}^R\,,\,\Re\,\bar{G}^R\,\} - \frac{1}{8}\,\{\,\bar{\Gamma}\,,\,\bar{A}\,\}\,. \tag{48}$$

The Poisson bracket containing the mass-function $\bar{M}$ leads to the well-known drift operator $p^\mu\,\partial^x_\mu\,\bar{F}$ (for an arbitrary function $\bar{F}$), i.e.

$$\{\,\bar{M}\,,\,\bar{F}\,\} = \{\,p_0^2 - \mathbf{p}^2 - m^2 - \bar{\Sigma}^\delta - \Re\,\bar{\Sigma}^R\,,\,\bar{F}\,\} = 2\,p^\mu\,\partial^x_\mu\,\bar{F} - \{\,\bar{\Sigma}^\delta + \Re\,\bar{\Sigma}^R\,,\,\bar{F}\,\}\,, \tag{49}$$

such that the first order equations (47) and (48) can be written in a more comprehensive form as

$$\{\,\bar{M}\,,\,\bar{A}\,\} = \{\,\bar{\Gamma}\,,\,\Re\,\bar{G}^R\,\}\,, \tag{50}$$

$$\{\,\bar{M}\,,\,\Re\,\bar{G}^R\,\} = -\frac{1}{4}\,\{\,\bar{\Gamma}\,,\,\bar{A}\,\}\,. \tag{51}$$

When inserting (44) and (45) we find that these first order time evolution equations are *solved* by the algebraic expressions. In this case the following relations hold [29]:

$$\{\,\bar{M}\,,\,\bar{A}\,\} = \{\,\bar{\Gamma}\,,\,\Re\,\bar{G}^R\,\} = \{\,\bar{M}\,,\,\bar{\Gamma}\,\}\;\frac{\bar{M}^2 - \bar{\Gamma}^2/4}{[\,\bar{M}^2 + \bar{\Gamma}^2/4\,]^2}\,, \tag{52}$$

$$\{\,\bar{M}\,,\,\Re\,\bar{G}^R\,\} = -\frac{1}{4}\,\{\,\bar{\Gamma}\,,\,\bar{A}\,\} = \{\,\bar{M}\,,\,\bar{\Gamma}\,\}\;\frac{\bar{M}\,\bar{\Gamma}/2}{[\,\bar{M}^2 + \bar{\Gamma}^2/4\,]^2}\,. \tag{53}$$

Thus we have derived the proper structure of the spectral function (44) within the first-order gradient (or semiclassical) approximation. Together with the explicit form for the real part of the retarded Green function (45) we now have fixed the dynamics of the spectral properties, which is consistent up to first order in the gradients.

As a next step we rewrite the memory terms in the collision integrals (34) such that the time integrations extend from $-\infty$ to $+\infty$. In this respect we consider the initial time $t_0 = -\infty$ whereas the upper time boundaries t_1, t_2 are taken into account by Θ-functions, i.e.

$$\begin{aligned} I_1^{\lessgtr}(x_1,x_2) &= -\int_{-\infty}^{\infty} d^Dx' \;\; \Theta(t_1 - t')\,\left[\,\Sigma^>(x_1,x') - \Sigma^<(x_1,x')\,\right]\;\; G^{\lessgtr}(x',x_2) \\ &\quad + \int_{-\infty}^{\infty} d^Dx' \;\; \Sigma^{\lessgtr}(x_1,x')\;\; \Theta(t_2 - t')\,\left[\,G^>(x',x_2) - G^<(x',x_2)\,\right] \\ &= -\int_{-\infty}^{\infty} d^Dx' \;\; \Sigma^R(x_1,x')\,G^{\lessgtr}(x',x_2) + \Sigma^{\lessgtr}(x_1,x')\,G^A(x',x_2)\,. \end{aligned} \tag{54}$$

We now perform the analogous steps as invoked before for the retarded and advanced Dyson-Schwinger equations. We start with a first order gradient expansion of the Wigner transformed Kadanoff-Baym equation using (54) for the memory integrals. Again we separate the real and the imaginary parts in the resulting equation, which have to be satisfied independently. At the end of this procedure we obtain a generalized transport equation:

$$\underbrace{2\,p^\mu\,\partial_\mu^x\,i\bar{G}^{\lessgtr} \;-\; \{\,\bar{\Sigma}^\delta + \Re\,\bar{\Sigma}^R,\, i\bar{G}^{\lessgtr}\,\}}_{\{\,\bar{M}\,,\,i\bar{G}^{\lessgtr}\,\}} - \{\,i\bar{\Sigma}^{\lessgtr}\,,\,\Re\,\bar{G}^R\,\} \;=\; i\bar{\Sigma}^<\,i\bar{G}^> \;-\; i\bar{\Sigma}^>\,i\bar{G}^<$$

$$\{\,\bar{M}\,,\,i\bar{G}^{\lessgtr}\,\} \qquad\qquad - \{\,i\bar{\Sigma}^{\lessgtr}\,,\,\Re\,\bar{G}^R\,\} \;=\; i\bar{\Sigma}^<\,i\bar{G}^> \;-\; i\bar{\Sigma}^>\,i\bar{G}^< \tag{55}$$

as well as a generalized mass-shell equation

$$\underbrace{[\,p^2 - m^2 - \bar{\Sigma}^\delta - \Re\,\bar{\Sigma}^R\,]}_{\bar{M}}\;i\bar{G}^{\lessgtr} \;=\; i\bar{\Sigma}^{\lessgtr}\,\Re\,\bar{G}^R \;+\; \frac{1}{4}\,\{\,i\bar{\Sigma}^>,\,i\bar{G}^<\,\} \;-\; \frac{1}{4}\,\{\,i\bar{\Sigma}^<,\,i\bar{G}^>\,\} \tag{56}$$

with the mass-function $\bar{M}$ specified in Eq. (46). Since the Green function $G^{\lessgtr}(x_1,x_2)$ consists of an antisymmetric real part and a symmetric imaginary part with respect to the relative coordinate $x_1 - x_2$, the Wigner transform of this function is purely imaginary. It is thus convenient to represent the Wightman functions in Wigner space by the real-valued quantities $i\bar{G}^{\lessgtr}(p,x)$. Since the collisional selfenergies obey the same symmetry relations in coordinate space and in phase-space, they will be kept also as $i\bar{\Sigma}^{\lessgtr}(p,x)$ further on.

In the transport equation (55) one recognizes on the l.h.s. the drift term $p^\mu\partial_\mu^x i\bar{G}^{\lessgtr}$, as well as the Vlasov term with the local self-energy $\bar{\Sigma}^\delta$ and the real part of the retarded self-energy $Re\,\bar{\Sigma}^R$. On the other hand the r.h.s. represents the collision term with its typical 'gain and loss' structure. The loss term $i\bar{\Sigma}^>\,i\bar{G}^<$ (proportional to the Green function itself) describes the scattering out of a respective phase-space cell, whereas the gain term $i\bar{\Sigma}^<\,i\bar{G}^>$ takes into account scatterings into the actual cell. The last term on the l.h.s. $\{\,i\bar{\Sigma}^{\lessgtr},\Re\,\bar{G}^R\,\}$ is very *peculiar* since it does not contain directly the distribution function $i\bar{G}^<$. This second Poisson bracket vanishes in the quasiparticle approximation and thus does not appear in the on-shell Boltzmann limit. As demonstrated in detail in Refs. [6, 26] the second Poisson bracket $\{\,i\bar{\Sigma}^{\lessgtr},\Re\,\bar{G}^R\,\}$ governs the evolution of the off-shell dynamics for nonequilibrium systems.

Although the generalized transport equation (55) and the generalized mass-shell equation (56) have been derived from the same Kadanoff-Baym equation in a first order gradient expansion, both equations are not exactly equivalent [15, 26]. Instead, they deviate from each other by contributions of second gradient order, which are hidden in the term $\{\,i\bar{\Sigma}^{\lessgtr},\Re\,\bar{G}^R\,\}$. A consistency, however, can be achieved by rewriting the self-energy $\bar{\Sigma}^<$ by $\bar{G}^<\cdot\bar{\Gamma}/\bar{A}$ in the Poisson bracket term $\{\bar{\Sigma}^<,\Re\,\bar{G}^R\}$. The generalized transport equation (55) then can be written in short-hand notation

$$\frac{1}{2}\,\bar{A}\,\bar{\Gamma}\;\left[\,\{\,\bar{M}\,,\;i\bar{G}^<\,\} \;-\; \frac{1}{\bar{\Gamma}}\,\{\,\bar{\Gamma}\,,\,\bar{M}\cdot i\bar{G}^<\,\}\right] \;=\; i\bar{\Sigma}^<\,i\bar{G}^> \;-\; i\bar{\Sigma}^>\,i\bar{G}^< \tag{57}$$

with the mass-function $\bar{M}$ (46). The transport equation (57) within the Botermans-Malfliet (BM) form resolves the discrepancy between the generalized mass-shell equation (56) and the generalized transport equation in its original Kadanoff-Baym form (55).

2.7. Test-particle representation and numerical solution

The generalized transport equation (57) allows to extend the traditional on-shell transport approaches for which efficient numerical recipes have been set up. In order to obtain a practical solution to the transport equation (57) we use a test-particle ansatz for the Green function $G^<$, more specifically for the real and positive semi-definite quantity (using $\bar{G}=G,\bar{\Sigma}=\Sigma,\bar{\Gamma}=\Gamma$),

$$F(x,p) \;= i\,G^<(x,p) \;\sim\; \sum_{i=1}^{N}\,\delta^{(3)}(\mathbf{x}\,-\,\mathbf{X}_i(t))\;\,\delta^{(3)}(\mathbf{p}\,-\,\mathbf{P}_i(t))\;\,\delta(p_0-\,\epsilon_i(t))\,, \tag{58}$$

where the sum over i describes the sum over all (properly normalized) testparticles. In the most general case (where the self energies depend on four-momentum P, time t and the spatial coordinates $\mathbf{X}$) the equations of motion for the test-particles i read

$$\frac{d\vec{X}_i}{dt} = \frac{1}{1-C_{(i)}}\frac{1}{2\epsilon_i}\left[2\,\vec{P}_i + \vec{\nabla}_{P_i}\Re\Sigma^R_{(i)} + \frac{\epsilon_i^2-\vec{P}_i^2-M_0^2-\Re\Sigma^R_{(i)}}{\Gamma_{(i)}}\,\vec{\nabla}_{P_i}\Gamma_{(i)}\right], \tag{59}$$

$$\frac{d\vec{P}_i}{dt} = -\frac{1}{1-C_{(i)}}\frac{1}{2\epsilon_i}\left[\vec{\nabla}_{X_i}\Re\Sigma^R_i + \frac{\epsilon_i^2-\vec{P}_i^2-M_0^2-\Re\Sigma^R_{(i)}}{\Gamma_{(i)}}\,\vec{\nabla}_{X_i}\Gamma_{(i)}\right], \tag{60}$$

$$\frac{d\epsilon_i}{dt} = \frac{1}{1-C_{(i)}}\frac{1}{2\epsilon_i}\left[\frac{\partial\Re\Sigma^R_{(i)}}{\partial t} + \frac{\epsilon_i^2-\vec{P}_i^2-M_0^2-Re\Sigma^R_{(i)}}{\Gamma_{(i)}}\,\frac{\partial\Gamma_{(i)}}{\partial t}\right], \tag{61}$$

where the notation $F_{(i)}$ implies that the function is taken at the coordinates of the test-particle, i.e. $F_{(i)} \equiv F(t,\mathbf{X}_i(t),\mathbf{P}_i(t),\epsilon_i(t))$.

In Eqs. (59-61), a common multiplication factor $(1-C_{(i)})^{-1}$ appears, which contains the energy derivatives of the retarded self energy

$$C_{(i)} = \frac{1}{2\epsilon_i}\left[\frac{\partial}{\partial\epsilon_i}\Re\Sigma^R_{(i)} + \frac{\epsilon_i^2-\vec{P}_i^2-M_0^2-Re\Sigma^R_{(i)}}{\Gamma_{(i)}}\,\frac{\partial}{\partial\epsilon_i}\Gamma_{(i)}\right]. \tag{62}$$

It yields a shift of the system time t to the 'eigentime' of particle i defined by $\tilde{t}_i = t/(1-C_{(i)})$. As the reader immediately verifies, the derivatives with respect to the 'eigentime', i.e. $d\mathbf{X}_i/d\tilde{t}_i$, $d\mathbf{P}_i/d\tilde{t}_i$ and $d\epsilon_i/d\tilde{t}_i$ then emerge without this renormalization factor for each test-particle i when neglecting higher order time derivatives in line with the semiclassical approximation scheme. Note that the test-particle equations of motion (presented above) should not be applied for arbitrary selfenergies Σ^R and width Γ since the theory must obey micro-causality. This leads to severe constraints for the selfenergies [23, 24, 30].

Some limiting cases should be mentioned explicitly: In case of a momentum-independent 'width' $\Gamma(x)$ we take $M^2 = P^2 - Re\Sigma^R$ as an independent variable instead of P_0, which then fixes the energy (for given $\mathbf{P}$ and M^2) to

$$p_0^2 = \mathbf{p}^2 + M^2 + \Re\Sigma(x,\mathbf{p},M^2)^R\,. \tag{63}$$

Eq. (61) then turns to ($\Delta M_i^2 = M_i^2 - M_0^2$)

$$\frac{d\Delta M_i^2}{dt} = \frac{\Delta M_i^2}{\Gamma_{(i)}}\,\frac{d\Gamma_{(i)}}{dt} \qquad \leftrightarrow \qquad \frac{d}{dt}\ln\left(\frac{\Delta M_i^2}{\Gamma_{(i)}}\right) = 0 \tag{64}$$

for the time evolution of the test-particle i in the invariant mass squared. In case of $\Gamma = const.$ the familiar equations of motion for test-particles in on-shell transport approaches are regained. We mention in passing that in the Parton-Hadron-String Dynamics (PHSD) transport approach [31, 32] the width of partonic degrees-of-freedom (so far) is taken as momentum independent such that the simple limit (64) applies (see below).

3. Dynamical quasiparticle model for hot QCD

Early concepts of the Quark-Gluon-Plasma (QGP) were guided by the idea of a weakly interacting system of massless partons which might be described by perturbative QCD (pQCD). However, experimental observations at RHIC indicated that the new medium created in ultrarelativistic Au+Au collisions is interacting more strongly than hadronic matter. It is presently widely accepted that this medium is an almost perfect liquid of partons as extracted experimentally from the strong radial expansion and the scaling of the elliptic flow $v_2(p_T)$ of mesons and baryons with the number of constituent quarks and antiquarks. At vanishing quark chemical potential μ_q the QCD problem can be addressed at zero and finite temperature by lattice QCD calculations on a 3+1 dimensional torus with a suitable discretization of the QCD action on the euclidian lattice. These calculations so far have provided valuable information on the QCD equation of state, chiral symmetry restoration and various correlators that can be attributed/related to transport coefficients. Due to the Fermion 'sign'-problem lQCD calculations at finite μ_q are presently not robust and one has to rely on nonperturbative - but effective - models to obtain information in the (T, μ_q) plane or for systems out-off equilibrium.

3.1. Quasiparticle properties

As demonstrated above a consistent dynamical approach for the description of strongly interacting systems - also out-off equilibrium - can be formulated on the basis of Kadanoff-Baym (KB) equations or off-shell transport equations in phase-space representation (cf. Section 2), respectively. In the KB theory the field quanta are described in terms of dressed propagators with complex selfenergies [33]. Whereas the real part of the selfenergies can be related to mean-field potentials (of Lorentz scalar, vector or tensor type), the imaginary parts provide information about the lifetime and/or reaction rates of time-like 'particles'. Once the proper (complex) selfenergies of the degrees-of-freedom are known, the time evolution of the system is fully governed by off-shell transport equations (cf. Section 2). The determination/extraction of complex selfenergies for the partonic degrees-of-freedom can be performed within the Dynamical QuasiParticle Model (DQPM) by fitting lattice QCD calculations in thermal equilibrium. The DQPM postulates retarded propagators of the quark and gluon degrees-of-freedom in the form

$$G^R(\omega, \mathbf{p}) = \frac{1}{\omega^2 - \mathbf{p}^2 - M^2 + 2i\gamma\omega} \tag{65}$$

using $\omega = p_0$. In the scope of the DQPM the running coupling (squared) is approximated by

$$g^2(T/T_c) = \frac{48\pi^2}{(11N_c - 2N_f)\ln[\lambda^2(T/T_c - T_s/T_c)^2]}, \tag{66}$$

where the parameters $\lambda \approx 2.42$ and $T_s/T_c \approx 0.56$ have to be extracted from a fit to the lattice data in Fig. 3 (r.h.s.) (see below). In Eq. (66), $N_c = 3$ stands for the number of colors, T_c is the critical temperature (≈ 158 MeV), while $N_f(= 3)$ denotes the number of flavors. The parameter T_s is essentially important for the infrared enhancement of the coupling at low temperature T. It has been demonstrated in Ref. [34] that this functional form for the strong coupling $\alpha_s = g^2/(4\pi)$ is in accordance with the lQCD calculations of the Bielefeld group for the long range part of the $q - \bar{q}$ potential. Furthermore, it matches the hard-thermal-loop (HTL) limit for high temperatures T.

The dynamical quasiparticle mass (for gluons and quarks) is assumed to be given by the HTL thermal mass in the asymptotic high-momentum regime, i.e. for gluons

$$M_g^2(T) = \frac{g^2}{6}\left(\left(N_c + \frac{1}{2}N_f\right)T^2 + \frac{N_c}{2}\sum_q \frac{\mu_q^2}{\pi^2}\right) , \tag{67}$$

and for quarks (antiquarks)

$$M_{q(\bar{q})}^2(T) = \frac{N_c^2 - 1}{8N_c}g^2\left(T^2 + \frac{\mu_q^2}{\pi^2}\right) , \tag{68}$$

but with the coupling given in Eq. (66). The dynamical masses (68) in the QGP are large compared to the bare masses of the light (u, d) quarks and adopted in the form (68) for the (u, d) quarks. The strange quark has a larger bare mass which also enters to some extent the dynamical mass $M_s(T)$. This essentially suppresses the channel $g \to s + \bar{s}$ relative to the channel $g \to u + \bar{u}$ or $d + \bar{d}$ and controls the strangeness ratio in the QGP. Empirically we have used $M_s(T) = M_u(T) + \Delta M = M_d(T) + \Delta M$ where $\Delta M = 35$ MeV, which has been fixed once in comparison to experimental data for the K^+/π^+ ratio in central Au+Au collisions at $\sqrt{s_{NN}}$ = 17.3 GeV. Furthermore, the effective quarks, antiquarks and gluons in the DQPM have finite widths, which for $\mu_q = 0$ are adopted in the form

$$\gamma_g(T) \quad = \quad \frac{1}{3}N_c\frac{g^2T}{8\pi}\ln\left(\frac{2c}{g^2} + 1\right), \quad \gamma_{q(\bar{q})}(T) = \frac{1}{3}\frac{N_c^2 - 1}{2N_c}\frac{g^2T}{8\pi}\ln\left(\frac{2c}{g^2} + 1\right), \tag{69}$$

where $c = 14.4$ is related to a magnetic cut-off, which is one of the parameters of the DQPM. Furthermore, we assume that the width of the strange quark is the same as that for the light (u, d) quarks.

The physical processes contributing to the width γ_g are both $gg \leftrightarrow gg$, $gq \leftrightarrow gq$ scattering as well as splitting and fusion reactions $gg \leftrightarrow g$, $gg \leftrightarrow ggg$, $ggg \leftrightarrow gggg$ or $g \leftrightarrow q\bar{q}$ etc. On the fermion side elastic fermion-fermion scattering $pp \leftrightarrow pp$, where p stands for a quark q or antiquark $\bar{q}$, fermion-gluon scattering $pg \leftrightarrow pg$, gluon bremsstrahlung $pp \leftrightarrow pp + g$ or quark-antiquark fusion $q\bar{q} \leftrightarrow g$ etc. emerge. Note, however, that the explicit form of (69) is derived for hard two-body scatterings only.

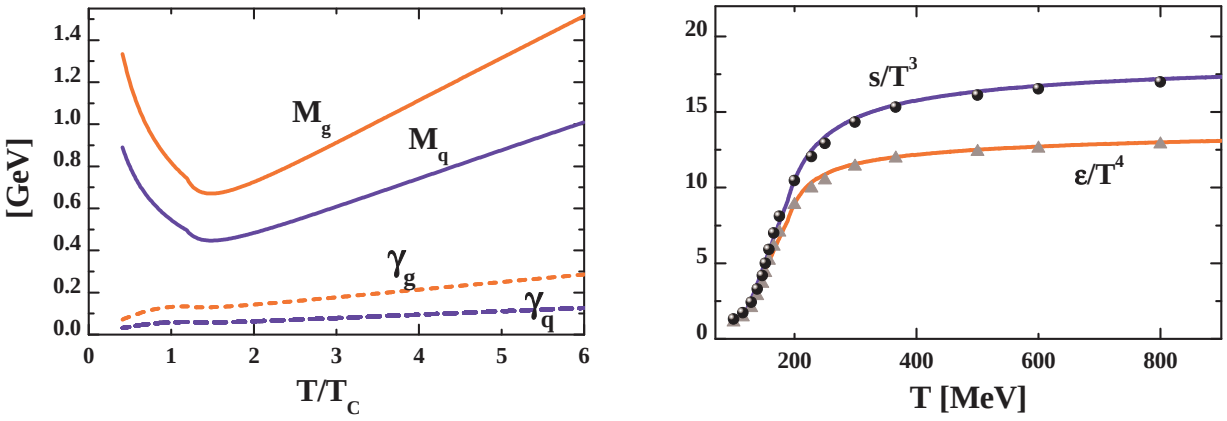


Figure 3: *(l.h.s.)* The effective gluon mass M_g and width γ_g as function of the scaled temperature T/T_c (upper red lines). The lower blue lines show the corresponding quantities for quarks. *(r.h.s.)* The scaled entropy density $s(T)/T^3$ (upper blue line) and scaled energy density $\epsilon(T)/T^4$ (lower red line) from the DQPM in comparison to the lQCD results from the BMW group (full dots and triangles) [35]. The figures are taken from Ref. [32].

3.2. Spectral functions

In the DQPM the parton spectral functions are no longer δ-functions in the invariant mass squared but taken as (cf. Eq. (29) in Section 2)

$$\rho_j(\omega,\mathbf{p}) = \frac{\gamma_j}{2E_j}\left(\frac{1}{(\omega-E_j)^2+\gamma_j^2} - \frac{1}{(\omega+E_j)^2+\gamma_j^2}\right) \tag{70}$$

separately for quarks, antiquarks and gluons ($j = q, \bar{q}, g$). Here $E_j^2(\mathbf{p}^2) = \mathbf{p}^2 + M_j^2 - \gamma_j^2$, where the parameters γ_j, M_j from the DQPM have been described above. The spectral function (70) is antisymmetric in ω and normalized as

$$\int_{-\infty}^{\infty} \frac{d\omega}{2\pi}\, 2\omega\, \rho_j(\omega,\mathbf{p}) = 2\int_0^{\infty} \frac{d\omega}{2\pi}\, 2\omega\rho_j(\omega,\mathbf{p}) = 1 \tag{71}$$

as mandatory for quantum field theory.

The actual gluon mass M_g and width γ_g – employed as input in the further calculations – as well as the quark mass M_q and width γ_q are depicted in Fig. 3 (l.h.s.) as a function of T/T_c. Note that for $\mu_q = 0$ the DQPM gives

$$M_q = \frac{2}{3}M_g, \qquad \gamma_q = \frac{4}{9}\gamma_g\ . \tag{72}$$

These variations of the masses with the temperature T – that appear drastic in Fig. 3 (l.h.s.) – become, however, rather smooth if viewed as a function of the scalar parton density ρ_s defined (in thermal equilibrium) by

$$\begin{aligned}\rho_s(T/T_c) \;=\; & d_g \int_0^{\infty}\frac{d\omega}{2\pi}\int\frac{d^3p}{(2\pi)^3}\, 2\sqrt{p^2}\;\rho_g(\omega,\mathbf{p})\; n_B(\omega/T)\;\Theta(p^2)\\ & + d_q \int_0^{\infty}\frac{d\omega}{2\pi}\int\frac{d^3p}{(2\pi)^3}\, 2\sqrt{p^2}\;\rho_q(\omega,\mathbf{p})\; n_F((\omega-\mu_q)/T)\;\Theta(p^2)\\ & + d_{\bar{q}} \int_0^{\infty}\frac{d\omega}{2\pi}\int\frac{d^3p}{(2\pi)^3}\, 2\sqrt{p^2}\;\rho_{\bar{q}}(\omega,\mathbf{p})\; n_F((\omega+\mu_q)/T)\;\Theta(p^2)\ ,\end{aligned} \tag{73}$$

where n_B and n_F denote the Bose and Fermi functions, respectively, while μ_q stands for the quark chemical potential. The number of transverse gluonic degrees-of-freedom is $d_g = 16$ while the fermion degrees-of-freedom amount to $d_q = d_{\bar{q}} = 2N_cN_f = 18$ in case of three flavors (N_f=3). The function $\Theta(p^2)$ (with $p^2 = \omega^2 - \mathbf{p}^2$) projects on **time-like** four-momenta since only this fraction of the four-momentum distribution can be propagated within the light cone.

3.3. Thermodynamics of QCD

With the quasiparticle properties (or propagators) chosen as described above, one can evaluate the entropy density $s(T)$, the pressure $P(T)$ and energy density $\epsilon(T)$ in a straight forward manner by starting with the entropy density in the quasiparticle limit from Baym [36],

$$\begin{aligned} s^{dqp} &= -d_g \int \frac{d\omega}{2\pi} \frac{d^3p}{(2\pi)^3} \frac{\partial n_B}{\partial T} \left(\Im \ln(-\Delta^{-1}) + \Im\Pi \, \Re\Delta \right) \\ &\quad -d_q \int \frac{d\omega}{2\pi} \frac{d^3p}{(2\pi)^3} \frac{\partial n_F((\omega-\mu_q)/T)}{\partial T} \left(\Im \ln(-S_q^{-1}) + \Im\Sigma_q \, \Re S_q \right), \\ &\quad -d_{\bar q} \int \frac{d\omega}{2\pi} \frac{d^3p}{(2\pi)^3} \frac{\partial n_F((\omega+\mu_q)/T)}{\partial T} \left(\Im \ln(-S_{\bar q}^{-1}) + \Im\Sigma_{\bar q} \, \Re S_{\bar q} \right), \end{aligned} \tag{74}$$

where $n_B(\omega/T) = (\exp(\omega/T) - 1)^{-1}$ and $n_F((\omega - \mu_q)/T) = (\exp((\omega - \mu_q)/T) + 1)^{-1}$ denote the Bose and Fermi distribution functions, respectively, while $\Delta = (P^2 - \Pi)^{-1}$, $S_q = (P^2 - \Sigma_q)^{-1}$ and $S_{\bar q} = (P^2 - \Sigma_{\bar q})^{-1}$ stand for the full (scalar) quasiparticle propagators of gluons g, quarks q and antiquarks $\bar q$. In Eq. (74) Π and $\Sigma = \Sigma_q \approx \Sigma_{\bar q}$ denote the (retarded) quasiparticle selfenergies. In principle, Π as well as Δ are Lorentz tensors and should be evaluated in a nonperturbative framework. The DQPM treats these degrees-of-freedom as independent scalar fields with scalar selfenergies which are assumed to be identical for quarks and antiquarks. Note that one has to treat quarks and antiquarks separately in Eq. (74) as their abundance differs at finite quark chemical potential μ_q.

Since the nonperturbative evaluation of the propagators and selfenergies in QCD is a formidable task [and addressed in Dyson-Schwinger (DS) Bethe-Salpeter (BS) approaches] an alternative and practical procedure is to use physically motivated *Ansätze* with Lorentzian spectral functions for quarks[1] and gluons as in (70). With this choice the complex selfenergies $\Pi = M_g^2 - 2i\omega\gamma_g$ and $\Sigma_q(\mathbf{q}) = M_q(\mathbf{q})^2 - 2i\gamma_q(\mathbf{q})$ are fully defined via (67), (68), (69). Note that the retarded propagator (65),

$$G_R^{-1} = \omega^2 - \mathbf{p}^2 - M^2 + 2i\gamma\omega, \tag{75}$$

corresponds to the propagator of a damped harmonic oscillator (with an additional $\mathbf{p}^2$) and preserves microcausality also for $\gamma > M$ [30], i.e. in case of overdamped motion. Although the 'Ansatz' for the parton propagators is not QCD we will demonstrate that a variety of QCD observables on the lattice are compatible with this choice.

Since within the DQPM the real and imaginary parts of the propagators Δ and S now are fixed analytically the entropy density (74) can be evaluated numerically. As we deal with a grandcanonical ensemble the Maxwell relations give (at $\mu_q = 0$),

$$s = \frac{\partial P}{\partial T} \, , \tag{76}$$

such that the pressure can be obtained by integration of the entropy density s over T, where one tacitly identifies the 'full' entropy density s with the quasiparticle entropy density s^{dqp} (74). The starting point for the integration in T is chosen between 100 MeV $< T <$ 120 MeV where the entropy density is approximated by that of a noninteracting pion, η and kaon gas.

The energy density ϵ then follows from the thermodynamical relation

$$\epsilon = Ts - P \tag{77}$$

(for $\mu_q = 0$) and thus is also fixed by the entropy $s(T)$ as well as the interaction measure

$$W(T) := \epsilon(T) - 3P(T) = Ts - 4P \tag{78}$$

that vanishes for massless and noninteracting degrees-of-freedom.

A direct comparison of the resulting entropy density $s(T)$ (74) - using (66) to (70) - and energy density $\epsilon(T)$ (77) from the DQPM with lQCD results from the BMW group [35] is presented in Fig. 3 (r.h.s.). Both results have been divided by T^3 and T^4, respectively, to demonstrate the scaling with temperature. The agreement is sufficiently good. A satisfactory agreement also holds for the dimensionless 'interaction measure', i.e. $(\epsilon - 3P)/T^4$ (cf. Fig. 4, l.h.s.).

[1] In the following the abbreviation is used that 'quarks' denote quarks and antiquarks if not specified explicitly.

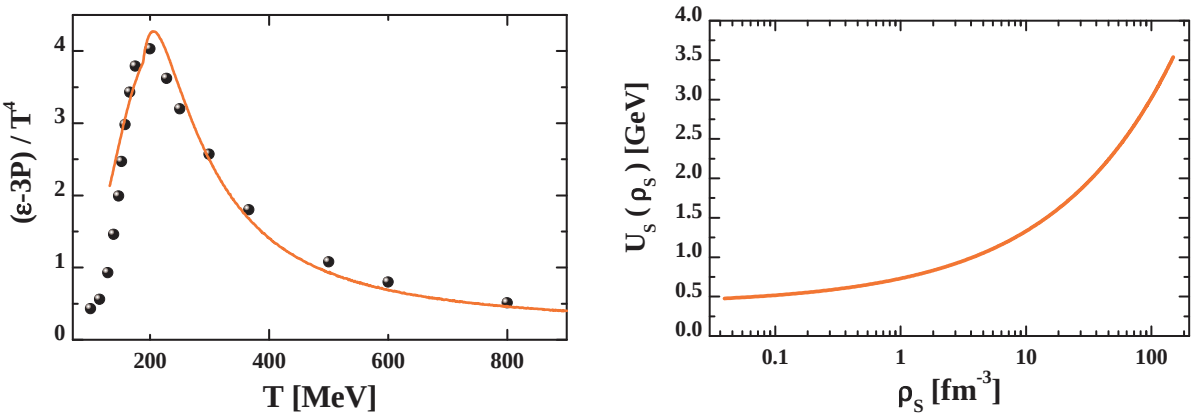


Figure 4: (l.h.s.) The interaction measure $(\epsilon - 3P)/T^4$ from the DQPM in comparison to the lQCD results from [35]. (r.h.s.) The scalar mean-field (80) for quarks and antiquarks from the DQPM as a function of the scalar parton density ρ_s for $\mu_q = 0$. The figures are taken from Ref. [32].

3.4. Partonic mean-field potentials from the DQPM

The DQPM uniquely defines a potential energy density,

$$V_p(T, \mu_q) = T^{00}_{g-}(T, \mu_q) + T^{00}_{q-}(T, \mu_q) + T^{00}_{\bar{q}-}(T, \mu_q), \tag{79}$$

where the different contributions T^{00}_{j-} correspond to the space-like part of the energy-momentum tensor component T^{00}_j of parton $j = g, q, \bar{q}$ [33]. It is found that this quantity is practically independent on the quark chemical potential (for moderate μ_q) when displayed as a function of the scalar density ρ_s instead of T and μ_q separately. Note that the field quanta involved in (79) are virtual and thus correspond to partons exchanged in interaction diagrams.

A scalar mean-field $U_s(\rho_s)$ for quarks and antiquarks is defined by the derivative [33],

$$U_s(\rho_s) = \frac{dV_p(\rho_s)}{d\rho_s}, \tag{80}$$

which is evaluated numerically within the DQPM. The result is displayed in Fig. 4 (r.h.s.) as a function of the parton scalar density ρ_s (73) and shows that the scalar mean-field is in the order of a few GeV for $\rho_s > 10$ fm^{-3}. This mean-field (80) is employed in the PHSD transport calculations and determines the force on a quasiparticle j, i.e. $\sim M_j/E_j \nabla U_s(x) = M_j/E_j \; dU_s/d\rho_s \; \nabla\rho_s(x)$ where the scalar density $\rho_s(x)$ is determined numerically on a space-time grid (see below).

3.5. DQPM at finite quark chemical potential

Since the coupling (squared) in the DQPM is a function of T/T_c and in the Hard-Thermal-Loop approximation depends on

$$T^*(T, \mu_q) = \sqrt{T^2 + \mu_q^2/\pi^2}, \tag{81}$$

a straight forward extension of the DQPM to finite μ_q is to consider the coupling as a function of $T^*/T_c(\mu_q)$ with a μ_q-dependent critical temperature $T_c(\mu_q)$,

$$\frac{T_c(\mu_q)}{T_c(\mu_q = 0)} = \sqrt{1 - \alpha \; \mu_q^2} \approx 1 - \alpha/2 \; \mu_q^2 + \cdots \tag{82}$$

with $\alpha \approx 8.79$ GeV^{-2}. The expression of $T_c(\mu_q)$ in Eq. (82) is obtained by requiring a constant energy density ϵ for the system at $T = T_c(\mu_q)$ where ϵ at $T_c(\mu_q = 0) \approx 0.158$ GeV is fixed by a lattice QCD calculation at $\mu_q = 0$ [35]. The coefficient in front of the μ_q^2-dependent part can be compared to recent lQCD calculations at finite (but small) μ_B which gives [37]:

$$\frac{T_c(\mu_B)}{T_c} = 1 - \kappa \left(\frac{\mu_B}{T_c}\right)^2 + \cdots \tag{83}$$

with $\kappa = 0.013(2)$. Rewriting Eq. (82) in the form (83) and using $\mu_B \approx 3\mu_q$ we get $\kappa_{DQPM} \approx 0.0122$ which compares very well with the lQCD result. Consequently one has to expect an approximate scaling of the DQPM results if the partonic width is assumed to have the form,

$$\gamma_g(T,\mu_q) = \frac{1}{3} N_c \frac{g^2(T^*/T_c(\mu_q))}{8\pi}\, T\ \ln\left(\frac{2c}{g^2(T^*/T_c(\mu_q))}+1\right),$$
$$\gamma_q(T,\mu_q) = \frac{1}{3} \frac{N_c^2-1}{2N_c} \frac{g^2(T^*/T_c(\mu_q))}{8\pi}\, T\ \ln\left(\frac{2c}{g^2(T^*/T_c(\mu_q))}+1\right). \quad (84)$$

This choice leads to an approximate independence of the potential energies per degree-of-freedom as a function of (moderate) μ_q. Nevertheless, the conjecture (84) should be explicitly controlled by future lQCD studies for N_f=3 at finite quark chemical potential. Unfortunately, this task is presently out of reach and one has to live with the uncertainty in (84) which is assumed in the following investigations.

We point out, furthermore, that in general the quasiparticle masses M_j as well as the widths γ_j might depend also on the momentum $\mathbf{q}$ relative to the medium at rest and approach the perturbative values at high q^2. So far, the momentum dependence of the complex selfenergy cannot reliably be extracted from the lQCD results in thermodynamic equilibrium which are essentially sensitive to momenta in the order of a few times the temperature. This is presently an open issue and will have to be re-addressed in future.

On the basis of the DQPM for the partonic phase a relativistic off-shell transport approach has been developed in the past decade that gives approximately the same dynamics as the DQPM for partonic systems in equilibrium but also contains interacting hadrons and a dynamical transition between hadronic and partonic degrees-of-freedom. This approach that can also be employed for systems out of equilibrium – such as heavy-ion collisions – is denoted by Parton-Hadron-String Dynamics (PHSD). The detailed set up of PHSD as well as its comparison to heavy-ion data from low SPS to LHC energies is described in the next Section.

4. The PHSD approach

The Parton-Hadron-String-Dynamics approach is a microscopic covariant transport model that incorporates effective partonic as well as hadronic degrees-of-freedom and involves a dynamical description of the hadronization process from partonic to hadronic matter. Whereas the hadronic part is essentially equivalent to the conventional HSD approach [38, 39] the partonic dynamics is based on the Dynamical Quasiparticle Model [34, 40, 41, 42] which describes QCD properties in terms of single-particle Green's functions. With the (essentially three) DQPM parameters for the temperature-dependent effective coupling (66) fixed by lattice QCD results – as described in Section 3 – the approach is fully defined in the partonic phase.

One might ask whether the quasiparticle properties – fixed in thermal equilibrium – should be appropriate also for the nonequilibrium configurations. This question is nontrivial and can only be answered by detailed investigations e.g. on the basis of Kadanoff-Baym equations. We recall that such studies have been summarized in Ref. [33] for strongly interacting scalar fields that initially are far off-equilibrium and simulate momentum distributions of colliding systems at high relative momentum. The results for the effective parameters M and γ, which correspond to the time-dependent pole mass and width of the propagator, indicate that the quasiparticle properties - except for the very early off-equilibrium configuration - are close to the equilibrium mass and width even though the phase-space distribution of the particles is far from equilibrium (cf. Figs. 8 to 10 in Ref. [33]). Accordingly, we will adopt the equilibrium quasiparticle properties also for phase-space configurations out of equilibrium as appearing in relativistic heavy-ion collisions. The reader has to keep in mind that this approximation is well motivated, however, not fully equivalent to the exact solution.

On the hadronic side PHSD includes explicitly the baryon octet and decouplet, the 0^-- and 1^--meson nonets as well as selected higher resonances as in HSD [38, 39]. Hadrons of higher masses (> 1.5 GeV in case of baryons and > 1.3 GeV in case of mesons) are treated as 'strings' (color-dipoles) that decay to the known (low-mass) hadrons according to the JETSET algorithm [43]. We discard an explicit recapitulation of the string formation and decay and refer the reader to the original work [43].

4.1. Hadronization

Whereas the dynamics of partonic as well as hadronic systems is fixed by the DQPM or HSD, respectively, the change in the degrees-of-freedom has to be specified in line with the lattice QCD equation of state. The

hadronization, i.e. the transition from partonic to hadronic degrees-of-freedom, has been introduced in Refs. [31, 44] and is repeated here for completeness. The hadronization is implemented in PHSD by local covariant transition rates e.g. for $q + \bar{q}$ fusion to a mesonic state m of four-momentum $p = (\omega, \mathbf{p})$ at space-time point $x = (t, \mathbf{x})$:

$$\frac{dN_m(x,p)}{d^4x d^4p} = Tr_q Tr_{\bar{q}}\ \delta^4(p - p_q - p_{\bar{q}})\ \delta^4\left(\frac{x_q + x_{\bar{q}}}{2} - x\right) \omega_q\ \rho_q(p_q)\ \omega_{\bar{q}}\ \rho_{\bar{q}}(p_{\bar{q}}) \\ \times |v_{q\bar{q}}|^2\ W_m(x_q - x_{\bar{q}}, (p_q - p_{\bar{q}})/2)\ N_q(x_q, p_q)\ N_{\bar{q}}(x_{\bar{q}}, p_{\bar{q}})\ \delta(\text{flavor, color}). \tag{85}$$

In Eq. (85) we have introduced the shorthand notation,

$$Tr_j = \sum_j \int d^4x_j \int \frac{d^4p_j}{(2\pi)^4}\ , \tag{86}$$

where $\sum_j$ denotes a summation over discrete quantum numbers (spin, flavor, color); $N_j(x,p)$ is the phase-space density of parton j at space-time position x and four-momentum p. In Eq. (85) δ(flavor, color) stands symbolically for the conservation of flavor quantum numbers as well as color neutrality of the formed hadronic state m which can be viewed as a color-dipole or 'pre-hadron'. Furthermore, $v_{q\bar{q}}(\rho_p)$ is the effective quark-antiquark interaction from the DQPM (displayed in Fig. 10 of Ref. [42]) as a function of the local parton $(q + \bar{q} + g)$ density ρ_p (or energy density). Furthermore, $W_m(x,p)$ is the dimensionless phase-space distribution of the formed 'pre-hadron', i.e.

$$W_m(\xi, p_\xi) = \exp\left(\frac{\xi^2}{2b^2}\right)\ \exp\left(2b^2(p_\xi^2 - (M_q - M_{\bar{q}})^2/4)\right) \tag{87}$$

with $\xi = x_1 - x_2 = x_q - x_{\bar{q}}$ and $p_\xi = (p_1 - p_2)/2 = (p_q - p_{\bar{q}})/2$ (which had been previously introduced in Eq. (2.14) of Ref. [45]). The width parameter b is fixed by $\sqrt{\langle r^2 \rangle} = b = 0.66$ fm (in the rest frame) which corresponds to an average rms radius of mesons. We note that the expression (87) corresponds to the limit of independent harmonic oscillator states and that the final hadron-formation rates are approximately independent of the parameter b within reasonable variations. By construction the quantity (87) is Lorentz invariant; in the limit of instantaneous 'hadron formation', i.e. $\xi^0 = 0$, it provides a Gaussian dropping in the relative distance squared $(\mathbf{r}_1 - \mathbf{r}_2)^2$. The four-momentum dependence reads explicitly (except for a factor 1/2)

$$(E_1 - E_2)^2 - (\mathbf{p}_1 - \mathbf{p}_2)^2 - (M_1 - M_2)^2 \leq 0 \tag{88}$$

and leads to a negative argument of the second exponential in Ed. (87) favoring the fusion of partons with low relative momenta $p_q - p_{\bar{q}} = p_1 - p_2$.

Some comments on the hadronization scheme are in order: The probability for a quark to hadronize is essentially proportional to the timestep dt in the calculation, the number of possible hadronization partners in the volume $dV \sim 5$ fm^3 and the transition matrix element squared (apart from the gaussian overlap function). For temperatures above T_c the probability is rather small ($\ll 1$) but for temperatures close to T_c and below T_c the matrix element becomes very large since it essentially scales with the effective coupling squared (66) which is strongly enhanced in the infrared. For a finite timestep dt – as used in the calculations – the probability becomes larger than 1 which implies that the quark has to hadronize with some of the potential antiquarks in the actual timestep if the temperature or energy density becomes too low. Furthermore, the gluons practically freeze out close to T_c since the mass difference between quarks and gluons increases drastically with decreasing temperature and the reaction channel $g \leftrightarrow q + \bar{q}$ is close to equilibrium. This implies that all partons hadronize. Due to numerics some 'leftover' partons may occur at the end of the calculations which are 'forced' to hadronize by increasing the volume dV until they have found a suitable partner. In practice the 'forced' hadronization was only used for LHC energies where the computational time was stopped at ~ 1000 fm/c when partons with rapidities close to projectile or target rapidity did not yet hadronize due to time dilatation ($\gamma_{cm} \approx 1400$).

Related transition rates (85) are defined for the fusion of three off-shell quarks ($q_1 + q_2 + q_3 \leftrightarrow B$) to a color neutral baryonic (B or $\bar{B}$) resonances of finite width (or strings) fulfilling energy and momentum conservation as well as flavor current conservation (cf. Section 2.3 in Ref. [31]). In contrast to the familiar coalescence models this hadronization scheme solves the problem of simultaneously fulfilling all conservation laws and the constraint of entropy production. For further details we refer the reader to Refs. [31, 44].

4.2. Initial conditions

The initial conditions for the parton/hadron dynamical system have to be specified additionally. In order to describe relativistic heavy-ion reactions we start with two nuclei in their 'semi-classical' groundstate, boosted towards each other with a velocity β (in z-direction), fixed by the bombarding energy. The initial phase-space distributions of the projectile and target nuclei are determined in the local Thomas-Fermi limit as in the HSD transport approach [38, 39] or the UrQMD model [46, 47]. We recall that at relativistic energies the initial interactions of two nucleons are well described by the excitation of two color-neutral strings which decay in time to the known hadrons (mesons, baryons, antibaryons) [43]. Initial hard processes - i.e. the short-range high-momentum transfer reactions that can be well described by perturbative QCD - are treated in PHSD (as in HSD) via PYTHIA 5.7 [48]. The novel element in PHSD (relative to HSD) is the 'string melting concept' as also used in the AMPT model [49] in a similar context. However, in PHSD the strings (or possibly formed hadrons) are only allowed to 'melt' if the local energy density $\epsilon(x)$ (in the local rest frame) is above the transition energy density ϵ_c which in the present DQPM version is $\epsilon_c \approx 0.5$ GeV/fm^3. The mesonic strings then decay to quark-antiquark pairs according to an intrinsic quark momentum distribution,

$$F(\mathbf{q}) \sim \exp(-2b^2\mathbf{q}^2) \ , \tag{89}$$

in the meson rest-frame (cf. Eq. (85) for the inverse process). The parton final four-momenta are selected randomly according to the momentum distribution (89) (with b= 0.66 fm), and the parton-energy distribution is fixed by the DQPM at given energy density $\epsilon(\rho_s)$ in the local cell with scalar parton density ρ_s. The flavor content of the $q\bar{q}$ pair is fully determined by the flavor content of the initial string. By construction the 'string melting' to massive partons conserves energy and momentum as well as the flavor content. In contrast to Ref. [49] the partons are of finite mass – in line with their local spectral function – and obtain a random color $c = (1, 2, 3)$ or (r, b, g) in addition. Of course, the color appointment is color neutral, i.e. when selecting a color c for the quark randomly the color for the antiquark is fixed by $-c$. The baryonic strings melt analogously into a quark and a diquark while the diquark, furthermore, decays to two quarks. Dressed gluons are generated by the fusion of nearest neighbor $q + \bar{q}$ pairs ($q + \bar{q} \to g$) that are flavor neutral until the ratio of gluons to quarks reaches the value $N_g/(N_q+N_{\bar{q}})$ given by the DQPM for the energy density of the local cell. This 'recombination' is performed for all cells in space during the passage time of the target and projectile (before the calculation continues with the next timestep) and conserves the four-momentum as well as the flavor currents. We note, however, that the initial phase in PHSD is dominated by quark and antiquark degrees-of-freedom.

Apart from proton-proton, proton-nucleus or nucleus-nucleus collisions the PHSD approach can also be employed to study the properties of the interacting hadron/parton system in a finite box with periodic boundary conditions (cf. Section 4.4). To this aim the system is initialized by a homogeneous distribution of test-particles in a finite box with a momentum distribution close to a thermal one. Note that in PHSD the system cannot directly be initialized by a temperature and chemical potential since these 'Lagrange parameters' can only be determined when the system has reached a thermal and chemical equilibrium, i.e. when all forward and backward reaction rates have become equal.

4.3. System evolution

The dynamical evolution of the system is entirely described by the transport dynamics in PHSD incorporating the off-shell propagation of the partonic quasiparticles according to Refs. [26, 33] (Section 2.7) as well as the transition to resonant hadronic states (or 'strings') via Eq. (85). The time integration for the test-particle-equations of motion (cf. Eqs. (59), (60), (61)) is performed in the same way as in case of hadronic off-shell transport, where (in view of the presently momentum-independent width γ) the simple relation (64) is employed. For the collisions of partons two variants are at our disposal: i) geometrical collision criteria as used in standard hadronic transport, ii) the in-cell method developed in Ref. [50]. The latter can easily be extended to describe $2 \leftrightarrow 3$ or $1 \leftrightarrow 3$ processes etc. in a covariant way [51] and is the better choice at high particle densities (cf. Refs. [52, 53, 54]). The hadronization is performed by integrating the rate equations (e.g. (85)) in space and time which are discretized on a four-dimensional grid by Δt and $\Delta V(t) = \Delta x(t)\Delta y(t)\Delta z(t)$. In beam direction we use an initial grid size $\Delta z = 1/\gamma_{cm}$ fm with γ_{cm} denoting the Lorentz-γ factor in the nucleon-nucleon center-of-mass system while in the transverse direction we use $\Delta x = \Delta y = 1$ fm. The grid size is increased dynamically during the transport calculation such that all particles are included on the actual grid. This practically implies that the grid boundary in beam direction approximately moves with the velocity of light. In each time step Δt

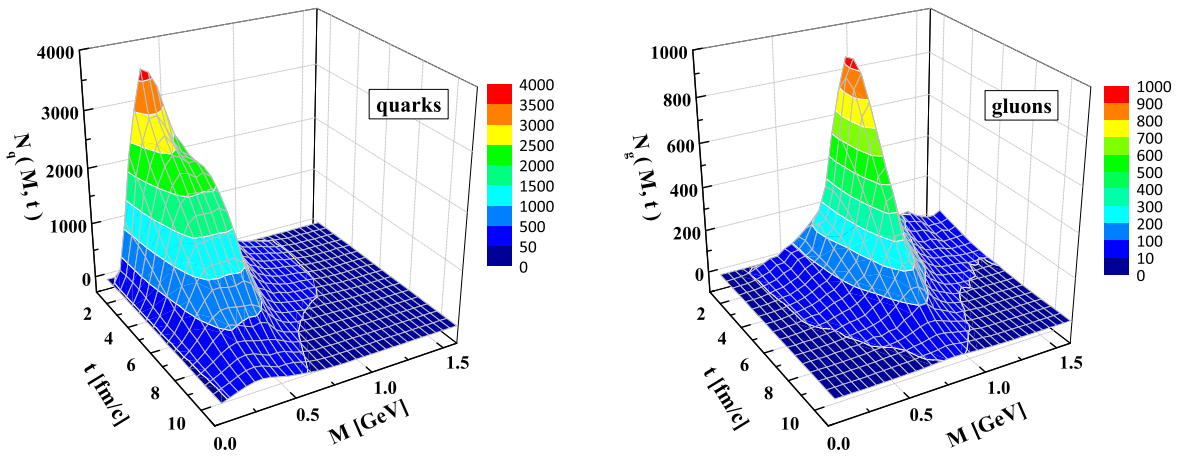


Figure 5: The time-dependent mass distributions for quarks (+ antiquarks) (l.h.s.) and gluons (r.h.s.) for a central Au+Au collision at $\sqrt{s} = 200$ GeV and b=1 fm at midrapidity ($|y| \leq 1$). The figures are taken from Ref. [32].

and cell ΔV the integrals in (85) and the respective integrals for baryon (antibaryon) formation are evaluated by a sum over all (time-like) test-particles using (e.g. for the quark density)

$$\frac{1}{\Delta V}\int_{\Delta V} d^3x \int_{-\infty}^{\infty} \frac{d\omega_q}{2\pi}\, 2\omega_q \int_{-\infty}^{\infty} \frac{d^3p_q}{(2\pi)^3}\, \rho_q(\omega_q, p_q)\; \tilde{N}_q(x, p_q) = \frac{1}{\Delta V} \sum_{J_q \text{ in } \Delta V} 1 \;=\; \rho_q(\Delta V)\;, \tag{90}$$

where the sum over J_q implies a sum over all test-particles of type q (here quarks) in the local volume ΔV in each parallel run. In Eq. (90) $\tilde{N}$ denotes the occupation number in phase space which in thermal equilibrium is given by Bose- or Fermi-functions, respectively. In case of other operators like the scalar density, energy density etc. the number 1 in Eq. (90) has to be replaced by $\sqrt{P_J^2}/\omega_J$, ω_J etc. In order to obtain lower numerical fluctuations the integrals are averaged over the parallel runs (typically 50 at RHIC energies). For each individual test-particle (i.e. x_q and p_q fixed) the additional integrations in Eq. (85) give a probability for a hadronization process to happen; the actual event then is selected by a Monte Carlo algorithm. Energy-momentum conservation fixes the four-momentum p of the hadron produced and its space-time position x is determined by (85). The final state is either a hadron with flavor content fixed by the fusing quarks (and/or antiquarks) or by a string of invariant mass $\sqrt{s}$ (with the same flavor), if $\sqrt{s}$ is above 1.3 GeV for mesonic or above 1.5 GeV for baryonic quark content.

On the partonic side the following elastic and inelastic interactions are included in PHSD $qq \leftrightarrow qq$, $\bar{q}\bar{q} \leftrightarrow \bar{q}\bar{q}$, $gg \leftrightarrow gg$, $gg \leftrightarrow g$, $q\bar{q} \leftrightarrow g$, $qg \leftrightarrow qg$, $g\bar{q} \leftrightarrow g\bar{q}$ exploiting 'detailed-balance' with interaction rates again from the DQPM [31, 42]. Partonic reactions such as $g + q \leftrightarrow q$ or $g + g \leftrightarrow q + \bar{q}$ have been discarded in the actual calculations due to their low rates since the large mass of the gluon leads leads to a strong mismatch in the energy thresholds between the initial and final channels. On the other hand the evaluation of photon and dilepton production is calculated perturbatively and channels like $g + q \to q + \gamma$ are included. In this case the probability for photon (dilepton) production from each channel is added up and integrated over space and time (Sections 5 - 7).

Numerical tests of the parton dynamics with respect to conservation laws, interaction rates in and out-off equilibrium in a finite box with periodic boundary conditions have been presented in Ref. [55]. In fact, in Ref. [55] it was shown that the PHSD calculations 'in the box' give practically the same results in equilibrium as the DQPM. We note in passing that the total energy is conserved in the box calculations up to about 3 digits while in the heavy-ion collisions addressed here in the following the violation of energy conservation is typically less than 1 % [31].

For illustration of the parton dynamics we display the time evolution of the quark and gluon distributions in mass for a central Au + Au collision at $\sqrt{s_{NN}} = 200$ GeV in Fig. 5 which shows the number of 'particles' as a function of invariant mass M and time t at midrapidity ($|y| \leq 1$). Note that by integration over M one obtains the number of quarks (+ antiquarks) $N_q(t)$ and gluons $N_g(t)$ in the rapidity interval $|y| \leq 1$ while dividing by

$N_q(t)$ and $N_g(t)$, respectively, an estimate for the particle spectral functions is obtained. Note that the mass distributions displayed here are the product of the spectral functions and the occupation numbers in a restricted phase space. Due to a moderate variation of the partons pole mass and width with the scalar density ρ_s the shapes of the partonic mass distributions do not change very much in time. The average quark mass is about 0.5 GeV while the average gluon mass is only slightly less than 1 GeV. Note, however, that the width of the mass function - which reflects the actual interaction rate per parton - remains significant for all times up to hadronization.

4.4. Transport coefficients of the QGP

The evaluation of transport coefficients can be performed in different ways and is usually performed by evaluating the temporal decay of correlators in the Kubo formalism [56, 57]. However, the results do not differ very much from those in the relaxation time approximation (RTA) which is easier to work out. We will thus focus on the latter approximation in this review for brevity.

Shear and bulk viscosities in the relaxation time approximation

The starting hypothesis of the relaxation time approximation is that the collision integral can be approximated (linearized) by

$$C[f] = -\frac{f - f^{eq}}{\tau} =: -\gamma(f - f^{eq}), \tag{91}$$

where τ is the relaxation time and f^{eq} the equilibrium distribution. In this approach it has been shown that the shear and bulk viscosities (without mean-field or potential effects) can be written as (e.g. in Ref. [58]):

$$\eta = \frac{1}{15T}\sum_a \int \frac{d^3p}{(2\pi)^3}\frac{|\mathbf{p}|^4}{E_a^2}\tau_a(E_a) f_a^{eq}(E_a/T), \tag{92}$$

$$\zeta = \frac{1}{9T}\sum_a \int \frac{d^3p}{(2\pi)^3}\ \frac{\tau_a(E_a)}{E_a^2}\big[(1-3v_s^2)E_a^2 - M_a^2\big] f_a^{eq}(E_a/T), \tag{93}$$

where the sum is over particles of different type a (in our case, $a = q, \bar{q}, g$). In the PHSD transport approach the relaxation time can be expressed in the following way:

$$\tau_a = \gamma_a^{-1}, \tag{94}$$

where γ_a is the width of particles of type $a = q, \bar{q}, g$, defined by Eq. (69). In our numerical simulation the volume V averaged shear and bulk viscosities assume the following expressions:

$$\eta = \frac{1}{15TV}\sum_{i=1}^{N}\frac{|\mathbf{p}_i|^4}{E_i^2}\gamma_i^{-1}, \qquad \zeta = \frac{1}{9TV}\sum_{i=1}^{N}\frac{\gamma_i^{-1}}{E_i^2}\big[(1-3v_s^2)E_i^2 - M_i^2\big]^2, \tag{95}$$

where the speed of sound $v_s = v_s(T)$ is taken from the DQPM using

$$v_s^2 = \frac{\partial P}{\partial \epsilon}. \tag{96}$$

In Fig. 6 we present the shear viscosity to entropy density ratio η/s as a function of the temperature of the system extracted from the PHSD simulations in the box employing different methods: the relaxation time approximation (red line+diamonds) and the Kubo formalism (blue line+dots). For comparison, the results from the virial expansion approach (green line) [59] and lattice QCD data for pure $SU_c(3)$ gauge theory are shown as a function of temperature, too.

In the absence of the chemical potential there should be no consideration of vector or tensor fields, only scalar fields. This affects the bulk viscosity, but not the shear viscosity. The expression for the bulk viscosity with potential effects is [58]

$$\zeta \;=\; \frac{1}{T}\sum_a \int \frac{d^3p}{(2\pi)^3}\frac{\tau_a(E_a)}{E_a^2} f_a^{eq}(E_a/T)\Big[\Big(\frac{1}{3} - v_s^2\Big)|\mathbf{p}|^2 - v_s^2\Big(M_a^2 - T^2\frac{d(M_a^2)}{d(T^2)}\Big)\Big]^2. \tag{97}$$

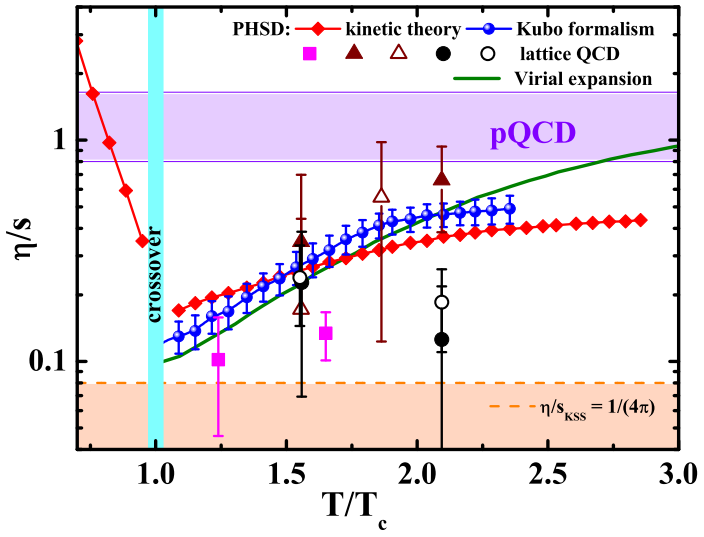


Figure 6: The shear viscosity to entropy density ratio η/s as a function of temperature of the system obtained by the PHSD simulations using different methods: the relaxation time approximation (red line+diamonds) and the Kubo formalism (blue line+dots). The others symbols denote lattice QCD data for pure $SU_c(3)$ gauge theory from different sources. The orange dashed line demonstrates the Kovtun-Son-Starinets bound $(\eta/s)_{KSS} = 1/(4\pi)$. For comparison, the results in the virial expansion approach (solid green line) [59] are shown as a function of temperature. The figure is taken from Ref. [60].

In the numerical simulation the volume averaged bulk viscosity with mean-field effects is calculated as

$$\zeta = \frac{1}{TV}\sum_{i=1}^{N}\frac{\gamma_i^{-1}}{E_i^2}\Big[\Big(\frac{1}{3}-v_s^2\Big)|\mathbf{p}|^2 - v_s^2\Big(M_i^2 - T^2\frac{d(M_i^2)}{d(T^2)}\Big)\Big]^2. \tag{98}$$

Using the DQPM expressions for masses of quarks and gluons (67) and (68), we can calculate the derivative $d(M^2)/d(T^2)$ as well as v_s^2 according to Eq. (96). For the actual results we refer the reader to Fig. 7 (l.h.s.), where the bulk viscosity to entropy density ratio ζ/s is presented as a function of temperature of the system extracted from the PHSD simulations in the box using the relaxation time approximation including mean-field effects (red line+diamonds) and without potential effects (blue line+open triangles). The r.h.s. of Fig. 7 shows the bulk to shear viscosity ratio as a function of temperature. Let us stress that contrary to η/s, the ratio ζ/s has a maximum close to T_c.

Electric conductivity

Whereas shear and bulk viscosities of hot QCD matter at finite temperature T presently are roughly known, the electric conductivity $\sigma_0(T, \mu_q)$ is a further macroscopic quantity of interest since it controls the electromagnetic emissivity of the plasma. First results from lattice calculations on the electromagnetic correlator have provided results that varied by more than an order of magnitude. Furthermore, the conductivity dependence on the temperature T (for $T>T_c$) is widely unknown, too, as well as its dependence on μ_q. The electric conductivity σ_0 is also important for the creation of electromagnetic fields in ultra-relativistic nucleus-nucleus collisions from partonic degrees-of-freedom, since σ_0 specifies the imaginary part of the electromagnetic (retarded) propagator and leads to an exponential decay of the propagator in time $\sim\exp(-\sigma_0(t-t')/(\hbar c))$.

In order to include the effects from an external electric field $\mathbf{E}$ or magnetic field $\mathbf{B}$ on the charged degrees-of-freedom, the propagation of each charged test-particle j in the PHSD is performed with the additional Lorentz force in the equation of motion:

$$\frac{d}{dt}\mathbf{p}^j = q_j e(\mathbf{E} + \frac{\mathbf{p}^j}{E^j}\times\mathbf{B}), \tag{99}$$

where q_j denotes the fractional charge of the test-particle $(\pm 1/3, \pm 2/3)$ and E^j its energy. We recall that the external electric field will lead to an acceleration of positively and negatively charged particles in opposite directions while the particle scatterings/interactions will damp this acceleration and eventually lead to an

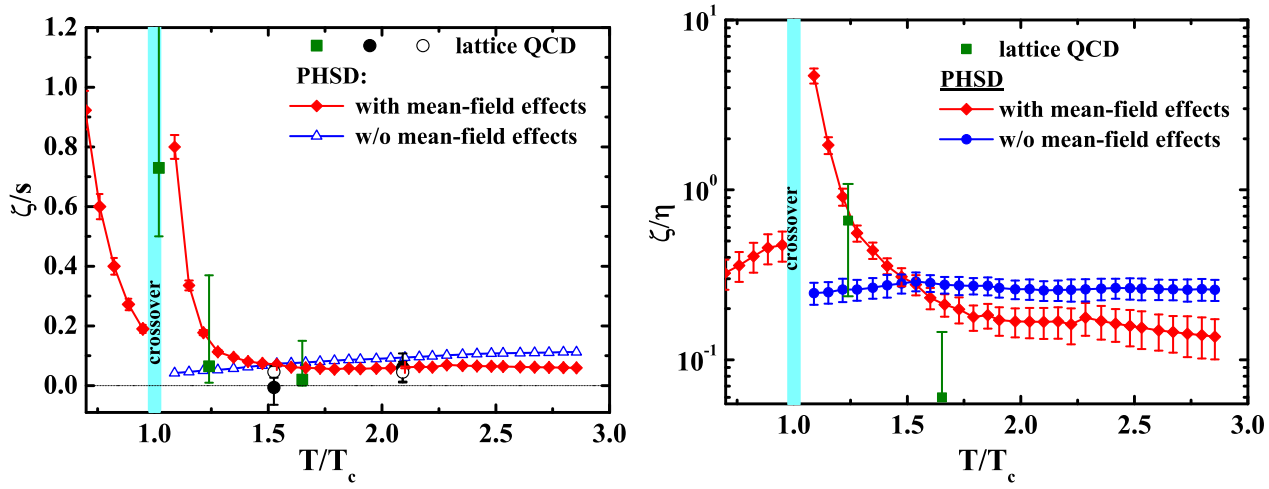


Figure 7: (l.h.s.) The bulk viscosity to entropy density ratio ζ/s as a function of temperature of the system extracted from the PHSD simulations in the box using the relaxation time approximation including mean-field effects (red line+diamonds) and without potential effects (blue line+open triangles). The other symbols show the available lattice QCD data from different sources (r.h.s.). The bulk to shear viscosity ratio as a function of temperature as obtained by the PHSD simulations in the box employing the relaxation time approximation including mean-field effects (red line+diamonds) and without potential effects (blue line+circles). Figures taken from Ref. [60].

equilibrium current if the external field is of moderate strength. The electric current density $j_z(t)$ (for an external electric field in z-direction) is calculated by

$$j_z(t) = \frac{1}{VN} \sum_{k=1}^{N} \sum_{j=1}^{N_k(t)} eq_j \frac{p_z^j(t)}{E_j(t)}. \tag{100}$$

The summation in (100) is carried out over N ensemble members $k = 1 \dots N$ while $N_k(t)$ denotes the time-dependent number of 'physical' (u, d, s) quarks and antiquarks that varies with time t due to the processes $q + \bar{q} \leftrightarrow g \leftrightarrow q' + \bar{q}'$ in a single member of the ensemble (run). The number of runs N is typically taken as a few hundred which gives a current $j_z(t)$ practically independent on the number of ensemble members N. We recall that (without external fields) each run of the ensemble is a micro-canonical simulation of the dynamics as inherent in the PHSD transport approach which strictly conserves the total four-momentum as well as all discrete conservation laws (e.g. net fermion number for each flavor etc.). A note of caution has to be given, since due to an external field we deal with an open system with increasing energy density (temperature) in time. Therefore we employ sufficiently small external fields eE_z, such that the energy increase during the computation time (in each run) stays below 2% and the increase in temperature below 1 MeV. For the details we refer the reader to Refs. [61, 62].

We find that for constant electric fields up to $eE_z = 50$ MeV/fm a stable electric current j_{eq} emerges that is $\sim E_z$. Accordingly, we obtain the conductivity $\sigma_0(T, \mu_q)$ from the ratio of the stationary current density j_{eq} and the electric field strength as

$$\frac{\sigma_0(T, \mu_q)}{T} = \frac{j_{eq}(T, \mu_q)}{E_z T} \ . \tag{101}$$

The results for the dimensionless ratio (101) at $\mu_q = 0$ are displayed in Fig. 8 by the full dots as a function of the scaled temperature T/T_c in comparison to recent lattice QCD results and suggest a minimum in the ratio $\sigma_0(T, \mu_q = 0)/T$ close to the critical temperature T_c followed by an approximate linear rise up to 2 T_c. The recent lQCD results are roughly compatible with the PHSD predictions.

Within PHSD (or the DQPM) also the dependence of the electrical conductivity on the quark chemical potential can be evaluated [62]. The numerical result could be fitted by a quadratic correction

$$\frac{\sigma_0(T, \mu_q)}{T} = \frac{\sigma_0(T, \mu_q = 0)}{T} \left(1 + a(T)\mu_q^2\right) \tag{102}$$

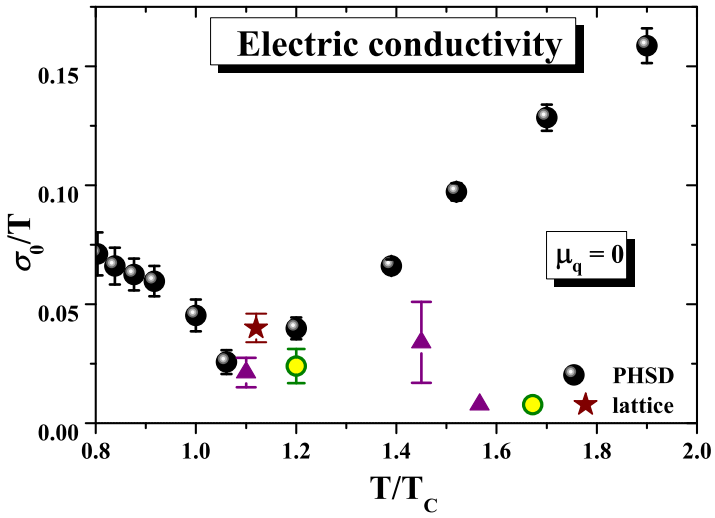


Figure 8: The dimensionless ratio of electric conductivity over temperature σ_0/T (101) as a function of the scaled temperature T/T_c for $\mu_q = 0$ in comparison to recent lattice QCD results. The figure is taken from Ref. [61].

with $a(T) \approx 11.6$ GeV^{-2} for $T = 0.2$ GeV. This result comes about as follows: We recall that the electric conductivity of gases, liquids and solid states is described in the relaxation time approach by the Drude formula,

$$\sigma_0 = \frac{e^2 n_e \tau}{m_e^*}, \tag{103}$$

where n_e denotes the density of non-localized charges, τ is the relaxation time of the charge carriers in the medium and m_e^* their effective mass. This expression can be directly computed for partonic degrees-of-freedom within the DQPM, which matches the quasiparticles properties to lattice QCD results in equilibrium. In the DQPM, the relaxation time for quarks/antiquarks is given by $\tau = 1/\gamma_q(T, \mu_q)$, where $\gamma_q(T, \mu_q)$ is the width of the quasiparticle spectral function (69). Furthermore, the spectral distribution for the mass of the quasiparticle has a finite pole mass $M_q(T, \mu_q)$ that is also fixed in the DQPM (68) as well as the density of $(u, \bar{u}, d, \bar{d}, s, \bar{s})$ quarks/antiquarks as a function of temperature T and chemical potential μ_q. The latter is given by an expression similar to the scalar density ρ_s in (73) but $\sqrt{p^2}$ replaced by ω. Thus, we obtain for the dimensionless ratio (101) the expression

$$\frac{\sigma_0(T, \mu_q)}{T} \approx \frac{2}{9} \frac{e^2 n_{q+\bar{q}}(T, \mu_q)}{M_q(T, \mu_q)\gamma_q(T, \mu_q)T}, \tag{104}$$

where $n_{q+\bar{q}}(T, \mu_q)$ denotes the total density of quarks and antiquarks and the pre-factor 2/9 reflects the flavor averaged fractional quark charge squared $(\sum_f q_f^2)/3$. As found in Ref. [62] the DQPM results match well with the explicit PHSD calculations in the box also for finite μ_q since PHSD in equilibrium is a suitable transport realization of the DQPM. In the DQPM we have $\gamma_q(T, \mu_q) \approx \gamma_q(T, \mu_q = 0)$ and $M_q(T, \mu_q) \approx M_q(T, \mu_q = 0)$ for $\mu_q \leq 100$ MeV, however,

$$n_{q+\bar{q}}(T, \mu_q) \approx n_{q+\bar{q}}(T, \mu_q = 0) \left(1 + a(T)\mu_q^2\right) \tag{105}$$

with the same coefficient $a(T)$ as in Eq. (102).

The temperature dependence of the expansion coefficient $a(T)$ is found to be $\sim 1/T^2$ such that the ratio σ_0/T can be approximated by

$$\frac{\sigma_0(T, \mu_q)}{T} \approx \frac{\sigma_0(T, \mu_q = 0)}{T} \left(1 + c_{\sigma_0} \frac{\mu_q^2}{T^2}\right). \tag{106}$$

A fit to the coefficient c_{σ_0} in the temperature range 170 MeV$\leq T \leq$ 250 MeV gives $c_{\sigma_0} \approx 0.46$. This completes our study on the stationary electric conductivity σ_0 which can be well understood in its variation with T and μ_q within the DQPM or PHSD, respectively. We note that the conductivity σ_0 controls the electromagnetic emissivity of systems in thermal equilibrium at low photon momentum (see Section 5.3).

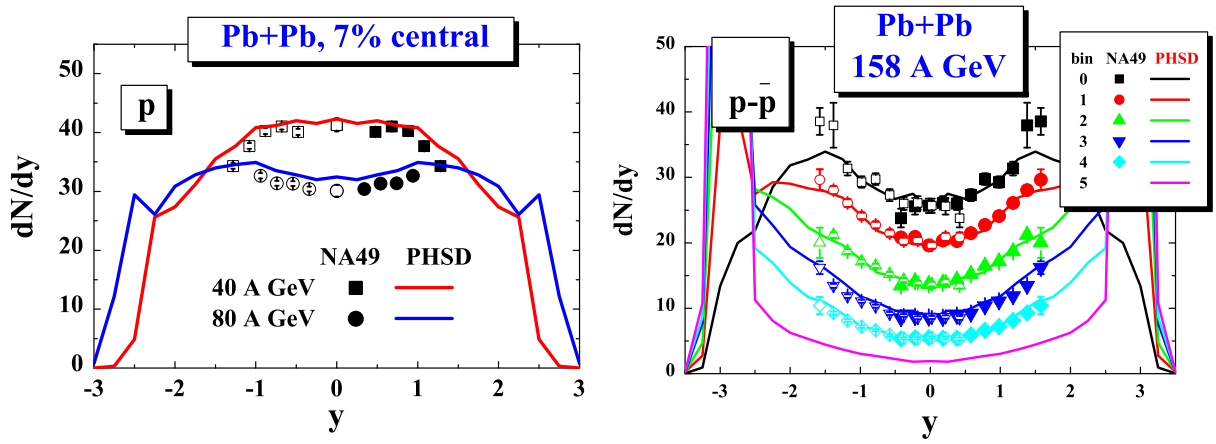


Figure 9: The proton rapidity distributions for central (7%) Pb+Pb collisions at 40 and 80 (l.h.s.) in comparison to the data from Ref. [63]. The r.h.s. of the figure presents the net-proton rapidity distribution at 158 A·GeV for different centrality bins (bin 0 – 0-5%; bin 1 – 5-12%; bin 2 – 12.5-23.5%; bin 3 – 23.5-33.5%; bin 4 – 33.5-43.5% and bin 5 – 43.5-78.5% central events) from PHSD (solid lines) in comparison to the experimental data from the NA49 Collaboration [64]. The figures are taken from Ref. [31].

4.5. Application to Au+Au or Pb+Pb collisions

In this Subsection we employ the PHSD approach to nucleus-nucleus collisions from $\sqrt{s_{NN}} = 5.5$ GeV to 2.76 TeV. Note that at RHIC or more specifically LHC energies other initial conditions (e.g. a color-glass condensate (CGC) [65, 66]) might be necessary. In the present work we discard such alternative initial conditions and explore to what extent the present initial conditions (described in Section 4.2) are compatible with differential measurements by the various collaborations at the SPS, RHIC or LHC. A more detailed comparison to results from CGC initial conditions in Pb-Pb collisions at $\sqrt{s_{NN}} = 2.76$ TeV may be found in Ref. [67].

Particle spectra in comparison to experiment

Since PHSD is essentially fixed by lQCD data at $\mu_q = 0$ in thermal equilibrium in the partonic phase and by HSD in the hadronic phase, it is of interest how the PHSD approach compares to the HSD model (without explicit interacting partonic degrees-of-freedom) as well as to experimental data from the SPS, RHIC or LHC collaborations. We start with proton rapidity distributions at the SPS that demonstrate the amount of initial baryon stopping and thus control the energy transfer in relativistic nucleus-nucleus collisions. Since we find the HSD results for the proton rapidity distribution dN/dy to be identical with the PHSD results (within statistics) we will only compare PHSD calculations to data of the NA49 Collaboration. Accordingly, in Fig. 9 the proton rapidity distributions from PHSD are compared to the data from Ref. [63] for 7% central Pb+Pb collisions at 40 and 80 A·GeV (l.h.s.). The r.h.s. of Fig. 9 shows the net-proton dN/dy from PHSD for 158 A·GeV Pb+Pb collisions for different centrality bins (bin 0 – 0-5%; bin 1 – 5-12%; bin 2 – 12.5-23.5%; bin 3 – 23.5-33.5%; bin 4 – 33.5-43.5% and bin 5 – 43.5-78.5% central events) in comparison to the experimental data from Ref. [64]. In fact, the PHSD results demonstrate that the baryon stopping is reasonably reproduced in Pb+Pb collisions as a function of bombarding energy and centrality of the reaction at the SPS energies. We note additionally that at SPS energies the antiprotons from HSD are about the same as from PHSD as well as $\Lambda + \Sigma^0$ and even Ξ^- baryons, however, the antibaryons with antistrangeness $\bar{\Lambda} + \bar{\Sigma}^0$ and $\bar{\Xi}^+$ are more abundant in PHSD than in HSD due to a large contribution from hadronization. For further details on the baryon/antibaryon sector in HSD and PHSD we refer the reader to Ref. [31].

Since the energy is dominantly transferred to mesons, which asymptotically appear mostly as pions and kaons, we continue with pion and $K^{\pm}$ rapidity distributions for 7% central Pb+Pb collisions at 40 and 80 A·GeV and 5% central collisions at 158 A·GeV since here rather complete data sets are available from the experimental side [68]. The results from PHSD (solid blue lines) are compared in Fig. 10 with the corresponding results from HSD (dashed red lines) and the experimental data for the same centralities in comparison to the rapidity spectrum from HSD (dashed red lines) and the experimental data from the NA49 Collaboration [68]. The actual deviations between the PHSD and HSD spectra are very moderate; the π^- rapidity distribution is slightly squeezed in width (in PHSD) and shows a more pronounced peak at midrapidity (at 158 A·GeV) more in line with the data. Nevertheless, it becomes clear from Fig. 10 that the energy transfer - reflected in the light

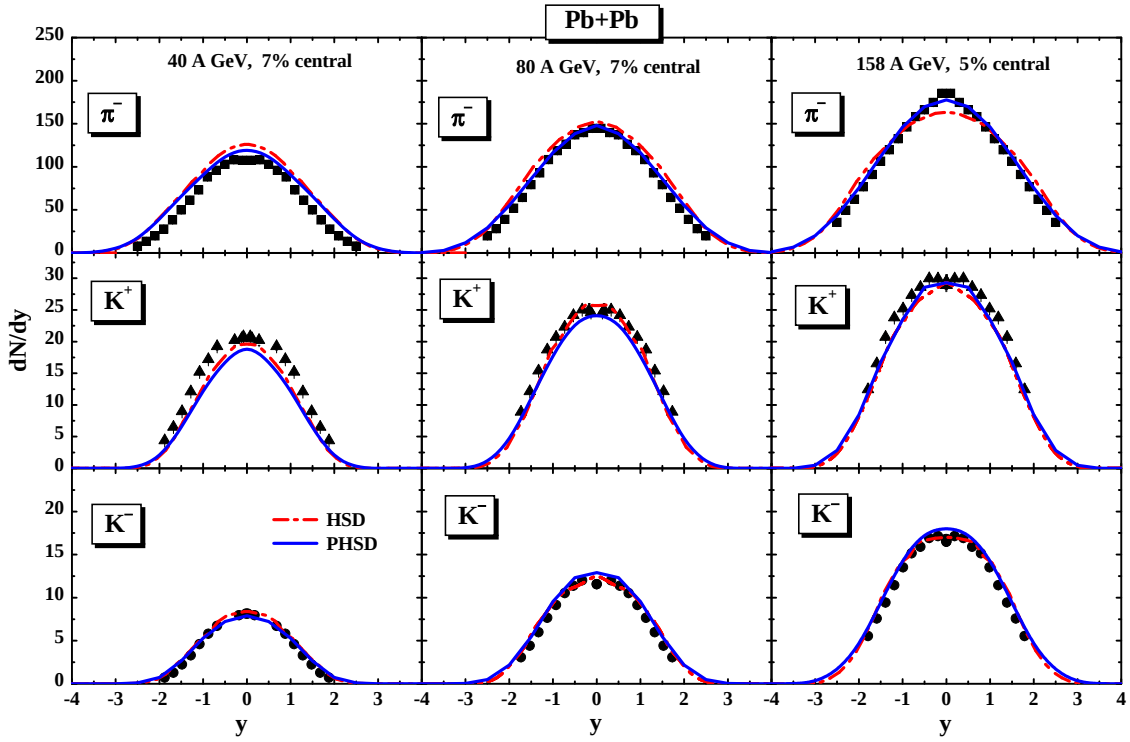


Figure 10: The rapidity distribution of π^- (upper part), K^+ (middle part) and K^- (lower part) for 7% or 5% central Pb+Pb collisions at 40, 80 and 158 A·GeV from PHSD (solid blue lines) in comparison to the distribution from HSD (dashed red lines) and the experimental data from the NA49 Collaboration [68, 69]. The figures are taken from Ref. [31].

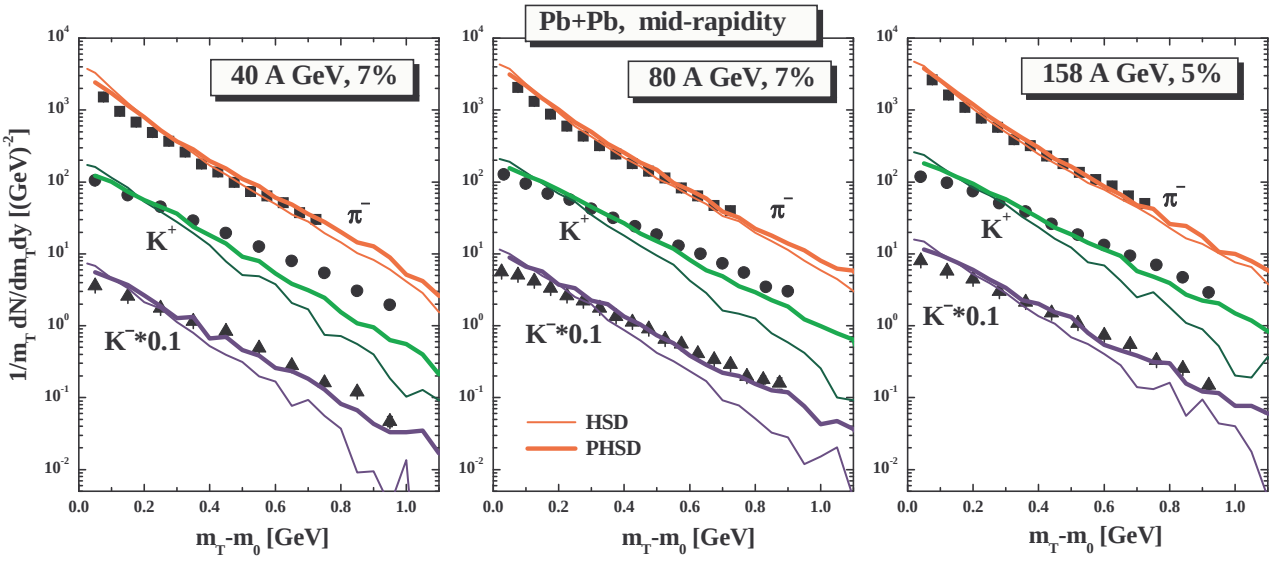


Figure 11: The π^-, K^+ and K^- transverse mass spectra for central Pb+Pb collisions at 40, 80 and 158 A·GeV from PHSD (thick solid lines) in comparison to the distributions from HSD (thin solid lines) and the experimental data from the NA49 Collaboration [68]. The figures are taken from Ref. [31].

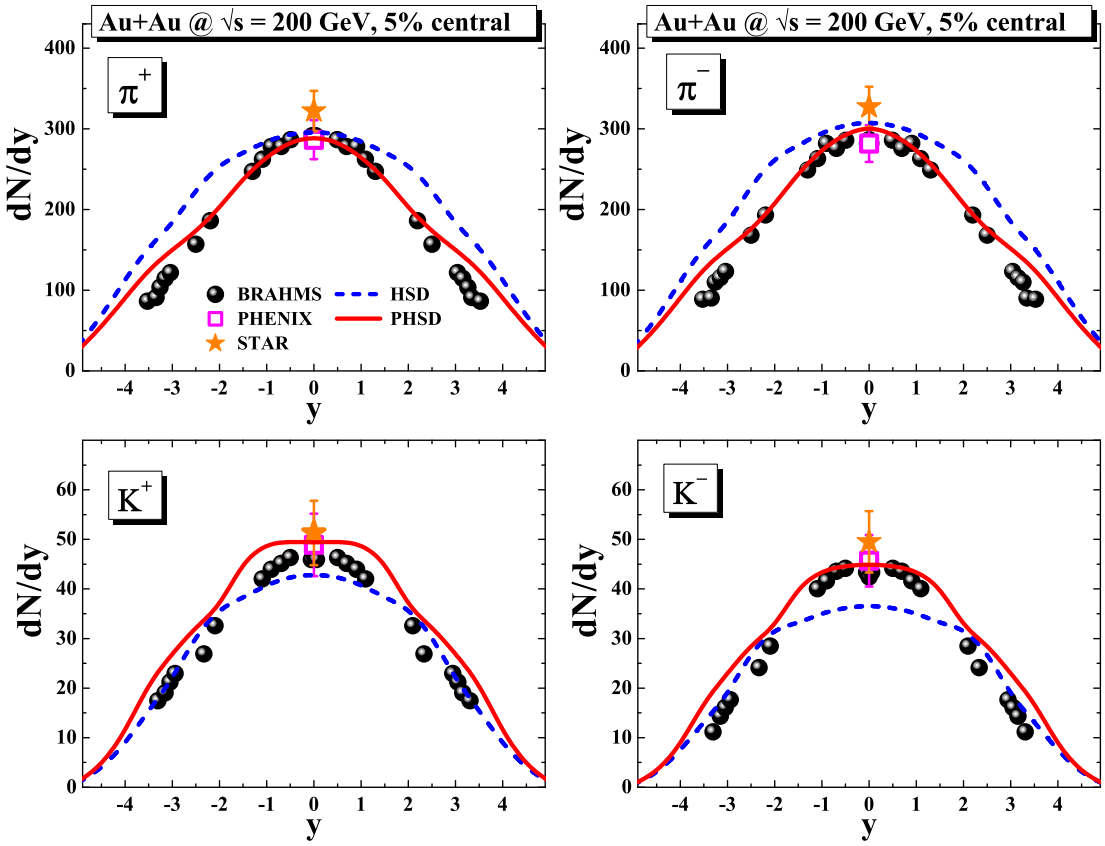


Figure 12: The rapidity distribution of π^+ (upper part, l.h.s.), K^+ (lower part, l.h.s.), π^- (upper part, r.h.s.) and K^- (lower part, r.h.s.) for 5% central Au+Au collisions at $\sqrt{s} = 200$ GeV from PHSD (solid lines) in comparison to the distribution from HSD (dashed lines) and the experimental data from the RHIC Collaborations [70, 71]. The figure is taken from Ref. [32].

meson spectra - is rather well described by PHSD, which thus passes another test. Fig. 10 demonstrates that the longitudinal motion is rather well understood within the transport approaches and dominated by initial string formation and decay. Actually, there is no sizeable sensitivity of the rapidity spectra to an intermediate partonic phase. But what about the transverse degrees-of-freedom?

The answer to this question is offered in Fig. 11 where we show the transverse mass spectra of π^-, K^+ and K^- mesons for 7% central Pb+Pb collisions at 40 and 80 A·GeV and 5% central collisions at 158 A·GeV in comparison to the data of the NA49 Collaboration [68]. Here the slope of the π^- spectra is only slightly enhanced in PHSD (thick solid lines) relative to HSD (thin solid lines) which demonstrates that the pion transverse mass spectra also show no sizeable sensitivity to the partonic phase. However, the $K^\pm$ transverse mass spectra are substantially hardened with respect to the HSD calculations at all bombarding energies - i.e. PHSD is more in line with the data - and thus suggest that partonic effects are better visible in the strangeness degrees-of-freedom. The hardening of the kaon spectra can be traced back to parton-parton scattering as well as a larger collective acceleration of the partons in the transverse direction due to the presence of repulsive fields for the partons. The enhancement of the spectral slope for kaons and anti-kaons in PHSD (due to collective partonic flow) shows up much clearer for the kaons due to their significantly larger mass (relative to pions). We recall that in Refs. [72, 73] the underestimation of the $K^\pm$ slope by HSD (and also UrQMD) had been suggested to be a signature for missing partonic degrees-of-freedom. In fact, the PHSD calculations support this early suggestion.

We continue with rapidity spectra from PHSD (solid red lines) for charged pions and kaons in 5% central Au+Au collisions at $\sqrt{s_{NN}} = 200$ GeV which are compared in Fig. 12 to the data from the RHIC Collaborations [70, 71] as well as to results from HSD (dashed blue lines). We find the rapidity distributions of the charged mesons to be slightly narrower than those from HSD and actually closer to the experimental data. Also note

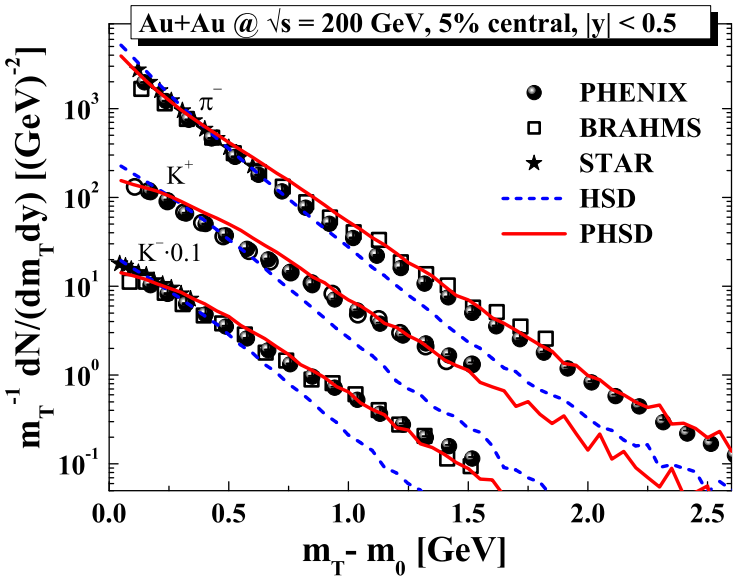


Figure 13: The π^-, K^+ and K^- transverse mass spectra for 5% central Au+Au collisions at $\sqrt{s} = 200$ GeV from PHSD (solid lines) in comparison to the distributions from HSD (dashed lines) and the experimental data from the BRAHMS, PHENIX and STAR Collaborations [70, 71]. The figure is taken from Ref. [32].

that there is slightly more production of $K^{\pm}$ mesons in PHSD than in HSD while the number of charged pions is slightly lower. The actual deviations between the PHSD and HSD spectra are not dramatic but more clearly visible than at SPS energies (cf. Figs. 8,9). Nevertheless, it becomes clear from Fig. 12 that the energy transfer in the nucleus-nucleus collision from initial nucleons to produced hadrons - reflected dominantly in the light meson spectra - is rather well described by PHSD also at the top RHIC energy.

Independent information on the active degrees-of-freedom is provided again by transverse mass spectra of the hadrons especially in central collisions. The PHSD results for the top RHIC energy are displayed in Fig. 13 where we show the transverse mass spectra of π^-, K^+ and K^- mesons for 5% central Au+Au collisions at $\sqrt{s}$ = 200 GeV in comparison to the data of the RHIC Collaborations [70, 71]. Here the slope of the π^- spectra is slightly enhanced in PHSD (solid red lines) relative to HSD (dashed blue lines) which demonstrates that the pion transverse mass spectra also show some sensitivity to the partonic phase (contrary to the SPS energy regime). The $K^{\pm}$ transverse mass spectra are substantially hardened with respect to the HSD calculations - i.e. PHSD is more in line with the data - and thus suggest that partonic effects are better visible in the strangeness degrees-of-freedom. The hardening of the kaon spectra can be traced back also to parton-parton scattering as well as a larger collective acceleration of the partons in the transverse direction due to the presence of the repulsive scalar mean-field for the partons.

We, finally, come to the presently highest laboratory energies for Pb+Pb collisions at the LHC, however, recall that the PHSD approach had to be properly upgraded to LHC energies with respect to a more recent PYTHIA 6.4 implementation [76]. The transition between the different PYTHIA regions in energy is smooth with respect to $\sqrt{s_{NN}}$ of the individual collisions such that PHSD preserves all results at lower bombarding energies where PYTHIA 6.4 does not work sufficiently well. In PYTHIA 6.4 we use the Innsbruck pp tune (390) which allows to describe reasonably the p-p collisions at $\sqrt{s_{NN}} = 7$ TeV in the framework of the PHSD transport approach (cf. Fig. 1 in Ref. [76]). The overall agreement with LHC experimental data for the distribution in the charged particle multiplicity N_{ch}, the charged particle pseudorapidity distribution, the transverse momentum p_T spectra and the correlation of the average p_T with the number of charged particles N_{ch} is satisfactory. Also a variety of observables from p-Pb collisions at $\sqrt{s_{NN}} = 5.02$ TeV compare quite well with the experimental observations [76].

One might ask whether the PHSD approach still works at LHC energies for nucleus-nucleus (Pb+Pb) collisions although the invariant energy is higher by about a factor of 13.8 compared to the top RHIC energy. In Fig. 14 (l.h.s.) we compare the average p_T (at midrapidity) as a function of charged multiplicity N_{ch} in p+p

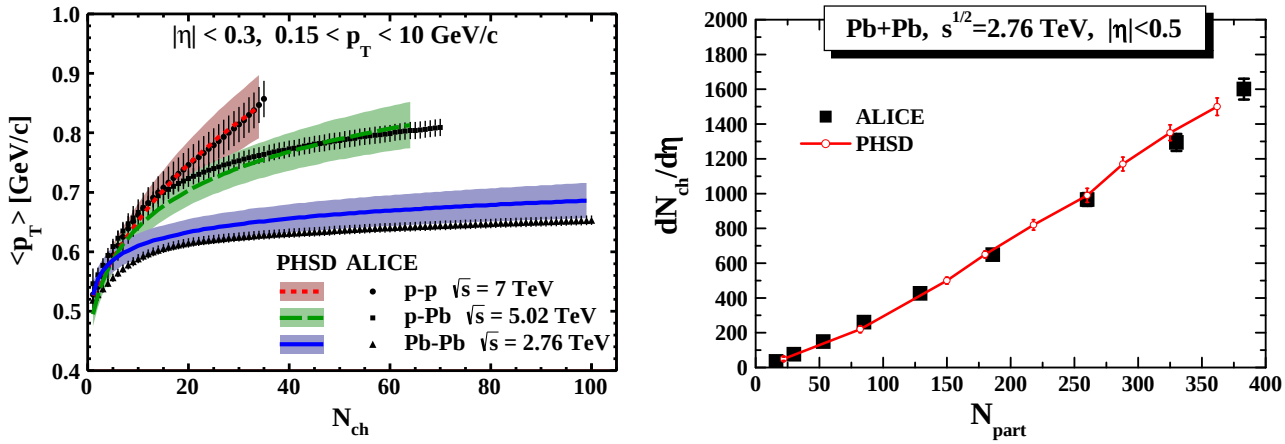


Figure 14: (l.h.s.) Mean p_T results for p-p, p-Pb and Pb-Pb collisions from the PHSD transport approach in comparison to the ALICE experimental data from Ref. [74] at midrapidity. Note the different invariant energies for p-p, p-Pb and Pb-Pb collisions. (r.h.s.) Pseudo-rapidity distribution of charged hadrons $dN_{ch}/d\eta$ at midrapidity as a function of the number of participants N_{part} from PHSD (solid line) in comparison to the data from the ALICE Collaboration [75] for Pb+Pb at $\sqrt{s_{NN}}$= 2.76 TeV. The figures are taken from Ref. [67].

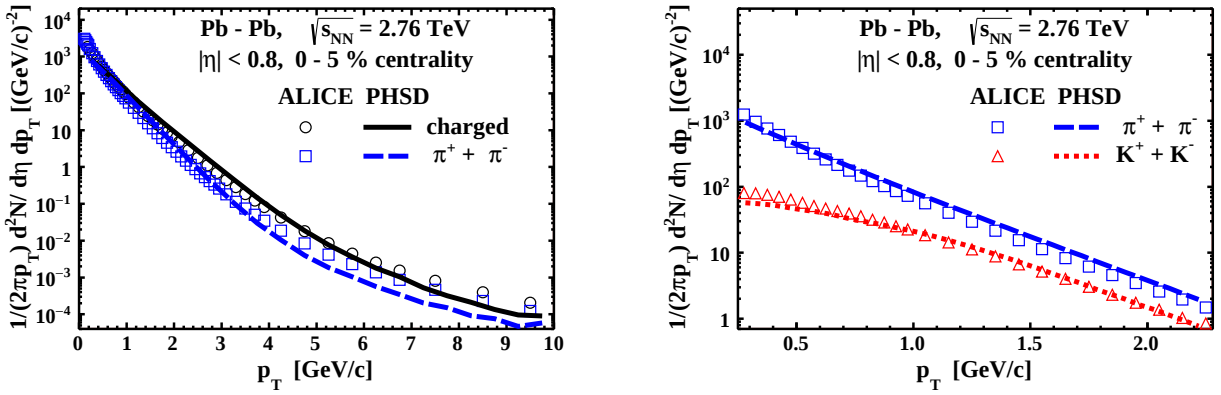


Figure 15: (l.h.s.) Transverse momentum spectra from PHSD in comparison to the results of the ALICE Collaboration for all charged particles [77, 78] (solid line) as well as for charged pions [79] (dashed line). (r.h.s.) Transverse momentum spectra from PHSD for $p_T \leq 2$ GeV/c in comparison to the results of the ALICE Collaboration [77, 78, 79] for pions and kaons. The figures are taken from Ref. [67].

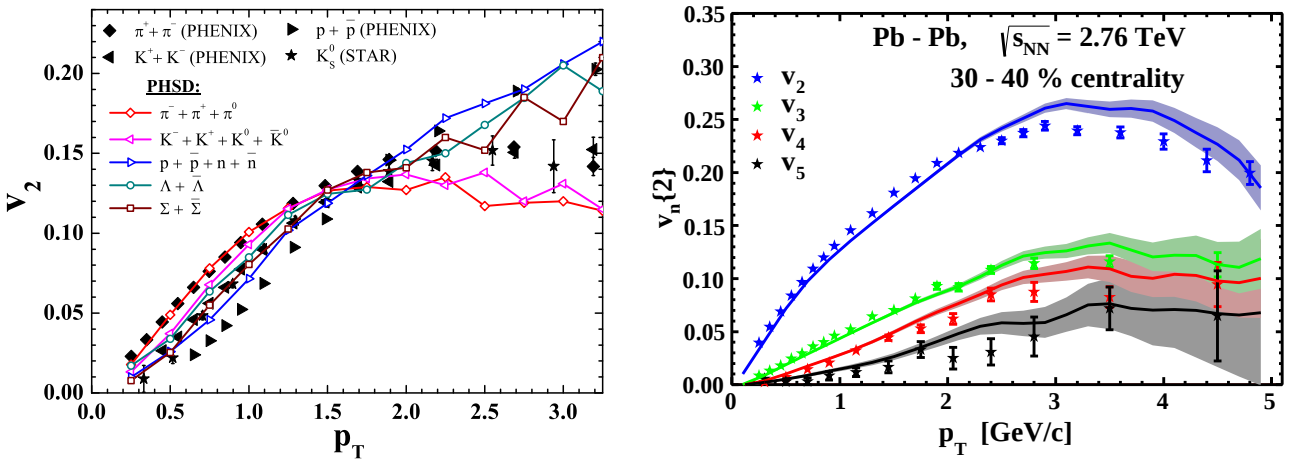


Figure 16: (l.h.s.) The hadron elliptic flow v_2 for inclusive Au+Au collisions as a function of the transverse momentum p_T (in GeV) for different hadrons in comparison to the data from the STAR [80, 81] and PHENIX Collaborations [82] within the same rapidity cuts. (r.h.s.) The flow coefficients v_2, v_3, v_4 and v_5 of all charged particles as a function of p_T for the centralities 30-40% in case of Pb-Pb collisions at $\sqrt{s_{NN}}$ = 2.76 TeV. The ALICE data have been adopted from Ref. [75]. The figures are taken from Refs. [32, 67].

reactions at $\sqrt{s_{NN}}$ = 7 TeV, p+Pb collisions at $\sqrt{s_{NN}}$ = 5.02 TeV and Pb+Pb collisions at $\sqrt{s_{NN}}$ = 2.76 TeV from the PHSD to the experimental data from Ref. [74]. Note that for low multiplicities ($N_{ch} < 5$) the mean p_T is almost independent on energy (see also Ref. [74]) which in PHSD can be traced back to the fact that (for the acceptance $|\eta| \leq 0.3$, $0.15 \leq p_T \leq 10$ GeV/c) only events with one or two binary collisions N_{bin} are selected for all systems. Actually, the correlation $< p_T > (N_{ch})$ only weakly depends on $\sqrt{s_{NN}}$ for pp reactions at these LHC energies, however, when plotting $p_T(N_{ch})$ on an event-by-event basis, large fluctuations in p_T or N_{ch} are obtained within PHSD. The same holds true for p+Pb and Pb+Pb reactions where a fixed N_{ch} can be obtained by reactions with a varying number of binary collisions N_{bin}. Each of these binary reactions then has a low N_{ch} and $< p_T >$, respectively. The ensemble average finally leads to the average correlation shown in Fig. 14 (l.h.s.). Nevertheless, the agreement between data and calculations (within the statistical accuracy) is encouraging. Note again that only very peripheral Pb+Pb collisions are probed for $N_{ch} < 100$.

In order to shed some light on the centrality dependence of charged particle production we display in Fig. 14 (r.h.s.) the results for the pseudo-rapidity distribution $dN_c/d\eta$ at midrapidity from the default PHSD calculations in comparison to the ALICE data as a function of the number of participants N_{part} that has been determined dynamically in the PHSD calculations. A quite acceptable agreement is seen, suggesting that the bulk parton dynamics is not much different at top RHIC and LHC energies.

We continue with the transverse momentum spectra for central Pb+Pb reactions at $\sqrt{s_{NN}}$ = 2.76 TeV (0-5% centrality) which are compared in Fig. 15 with results from the ALICE Collaboration for all charged particles [77, 78] (PHSD: black solid line) as well as for charged pions [79] (PHSD: dashed blue line). Note that except for the upgrade in the PYTHIA version no additional parameters or changes have been introduced in the PHSD. In this respect the approximate reproduction of the midrapidity p_T spectra for central collisions over 7 orders of magnitude in Fig. 15 (l.h.s.) is quite remarkable. A closer look at the low momentum spectra is offered in Fig. 15 (r.h.s.) where the PHSD spectra for pions and kaons are compared to results of the ALICE Collaboration [77, 78, 79] (symbols).

In summarizing, the partonic phase in PHSD at the top RHIC energy and at LHC leads to a narrowing of the longitudinal momentum distribution, a reduction of pion production, a slight enhancement of kaon production and to a hardening of their transverse mass spectra relative to HSD (closer to the data). These effects are clearly visible especially in the transverse degrees-of-freedom and are more pronounced than at SPS energies due to the larger space-time region of the partonic phase.

Collective flow

Of additional interest are the collective properties of the strongly interacting system which are explored experimentally by the azimuthal momentum distribution of particles in a fixed rapidity interval. The azimuthal

momentum distribution of the emitted particles is commonly expressed in the form of a Fourier series as

$$E\frac{d^3N}{d^3p} = \frac{d^2N}{2\pi p_T dp_T dy}\left(1+\sum_{n=1}^{\infty} 2v_n(p_T)\cos[n(\psi-\Psi_n)]\right), \tag{107}$$

where v_n is the magnitude of the n'th order harmonic term relative to the angle of the initial-state spatial plane of symmetry Ψ_n and $p=(E,\vec{p})$ is the four-momentum of the particle under consideration. We here focus on the coefficients v_2, v_3 and v_4 which implies that we have to perform event-by-event calculations in order to catch the initial fluctuations in the shape of the interaction zone and the event plane Ψ_{EP}; e. g., we calculate the triangular flow v_3 with respect to Ψ_3 as $v_3\{\Psi_3\} = \langle\cos(3[\psi-\Psi_3])\rangle/\mathrm{Res}(\Psi_3)$. The event plane angle Ψ_3 and its resolution $\mathrm{Res}(\Psi_3)$ are evaluated as described in Ref. [83] via the two-sub-events method [84, 85].

We here briefly summarize the main results. Fig. 16 (l.h.s.) shows the final hadron v_2 versus the transverse momentum p_T for different particle species at the top RHIC energy in comparison to the data from the STAR [80, 81] and PHENIX Collaborations [82]. We observe a mass separation in p_T as well as a separation in mesons and baryons for $p_T > 2$ GeV roughly in line with data. The elliptic flow of mesons is slightly underestimated for $p_T > 2$ GeV in PHSD which is opposite to ideal hydrodynamics which overestimates v_2 at high transverse momenta. On the other hand, the proton (and antiproton) elliptic flow is slightly overestimated at low $p_T < 1.5$ GeV. We note in passing that also the momentum integrated results for v_2 as a function of the number of participating nucleons N_{part} from PHSD compare well to the data from Ref. [86]. In contrast, the HSD results clearly underestimate the elliptic flow as pointed out before [87]. The relative enhancement of v_2 in PHSD with respect to HSD can be traced back to the high interaction rate in the partonic phase and to the repulsive scalar mean-field for partons; the PHSD calculations without mean-fields only give a small enhancement for the elliptic flow relative to HSD.

Stepping up in energy of the collision to $\sqrt{s_{NN}} = 2.76$ TeV reached at the LHC, the PHSD results for the flow coefficients v_2, v_3, v_4 and v_5 of all charged particles are shown in Fig. 16 as a function of p_T for the centralities 30-40% in Pb+Pb collisions (r.h.s.) in comparison to the ALICE data from Ref. [75]. The PHSD results for $v_2(p_T), v_3(p_T)$ and $v_4(p_T)$ describe the data reasonably up to about 3.5 GeV/c, whereas at higher transverse momenta the statistics of the present calculations is insufficient to draw robust conclusions. This also holds for the flow coefficient v_5 which still is in line with the data within error bars. It is quite remarkable that the collective behavior is reproduced in the PHSD approach not only for the semi-central collisions ($30-40$ %) but also for $0-5$% central collisions, which are sensitive to the initial state fluctuations (see Ref. [67]).

These tests indicate that the 'soft' physics at LHC in central A-A reactions is very similar to the top RHIC energy regime although the invariant energy is higher by more than an order of magnitude. Furthermore, the PHSD approach seems to work from lower SPS energies up to LHC energies for p-p, p-A as well as A-A collisions, i.e. over a range of more than two orders in $\sqrt{s_{NN}}$. Note that for even lower bombarding energies the PHSD approach merges to the HSD model which has been successfully tested from the SIS to the SPS energy regime in the past [39, 88, 89]. Since the bulk dynamics is well described in PHSD in comparison to experimental data in a wide dynamical range we may continue with the electromagnetic emissivity of the reactions which (in principle) does not employ any new parameter.

5. Implementation of photon and dilepton production in transport approaches

5.1. Photon sources in relativistic heavy-ion collisions

The *inclusive* photon yield as produced in $p+p$, $p+A$ and $A+A$ collisions is divided into "*decay* photons" and "*direct* photons". The *decay photons* – which constitute the major part of the *inclusive* photon spectrum – stem from the photonic decays of hadrons (mesons and baryons) that are produced in the reaction. These decays occur predominantly at later times and outside of the active reaction zone and therefore carry limited information on the initial high-energy state. Consequently, it is attempted to separate the *decay* photons from the inclusive yield (preferably by experimental methods) and to study the remaining "*direct* photons". One usually uses the "cocktail" method to estimate the contribution of the photon decays to the spectra and to the elliptic flow v_2, which relies (among others) on the m_T-scaling assumption and on the photon emission only by the finally produced hadrons with momentum distributions of the final states. Depending on the particular experimental set-up, different definitions of the *decay* photons are applied by the various collaborations: all groups subtract

the decays of π^0- and η-mesons, however, some groups also subtract the decays of the less abundant and short-living particles η', ω, ϕ, a_1 and the Δ-resonance. Indeed, the determination of the latter contributions (in particular from a_1 and Δ) by experimental methods is questionable, because of the photon emission during the multiple absorption and regeneration in the initial interaction phase. Therefore, a theoretical understanding of the *decay* photon contributions to the inclusive spectrum is important. Especially for analyzing simultaneously various measurements at different energies and within different experimental settings a theoretical analysis is mandatory which accounts for the different experimental acceptance cuts (from various collaborations) and allows for comparing spectra at different centralities and bombarding energies, ultimately bridging the gap from p-p to central heavy-ion collisions.

Within the PHSD we calculate the photon production from the following hadronic decays:

$$\pi^0 \to \gamma + \gamma, \quad \eta \to \gamma + \gamma, \quad \eta' \to \rho + \gamma, \quad \omega \to \pi^0 + \gamma, \quad \phi \to \eta + \gamma, \quad a_1 \to \pi + \gamma, \quad \Delta \to \gamma + N,$$

where the parent hadrons may be produced in baryon-baryon (BB), meson-baryon (mB) or meson-meson (mm) collisions in the course of the heavy-ion collision or may stem from hadronization. The decay probabilities are calculated according to the corresponding branching ratios taken from the latest compilation by the Particle Data Group [90]. The broad resonances – including the a_1, ρ, ω mesons – in the initial or final state are treated in PHSD in line with their (in-medium) spectral functions and the differential photon or dilepton yield is integrated in time (see below).

Let us briefly describe the evaluation of the photon production in the decays of the Δ-resonance as an important example. The $\Delta \to N\gamma$ width depends on the resonance mass M_Δ, which is distributed according to the Δ spectral function. Starting from the pioneering work of Jones and Scadron [91], a series of models [92, 93, 94] provided the mass-dependent electromagnetic decay width of the Δ-resonance in relation to the total width of the baryon. We employ the model of Ref. [93] in the present calculations where the spectral function of the Δ-resonance is assumed to be of relativistic Breit-Wigner form. Furthermore, we adopt the "Moniz" parametrization [95] for the shape of the Δ-spectral function, i.e. the dependence of the width on the mass $\Gamma^{tot}(M_\Delta)$.

The *direct photons* are obtained by subtraction of the decay-photon contributions from the inclusive (total) spectra measured experimentally. So far, the following contributions to the *direct* photons have been identified:

- The photons at large transverse momentum p_T, so called *prompt* or *pQCD* photons, are produced in the initial hard $N + N$ collisions and stem from jet fragmentation; these contributions are well described by perturbative QCD (pQCD). The latter, however, might be modified in $A + A$ contrary to $p + p$ reactions due to a modification of the parton distributions (initial state effect) or the parton energy loss in the medium (final state effect). In $A + A$ collisions at large p_T there may also arise contributions from the induced jet-γ-conversion in the QGP and the jet-medium photons from the scattering of hard partons with thermalized partons $q_{hard} + q(g)_{QGP} \to \gamma + q(g)$; however, these contributions are subleading. As noted above the prompt photons are well modeled by perturbative QCD calculations.

- After the subtraction of the *prompt* photons from the *direct* photon spectra, there is a significant remaining photon yield for $p_T < 3$ GeV, which is denoted as *thermal* photons. These low-p_T photons can be emitted by various partonic and hadronic sources as listed below:

  1. Photons that are radiated by quarks in the interaction with antiquarks and gluons,

     $$q + \bar{q} \to g + \gamma, \qquad\qquad q/\bar{q} + g \to q/\bar{q} + \gamma.$$

     In addition, photon production in the bremsstrahlung reactions $q+q/g \to q+q/g+\gamma$ is possible [96]. The implementation of the photon production by the quark and gluon interactions in the PHSD is based on the off-shell cross sections for the interaction of the massive dynamical quasi-particles as described in Ref. [97, 98]. The photon production rates in a thermal medium – calculated within the DQPM effective model for QCD – are within a factor of 2 similar to the rates obtained by the resummed pQCD approach from Ref. [99] (see Section 5.2). Since the quark-gluon-plasma produced in the heavy-ion collisions is strongly-interacting, the Landau-Migdal-Pomeranchuk (LPM) coherence effect can be important, too (cf. Section 5.3).

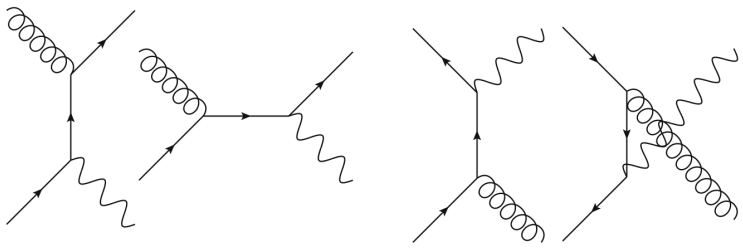


Figure 17: Feynman diagrams for the leading partonic sources of *thermal* photons ($q(\bar{q}) + g \to q(\bar{q}) + \gamma$ and $q + \bar{q} \to g + \gamma$) included in the PHSD calculations. The propagators and strong coupling are employed from the DQPM.

2. All colliding hadronic charges (meson, baryons) can also radiate photons by the bremsstrahlung processes:

$$m + m \to m + m + \gamma \qquad m + B \to m + B + \gamma.$$

These processes have been studied within the HSD/PHSD in Refs. [98, 100, 101, 102] in continuation of earlier work at lower energies [103, 104]. The implementation of photon bremsstrahlung from hadronic reactions in transport approaches has been based until recently in the 'soft photon' approximation (SPA). The soft-photon approximation [105, 106, 107] relies on the assumption that the radiation from internal lines is negligible and the strong interaction vertex is on-shell which is valid only at low energy (and p_T) of the produced photon. Since the relatively high transverse momenta of the *direct* photons ($p_T = 0.5 - 1.5$ GeV) are most important for a potential understanding of the "direct photon puzzle" we have departed from the SPA in the PHSD [102]. The PHSD results presented in this review have been obtained employing microscopic one-boson-exchange (OBE) calculations instead (cf. Section 5.4).

3. Additionally, the photons can be produced in binary meson+meson and meson+baryon collisions. We consider within the PHSD the *direct* photon production in the following $2 \to 2$ scattering processes:

$$\pi + \pi \to \rho + \gamma, \qquad \pi + \rho \to \pi + \gamma, \qquad V + N \to \gamma + N, \qquad \text{where } V = \rho,\ \phi,\ \omega, \text{ and } N = n, p,$$

accounting for all possible charge combinations (cf. Subsection 5.5). Further mesonic $2 \to 2$ reactions with the allowed quantum numbers for photon production, such as $\pi + \omega$, $\rho + \omega$, $V + \eta$ etc., can also contribute [108], but are discarded in the actual calculations that focus on the leading channels.

5.2. Photon production by dynamical quasiparticles in the QGP

We start with the description of photon production in the interactions of quarks and gluons in the quark-gluon plasma, which dominantly proceeds through the quark-antiquark annihilation and the gluon Compton scattering processes:

$$q + \bar{q} \to g + \gamma \qquad q(\bar{q}) + g \to q(\bar{q}) + \gamma,$$

that are diagrammatically presented in Fig. 17.

In the strongly interacting QGP the gluon and quark propagators (in PHSD) differ significantly from the non-interacting propagators such that bare production amplitudes can no longer be used [33, 42]. The off-shell quarks and gluons have finite masses and widths, which parametrize the resummed interaction of the QGP constituents. The perturbative QCD results for the cross sections of the processes in Fig. 17 have to be generalized in order to include the finite masses for fermions and gluons as well as their broad spectral functions. In Ref. [109], the influence of the gluon off-shellness (fixed to $m_g^2 = |\vec{k_g}|^2$) on the photon production was studied but the quark masses had been neglected and the spectral functions were assumed to be δ-functions (quasiparticle approximation). On the other hand, in Ref. [110] a finite quark mass has been incorporated in the elementary cross sections for both the quark annihilation and the gluon-Compton scattering processes (though the gluon was taken to be massless and the quasiparticle approximation maintained). However, the formulae from Ref. [110] still could not consistently describe the photon production by the effective dressed quarks and gluons within the PHSD transport approach, because they did not account for the finite width. Furthermore, in all the previous calculations the masses of quarks and antiquarks were assumed to be equal, which is not the case for the scattering of off-shell particles with continuous mass distributions.

The evaluation of the cross sections for *dilepton* production by off-shell partons, taking into account finite masses for quarks, antiquarks (with generally $m_q \neq m_{\bar{q}}$) and gluons m_g as well as their finite spectral width (by integrating over the mass distributions) has been carried out in Refs. [97, 111]. In order to obtain the cross sections for the *real* photon production, we use the relation between the real photon production cross section and the cross section for dilepton production [112]:

$$\frac{d\sigma(\gamma)}{dt} = \lim_{M\to 0} \frac{3\pi}{\alpha} \frac{M^2}{L(M)} \frac{d^2\sigma(e^+e^-)}{dM^2 dt}, \tag{108}$$

where M^2 is the invariant mass squared of the lepton pair (virtual photon), while the kinematical factor $L(M)$ is given by

$$L(M) = \sqrt{1 - \frac{4m_e^2}{M^2}}(1 + \frac{2m_e^2}{M^2}) \tag{109}$$

with m_e denoting the lepton mass. We employ the DQPM parametrization for the effective quark and gluon propagators in the calculation of $d^2\sigma(e^+e^-)/dM^2dt$ thus going beyond the leading twist approximation [113]. We refer the reader to Ref. [97] for details of the calculations and provide only the necessary steps here. We briefly summarize the differences of our 'effective' approach from the standard pQCD:

- We take into account full off-shell kinematics, i.e. the transverse motion and virtuality of the partons,
- quark and gluon lines in the diagrams in Fig. 17 and in the leading-order diagram $q + \bar{q} \to \gamma^*$ (which is relevant only for dilepton production) are dressed with non-perturbative spectral functions and self-energies: the cross sections are derived for arbitrary masses of all external parton lines and integrated over these virtualities weighted with spectral functions (see e.g. Refs [100, 111] for an introduction to the method); the internal lines are dressed with self energies.
- Strong vertices are modified compared to pQCD by replacing the perturbative coupling (that runs with the momentum transfer) with the running coupling $\alpha_S(T)$ that depends on the temperature T of the medium according to the parametrization of lattice data in Ref. [41], while the temperature T is related to the local energy density $\epsilon(\mathbf{r}; t)$ by the lQCD equation of state. Note that close to T_c the effective coupling $\alpha_S(T)$ increases with decreasing temperature much faster than the pQCD prediction.
- Due to the broad widths of quarks and gluons in the sQGP [42] – which is the consequence of their high interaction rate – there are non-vanishing contributions also from the decays of virtual quarks ($q \to q + g + l^+l^-$) and gluons ($g \to q + \bar{q} + l^+l^-$), which are forbidden kinematically in pQCD. However, we presently discard these processes in PHSD.

Due to the factorization [114], the dilepton emission from the QGP created in the heavy-ion collision is given by the convolution of the elementary subprocess cross sections (describing quark/gluon interactions with the emission of dileptons) with the structure functions that characterize the properties and evolution of the plasma (encoded in the distribution of the quarks and gluons with different momenta and virtualities):

$$\frac{d^3\sigma^{\rm QGP}}{dM^2 dx_F dq_T^2} = \sum_{abc} \int d\hat{s} \int_0^\infty dm_1^i \int_0^\infty dm_2^i \int_0^\infty d\mu^f \; F_{ab}(\hat{s}, m_1^i, m_2^i) \mathrm{A}_c(\mu^f) \frac{d^3\hat{\sigma}_{abc}(\hat{s}, m_1^i, m_2^i, \mu^f)}{dM^2 dx_F dq_T^2}, \tag{110}$$

where M^2 is the invariant mass of the dilepton pair, m_1^i and m_2^i are the masses of the incoming partons, μ^f is the mass of the outgoing parton, while the indices a, b, c denote quark, antiquark or gluon such that all the elementary reactions are covered. Here, $\mathrm{A}(\mu^f)$ is the spectral function for the parton in the final state. The structure function F_{ab} is a two-particle correlator that depends on the invariant energy $\sqrt{\hat{s}}$ of the partonic subprocess as well as on the virtualities of the incoming partons. Since we work in a 2PI-like approximation, the partons in the sQGP are characterized by single-particle distributions and we assume that the plasma structure function is given by

$$F_{ab}(\hat{s}, m_1, m_2) = A_a(m_1) A_b(m_2) \frac{dN_{ab}}{ds}. \tag{111}$$

In this context, the quantity $dN_{q\bar{q}}/ds$ has the meaning of the differential multiplicity of $q + \bar{q}$ collisions in the plasma as a function of the invariant energy squared s of these collisions in the interval ds. Analogously, dN_{gq}/ds denotes the differential multiplicity of $g + q$ collisions.

The off-shell partonic cross sections $\hat{\sigma}_{abc}(\hat{s}, m^{i1}, m^{i2}, \mu^f)$ for the different processes have been derived in Ref. [97]. We sketch the derivation for the example of the Gluon-Compton scattering diagram: We start from the formula for the unpolarized cross section,

$$d\sigma = \frac{\Sigma|\bar{M_{i\to f}}|^2 \varepsilon_1 \varepsilon_2 \Pi \frac{d^3 p_f}{(2\pi)^3}}{\sqrt{(p_1 p_2)^2 - m_1^2 m_2^2}} \; (2\pi)^4 \delta(p_1 + p_2 - \Sigma p_f), \tag{112}$$

where the incoming quark and antiquark momenta are p_1 and p_2 and their masses m_1 and m_2, respectively. In Eq. (112) p_f are the momenta of the outgoing particles, i.e. of the electron (muon) and positron (anti-muon) and gluon. We define the momenta of the internal quark – exchanged in the two relevant diagrams (see Fig. 17) – by $p_3 \equiv p_1 - q$, $\bar{p}_3 \equiv p_1 - p_2 - p_3$ and its mass by m_3. The final gluon momentum is denoted by k and its mass by μ. Then the matrix element of the process $q + \bar{q} \to g + \gamma^*$ is given by

$$M_{i\to f} = M_a + M_b, \tag{113}$$

where

$$\begin{aligned} M_a &= -e_q e g_s T^l_{ij} \frac{\epsilon_\nu(q)\epsilon_{\sigma l}(k)}{p_3^2 - m_3^2} u_i(p_1, m_1) \left[\gamma^\nu (\hat{p}_3 + m_3)\gamma^\sigma\right] v_j(p_2, m_2), \\ M_b &= -e_q e g_s T^l_{ij} \frac{\epsilon_{\sigma l}(k)\epsilon_\nu(q)}{\bar{p_3}^2 - m_3^2} u_i(p_1, m_1) \left[\gamma^\eta (\hat{\bar{p}_3} + m_3)\gamma^\nu\right] v_j(p_2, m_2). \end{aligned} \tag{114}$$

In Eq. (114) e is the electron charge, e_q is the quark fractional charge while T^l_{ij} is the generator of the SU(3) color group (that gives the color factor in the cross section). Furthermore, $\epsilon_\nu(q)$ is the polarization vector for the virtual photon with momentum q, $\epsilon_{\sigma l}(k)$ is the polarization vector for the gluon of momentum k and color l; $u_i(p, m)$ is a Dirac spinor for the quark with momentum p, mass m and color i and $v_i(p, m)$ is the spinor for the anti-quark.

The squared matrix element – summed over all spin polarizations as well as over the color degrees-of-freedom – can be decomposed in the following sums:

$$\sum |M|^2 = \sum M_a^* M_a + \sum M_b^* M_b + \sum M_a^* M_b + \sum M_b^* M_b, \tag{115}$$

where the star denotes complex conjugation. The spinors for quark states with mass m_i contribute to the expression for the average matrix element only in the combinations $\sum \bar{u}(p, m_i)u(p, m_i) = (\hat{p} + m_i)$ and the correlation functions between the states with different masses do not enter $|M|^2$. Thus we find:

$$\begin{aligned} \sum M_a^* M_b \;=\; & -\frac{e_q^2 e^2 g_s^2 \mathrm{Tr}\{T^2\}}{(p_3^2 - m_3^2)(\bar{p_3}^2 - m_3^2)} \Big[\mathrm{Tr}\left\{(\hat{p_2} - m_2)\gamma_\sigma(\hat{p_3} + m_3)\gamma_\nu(\hat{p_1} + m_1)\gamma^\sigma(\hat{\bar{p}_3} + m_3)\gamma^\nu\right\} \\ & - \frac{1}{M^2}\mathrm{Tr}\left\{(\hat{p_2} - m_2)\gamma_\sigma(\hat{p_3} + m_3)\hat{q}(\hat{p_1} + m_1)\gamma^\sigma(\hat{\bar{p}_3} + m_3)\hat{q}\right\} \\ & - \frac{A}{k^2}\mathrm{Tr}\left\{(\hat{p_2} - m_2)\hat{k}(\hat{p_3} + m_3)\gamma_\nu(\hat{p_1} + m_1)\hat{k}(\hat{\bar{p}_3} + m_3)\gamma^\nu\right\} \\ & + \frac{A}{k^2 M^2}\mathrm{Tr}\left\{(\hat{p_2} - m_2)\hat{k}(\hat{p_3} + m_3)\hat{q}(\hat{p_1} + m_1)\hat{k}(\hat{\bar{p}_3} + m_3)\hat{q}\right\}\Big] \end{aligned} \tag{116}$$

$$\begin{aligned} \sum |M_a|^2 \;=\; & -\frac{e_q^2 e^2 g_s^2 \mathrm{Tr}\{T^2\}}{(p_3^2 - m_3^2)^2} \left[\mathrm{Tr}\left\{\gamma_\sigma(\hat{p_3} + m_3)\gamma_\nu(\hat{p_1} + m_1)\gamma^\nu(\hat{p_3} + m_3)\gamma^\sigma(\hat{p_2} - m_2)\right\}\right. \\ & - \frac{1}{M^2}\mathrm{Tr}\left\{\gamma_\sigma(\hat{p_3} + m_3)\hat{q}(\hat{p_1} + m_1)\hat{q}(\hat{p_3} + m_3)\gamma^\sigma(\hat{p_2} - m_2)\right\} \\ & - \frac{A}{k^2}\mathrm{Tr}\left\{\hat{k}(\hat{p_3} + m_3)\gamma_\nu(\hat{p_1} + m_1)\gamma^\nu(\hat{p_3} + m_3)\hat{k}(\hat{p_2} - m_2)\right\} \\ & \left. + \frac{A}{k^2 M^2}\mathrm{Tr}\left\{\hat{k}(\hat{p_3} + m_3)\hat{q}(\hat{p_1} + m_1)\hat{q}(\hat{p_3} + m_3)\hat{k}(\hat{p_2} - m_2)\right\}\right]. \end{aligned} \tag{117}$$

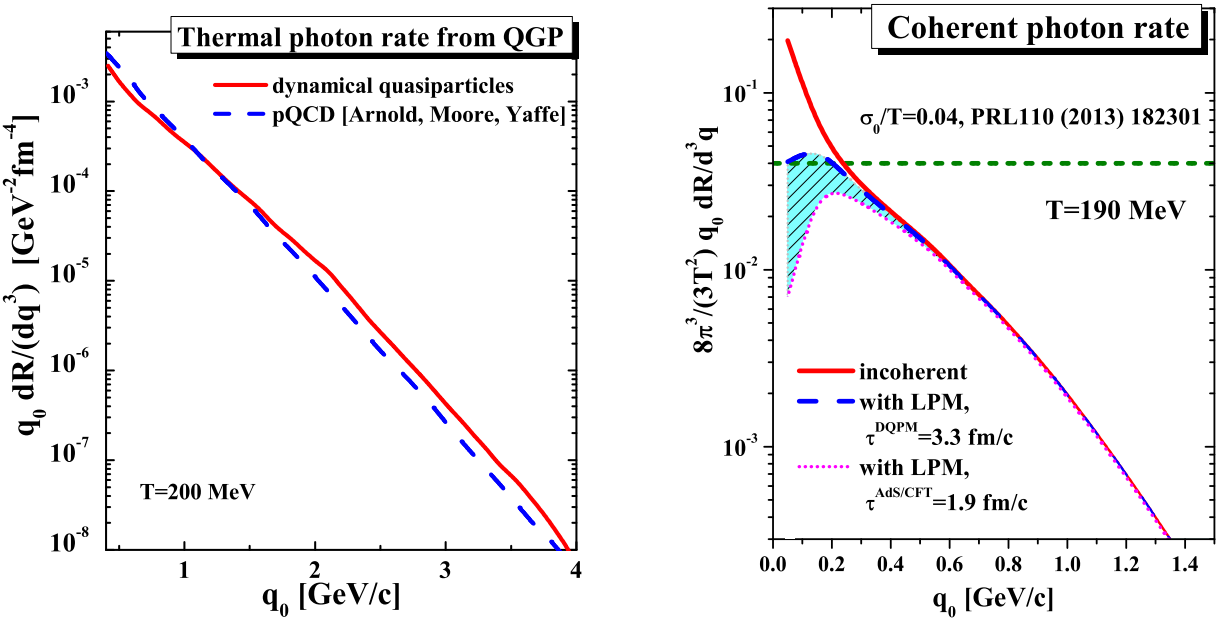


Figure 18: (l.h.s.) Invariant rate of photons produced from the strongly-interacting quark-gluon plasma (at temperature T= 200 MeV) consisting of massive broad quasi-particle quarks and gluons (red solid line). The leading-order pQCD rate (blue dashed line) from Ref. [99] (AMY-rate) is shown for comparison. (r.h.s.) Incoherent invariant photon production rate from the strongly-interacting quark-gluon plasma (at temperature T= 190 MeV) consisting of massive broad quasi-particle quarks and gluons (red solid line) scaled by $8\pi^3/(3T^2)$ in order to match the electric conductivity for $q_0 \to 0$ (cf. (122)). The blue dashed line and the magenta dotted line show the coherent rates for two assumptions on the average time between the collisions τ, i.e. from the DQPM model (upper, dashed line) and from the AdS/CFT correspondence as a lower limit (dotted line). The figures are taken from Ref. [102].

Note that by the transformation $\{p_3 \to \bar{p_3}, p_1 \to p_2, p_2 \to p_1, m_1 \to -m_2, m_2 \to -m_1\}$ we readily obtain $\sum M_b^* M_a$ from $\sum M_a^* M_b$ and $\sum |M_b|^2$ from $\sum |M_a|^2$. In equations (116) and (117) the factor A sets the gauge. For instance, in the generalized renormalizable gauge we have $A = (1-\lambda)k^2/(k^2 - \lambda\mu^2)$ and specifically in Feynman gauge $\lambda = 0$. We used the feynpar.m [115] package of the Mathematica program [116] to evaluate the traces of the products of the gamma matrices. The resulting cross sections are given in Ref. [97]. Since the final formulae for the cross sections are quite lengthy, we do not repeat them here. But we note that it is seen from the explicit results that the quark off-shellness leads to higher twist corrections ($\sim m_q^2/s, m_q^2/t, m_q^2/u$). These corrections are small in hard hadron scattering at high center-of-mass energy $\sqrt{s} > 10$ GeV but become substantial for photon production in the sQGP, where the characteristic $\sqrt{s}$ of parton collisions is of the order of a few GeV.

We take $d^2\sigma(e^+e^-)/dM^2dt$ from Ref. [97] and use relation (108) to implement the real photon production in the off-shell quark and gluon interactions into the PHSD transport approach. In each interaction of $q + \bar{q}$ or $q/\bar{q} + g$ the photon production probability and the elliptic flow of the produced photon are recorded differentially in transverse momentum p_T, rapidity y and interaction time t.

5.3. Thermal rates and the Landau-Migdal-Pomeranchuk effect

Using the cross sections for photon radiation by dressed quarks and gluons in the processes $q\bar{q} \to g\gamma$ and $qg \to q\gamma$ from Ref. [97] we can calculate the differential rate of photons from a thermalized strongly interacting QGP. Fig. 18 presents the invariant rate of photons produced from a QGP at the temperature $T = 200$ MeV (red solid line) in comparison to the leading-order Log-resummed perturbative QCD rate (blue solid line) from Arnold, Moore and Yaffe (AMY rate, taken from Ref. [99]). One observes a qualitative agreement between the results of both approaches although the degrees-of-freedom and their couplings are different. We mention that photon rates calculated recently at the NLO in perturbative QCD [117, 118, 119] also are approximately in line with those presented in Fig. 18 (l.h.s.).

The radiation of photons by charged particles is modified in the medium compared to the vacuum. One of such medium effects is caused by the absence of well-defined incoming and outgoing asymptotic states due to

the multiple scattering of particles in a strongly interacting environment. If the subsequent scatterings occur within the time necessary for photon radiation $\tau_\gamma \sim 1/q_0$, then the amplitudes for the emission of photons before and after the charged particle scattering have to be summed coherently. The effect of this destructive interference on the photon spectrum by electrons transversing a dense medium was first studied by Landau and Pomeranchuk in Ref. [120, 121] and Migdal in Ref. [122]. Accordingly, the Landau-Pomeranchuk-Migdal (LPM) effect modifies the spectrum of photons produced in the medium in comparison to the incoherent sum of emissions in quasi-free scatterings, leading especially to a suppression of the low energy photons because the formation time of the photon τ_γ is proportional to the inverse photon energy $1/q_0$. In particular, the LPM effect regularizes the $1/q_0$ divergence of the quasi-free bremsstrahlung spectra. The LPM suppression and the induced thermal mass of the medium quanta (the dielectric effect) together ensure that the photon spectrum is finite in the limit $q_0 \to 0$.

The importance of the LPM effect for the case of dilepton and photon production from QCD systems was shown in Refs. [123, 124, 125, 126] long ago. The magnitude of the LPM suppression is governed by the average time between the collisions τ, which in turn is given by the inverse scattering length a or by the inverse average spectral width of the particles γ:

$$\tau = \frac{1}{a} \sim \frac{1}{\gamma}. \tag{118}$$

The LPM suppression is more pronounced in case of small τ, i.e. for high reaction rates γ. Thus we expect it to be important for the emission of photons from the strongly-interacting quark-gluon plasma (sQGP) as created in the early phase of the heavy-ion collision. Indeed, it was shown in Refs. [32, 61] in the scope of the DQPM that the average collision time of partons is as short as $\tau \approx 2-3$ fm/c for temperatures in the range $T = 1$–$2\ T_c$, where $T_c \approx 158$ MeV is the deconfinement transition temperature. In comparison, the average time between pion collisions in a thermalized pion gas at temperatures $T < T_c$ is above 10 fm/c [123, 124].

Let us now quantify the magnitude of the LPM effect on the spectrum of photons radiated from the QGP as calculated within the PHSD. The coherent photon production rate - taking into account the LPM effect - differs from the incoherent cross section by a suppression factor, which generally depends on the photon energy, temperature and the interaction strength of the constituents. The coherent photon emission rate has been derived in Ref. [123, 124] for an elastically interacting pion gas in the soft photon approximation for the photon radiation amplitudes. The authors of Ref. [123, 124] used the same method for the calculation of the photon emission over the whole trajectory of the charged particle as adopted in the original work by Migdal in Ref. [122]. After averaging over the times between collisions τ, assuming an exponential distribution,

$$\frac{dW}{d\tau} = a e^{-\tau a}, \tag{119}$$

the coherent photon emission rate was found to be

$$\frac{dR}{dq^3} = N \frac{2\alpha_{_{EM}}}{(2\pi)^2} \left\langle v^2 \frac{(1-\cos^2\Theta)}{a^2 + q_0^2(1 - v\cos\Theta)^2} \right\rangle, \tag{120}$$

where the brackets $< . >$ stand for an average over the velocities of the scattering particles after the scattering. In Eq. (120) the velocities are characterized by their absolute values v and scattering angles $\cos\Theta$ in the center-of-mass frame with respect to the incoming (pion) momenta, while N is the number of scatterings and $\alpha_{EM} \approx 1/137$. A realistic parametrization of the data was used for the pion elastic scattering cross section (cf. Section 5.4) but the scattering was assumed to be isotropic. We recall that the incoherent rate is obtained from Eq. (120) in the limit $a = 0$.

An analytical form of the coherence factor was obtained in Ref. [126] in the model of hard scattering centers, using a quantum mechanical approach to coherently sum the photon amplitudes from all the scatterings. In the thermal medium the spacial distribution of the scattering centers is assumed random. Consequently, the function (119) naturally arises in this model for the distribution of times between collisions by a direct calculation of the two-particle correlation function. The quenching factor in the dipole limit ($\vec{q} = 0$) was found to be

$$(G(q_0\tau))^2 = \left(\frac{(q_0\tau)^2}{1 + (q_0\tau)^2} \right)^2. \tag{121}$$

Although formula (121) was obtained in a simple model, it is useful because it correctly captures the dependence of the LPM suppression on the average strength of the interaction given solely by the mean-free-time between collisions τ in the assumption of isotropic collisions.

We recall that the perturbative interaction of quarks and gluons is dominated by small angle scattering due to the massless particle exchange in the t-channel diagrams. In this case the coherence factor for the quark system in the limit of small scattering angles was obtained in Ref. [125]. However, the elastic scattering of dressed quarks in the PHSD is not dominated by the $t \to 0$ pole as in the perturbative case since the gluon mass (of order 1 GeV) acts as a regulator in the amplitude. Accordingly, the angular distribution for quark-quark scattering is closer to an isotropic distribution for low or moderate $\sqrt{s}$ in accordance with the model assumptions of Ref. [126] such that the expression (121) should apply as an estimate of the LPM suppression for the photon emission within the PHSD.

In Fig. 18 (r.h.s.) we show the photon emission rate in a QGP at the temperature T=190 MeV as calculated in the PHSD as an incoherent sum of the photon emission in quark and gluon scatterings (red solid line) which diverges for $q_0 \to 0$. The blue dashed line gives the same rate with the quenching factor (121) applied using $\tau(T) = 1/\Gamma(T) \approx 3.3$ fm/c from the DQPM (for T= 190 MeV). We observe that the suppression – in comparison to the incoherent rate – is visible only for photon energies $q_0 < 0.4$ GeV. For an estimate of the upper limit on the LPM suppression we employ the relaxation time approximation for the ratio of the shear viscosity over entropy density η/s which gives $\eta/s \approx$0.14 at T=190 MeV in the DQPM [55, 60]. The lowest bound as conjectured within the AdS/CFT correspondence is $\eta/s = 1/(4\pi) \approx 0.08$. In the relaxation time approximation this corresponds to a lower value of $\tau \approx 1.9$ fm/c. The coherent photon rate in this case is given by the (lowest) magenta dotted line and even shows a peak in the photon rate for $q_0 \approx 0.2$ GeV.

In order to further clarify the strength of the LPM suppression of the photon emission in the sQGP, we use the knowledge of the electric conductivity $\sigma_0(T)$ of the sQGP from the DQPM [61] which is roughly in line with more recent results from lattice QCD (cf. Fig. 6, r.h.s.). We recall that the photon emission rate from a thermal medium is controlled by σ_0 via the relation [127],

$$\frac{\sigma_0}{T} = \frac{8\pi^3}{3T^2} \lim_{q_0 \to 0} \left(q_0 \frac{dR}{d^3q} \right), \tag{122}$$

where T is the temperature of the system, q_0 is the photon energy and $\vec{q}$ is the photon momentum. Using the number for σ_0/T from the PHSD at the temperature of T = 190 MeV from Ref. [61] (or Fig. 6, r.h.s.), we obtain a limiting value for the scaled photon emission rate of 0.04 for $q_0 \to 0$ according to formula (122) (green short dashed line in Fig. 18, r.h.s.). The blue dashed line in Fig. 18 – the estimate of the rate based on formula (121) and the DQPM average spectral width of the quarks/antiquarks – indeed approaches the limiting value of 0.04 as given by the kinetic calculations of the electric conductivity.

Taking into account some uncertainty in the determination of τ and the expression (121), we conclude from Fig. 18 (r.h.s.) and analogous calculations at different temperatures that the LPM effect influences the photon production from the QGP for photon energies below $q_0 \approx 0.4$ GeV, but is negligible for higher photon energies. We note in passing that the suppression of the photon spectrum in the hadronic phase is much smaller due to the lower interaction rate, i.e. a longer interaction time τ and thus a lower LPM suppression factor at the same photon energy.

5.4. Bremsstrahlung $m + m \to m + m + \gamma$ beyond the soft-photon approximation

We briefly sketch the description of the photon bremsstrahlung in meson+meson scattering beyond the soft-photon approximation [128]. Since pions are the dominant meson species in the heavy-ion collisions [98], we concentrate here on the description of the bremsstrahlung photon production in pion+pion collisions. In order to calculate the differential cross sections for the photon production in the processes of the type $\pi+\pi \to \pi+\pi+\gamma$ we use the one-boson exchange (OBE) model as originally applied in Ref. [129] to the dilepton bremsstrahlung in pion+pion collisions, later on in Ref. [130] to the low-energy photon bremsstrahlung in pion+pion and kaon+kaon collisions. The calculations are based on a covariant microscopic effective theory with the interaction Lagrangian,

$$L_{int} = g_\sigma \sigma \partial_\mu \vec{\pi} \partial^\mu \vec{\pi} + g_\rho \vec{\rho}^\mu \cdot (\vec{\pi} \times \partial_\mu \vec{\pi}) + g_f f_{\mu\nu} \partial^\mu \vec{\pi} \cdot \partial^\nu \vec{\pi}, \tag{123}$$

as suggested in Refs. [96, 129]. Within this model the interaction of pions is described by the exchange of scalar, vector and tensor resonances: σ, ρ and $f_2(1270)$, respectively. Additionally, form factors are incorporated in the vertices in the t- and u-channels to account for the composite structure of the mesons and thus to effectively suppress the high momentum transfers,

$$h_\alpha(k^2) = \frac{m_\alpha^2 - m_\pi^2}{m_\alpha^2 - k^2}, \tag{124}$$

where $m_\alpha = m_\sigma$ or m_ρ or m_f is the mass of the exchanged meson and k^2 is the momentum transfer squared.

The cross section for elastic $\pi + \pi \to \pi + \pi$ scattering is given by

$$\frac{d\sigma_{el}(s)}{dt} = \frac{|M_{el}|^2}{16\pi s(s-4m_\pi^2)}, \tag{125}$$

where the matrix element $|M|^2$ is calculated by coherently summing up the Born diagrams of the σ-, ρ- and f_2-meson exchange in t, s and u channels (the u-channel diagrams are needed only in case of identical pions),

$$|M_{el}|^2 = |M^s(\sigma)+M^t(\sigma)+M^u(\sigma)+M^s(\rho)+M^t(\rho)+M^u(\rho)+M^s(f)+M^t(f)+M^u(f)|^2. \tag{126}$$

Let us define the four-momenta of the incoming pions as $p_a = (E_a, \vec{p}_a)$ and $p_b = (E_b, \vec{p}_b)$, the momenta of the outgoing pions as $p_1 = (E_1, \vec{p}_1)$ and $p_2 = (E_2, \vec{p}_2)$ and the four-momentum of the exchanged resonance (σ, ρ or f_2) as k. The propagators of the massive and broad scalar and vector particles are used to describe the exchange of the σ and ρ mesons (see e.g. Ref. [129]). The resonance f_2 is a spin-2 particle, for which the full momentum-dependent propagator has been derived in Ref. [131]. The polarization sum is

$$\begin{aligned} P_{\mu\nu\alpha\beta} &= \frac{1}{2}(g_{\mu\alpha}g_{\nu\beta} + g_{\mu\beta}g_{\nu\alpha} - g_{\mu\nu}g_{\alpha\beta})\frac{1}{2}(g_{\mu\alpha}\frac{k_\nu k_\beta}{m_f^2} + g_{\mu\beta}\frac{k_\nu k_\alpha}{m_f^2} + g_{\nu\alpha}\frac{k_\mu k_\beta}{m_f^2} + g_{\nu\beta}\frac{k_\mu k_\alpha}{m_f^2}) \\ &+\frac{2}{3}(\frac{1}{2}g_{\mu\nu} + \frac{k_\mu k_\nu}{m_f^2})(\frac{1}{2}g_{\alpha\beta} + \frac{k_\alpha k_\beta}{m_f^2}). \end{aligned} \tag{127}$$

Following the example of the dilepton production study in Ref. [129], we use the same propagator for the f_2 resonance while additionally accounting for its finite width by adding an imaginary part to the self-energy in accordance with its lifetime.

As a result, the following expressions are obtained for the matrix elements in case of elastic $\pi + \pi$ scattering diagrams (we give here explicitly the t- and s-channel results, the u-channels can be easily obtained by the crossing relations):

$$\begin{aligned} M^t(\sigma) &= \frac{-g_\sigma^2 h_\sigma^2(t)\left(2m_\pi^2 - t\right)^2}{t - m_\sigma^2 + im_\sigma\Gamma_\sigma}, \qquad M^s(\sigma) = \frac{-g_\sigma^2\left(s - 2m_\pi^2\right)^2}{s - m_\sigma^2 + im_\sigma\Gamma_\sigma}, \\ M^t(\rho) &= \frac{-g_\rho^2 h_\rho^2(t)\left(s-u\right)^2}{t - m_\rho^2 + im_\rho\Gamma_\rho}, \qquad M^s(\rho) = \frac{g_\rho^2\left(u-t\right)^2}{s - m_\rho^2 + im_\rho\Gamma_\rho}, \\ M^t(f) &= \frac{g_f^2 h_f^2(t)}{t - m_f^2 + im_f\Gamma_f}\frac{1}{2}\left(\frac{2}{3}(2m_\pi^2 - t)^2 - (s - 2m_\pi^2)^2 - (2m\pi^2 - u)^2\right), \\ M^s(f) &= \frac{g_f^2}{s - m_f^2 + im_f\Gamma_f}\frac{1}{2}\left(\frac{2}{3}(s - 2m_\pi^2)^2 - (2m_\pi^2 - t)^2 - (2m\pi^2 - u)^2\right), \end{aligned} \tag{128}$$

where the Mandelstamm variables are defined as $s = (p_a + p_b)^2 = (p_1 + p_b)^2$, $t = (p_a - p_1)^2 = (p_b - p_2)^2$, $u = (p_a - p_2)^2 = (p_b - p_1)^2$. We point out that the formulae (128) are compact, because the masses of all pions were assumed to be equal to m_π and the energy-momentum conservation $p_a + p_b = p_1 + p_2$ has been used. These conditions are not satisfied for the off-shell $\pi + \pi \to \pi + \pi$ subprocess, which we encounter in the subsequent calculation of the bremsstrahlung photon production $\pi + \pi \to \pi + \pi + \gamma$. For the actual calculation we obtained the off-shell generalizations $M(p_a, p_b, p_1, p_2)$ of the formulae (128), which are too lengthy to be presented here explicitly.

A reduced version of the model with the exchange of only two resonances – the scalar σ and the vector ρ meson – was used by the authors of Ref. [130] to calculate the rate of the photon production from the $\pi + \pi \to \pi + \pi + \gamma$ process at low transverse momenta of the photons ($p_T < 0.4$ GeV). This approximation is suitable at low p_T because the photon rate in this kinematical region is dominated by pion collisions of low center-of-mass energy $\sqrt{s}$, for which the contribution of the f_2-exchange is small. However, relatively high transverse momenta of photons $p_T = 1 - 2$ GeV are of interest for our goal of clarifying the "puzzling" high elliptic flow of *direct* photons. Therefore, we use the OBE model with three mesons as interaction carriers (including the tensor particle $f_2(1270)$) in the PHSD calculations.

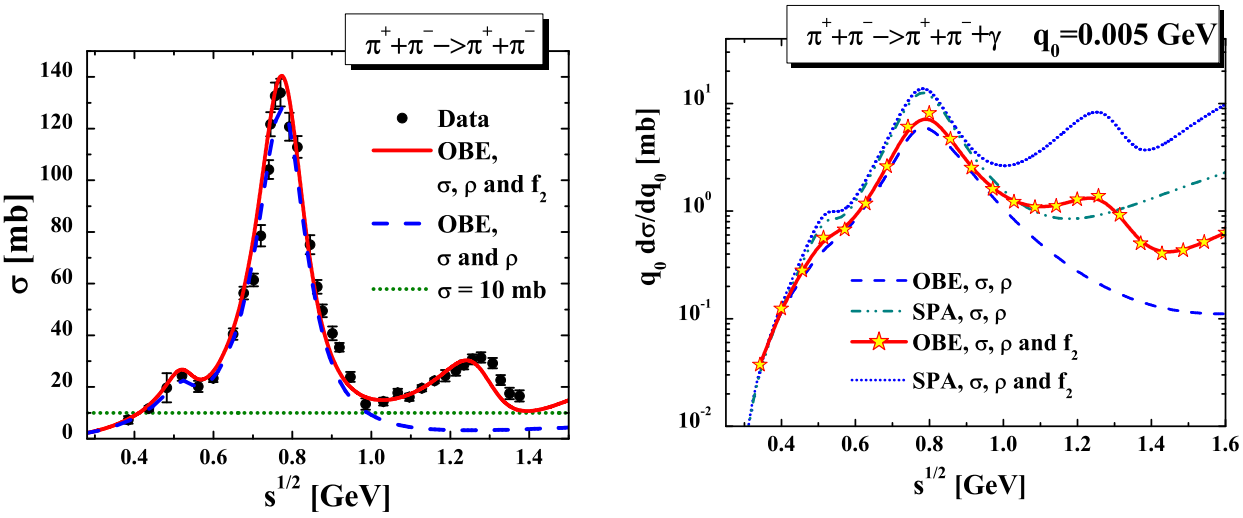


Figure 19: (l.h.s.) Cross section for pion+pion elastic scattering within the OBE effective models in comparison to the experimental data from Refs. [132, 133]: the exchange of two mesonic resonances, scalar σ and vector ρ (blue dashed line), and the exchange of three resonances σ, ρ and the tensor resonance $f_2(1270)$ of the particle data booklet [90] (red solid line). The green dashed line shows the constant and isotropic $\sigma_{el} = 10$ mb for orientation. (r.h.s.) Cross section for the production of a photon with energy $q_0 = 0.005$ GeV in the process $\pi + \pi - > \pi + \pi + \gamma$ within the following models: the exact OBE cross section within the effective model taking into account scalar, vector and tensor interactions via the exchange of σ, ρ and $f_2(1270)$-mesons (red line with star symbols), the soft photon approximation to this model (blue dotted line); the OBE result within the model taking into account only the scalar and vector interactions via the exchange of σ and ρ mesons (blue dashed line), and the soft photon approximation to this model (cyan dash-dot-dotted line). The figures are taken from Ref. [102].

Phenomenological coupling constants, masses and widths of the three interaction-carriers – entering the Lagrangian (123) – have to be fixed to the integrated energy-dependent cross section for pion+pion elastic scattering $\sigma_{el}(\sqrt{s})$, which is known experimentally as a function of $\sqrt{s}$). We present in Fig. 19 (l.h.s.) the integrated cross section for $\pi + \pi$ elastic scattering in two versions of the OBE model described above: taking into account the 2 resonances σ, ρ (dashed blue line) and taking into account the 3 resonances σ, ρ and f_2 (solid red line). Fitting the parameters of both variants of the OBE model (with two- or three-resonance exchange) to the data from Refs. [132, 133] we find the best-fit parameters: $g_\sigma m_\sigma = 2.0$, $m_\sigma = 0.525$ GeV, $\Gamma_\sigma = 0.100$ GeV, $g_\rho = 6.15$, $m_\rho = 0.775$ GeV, $\Gamma_\rho = 0.15$ GeV, $g_f m_f = 8.0$, $m_f = 1.274$ GeV, $\Gamma_f = 0.18$ GeV. The values of the masses and widths suggest an identification of the ρ-resonance to the ρ-meson and of the particle f_2 to the $f_2(1270)$ in the particle data book [90]. One sees in Fig. 19 (l.h.s.) that the tensor particle f_2 is important for the description of the pion interaction at higher collision energies $\sqrt{s} > 1$ GeV. Neglecting the contribution of the f_2 leads to an underestimation of the $\pi + \pi$ elastic scattering cross section by an order of magnitude around $\sqrt{s} = 1.2 - 1.3$ GeV. Later data on the $\pi + \pi$ interaction at $\sqrt{s}$ above 1 GeV – extracted in Ref. [134] from the measurement of the $K + p \to \Lambda + \pi + \pi$ reaction – also point to the importance of the tensor interaction in the resonance region of the $f_2(1270)$.

Within the OBE model for the covariant interactions of pions (described above), we can also calculate the emission of photons from the colliding pions by gauge coupling to the external hadron lines. The Feynman diagrams for the photon production in the process $\pi + \pi \to \pi + \pi + \gamma$ are shown in Fig. 20. For identical pions, e.g. $\pi^+ + \pi^+$, the u-channel diagrams have to be added, which are obtained from the t-channel diagrams by exchanging the outgoing pions. The applicability of this method is not limited to low photon energies but is restricted only by the applicability of the effective model to the description of the pion-pion (elastic) scattering.

Let us again denote the four-momenta of the incoming pions by p_a and p_b, the momenta of the outgoing pions by p_1 and p_2, and the photon momentum by $q = (q_0, \vec{q})$. The cross section for photon production in the process

$$\pi(p_a) + \pi(p_b) \to \pi(p_1) + \pi(p_2) + \gamma(q) \tag{129}$$

then is given by

$$d\sigma^\gamma = \frac{1}{2\sqrt{s(s - 4m_\pi^2)}} |M(\gamma)|^2 dR_3, \tag{130}$$

where dR_3 is the three-particle phase space, which depends on the momenta of the outgoing pions and of the photon,

$$dR_3 = \frac{d^3p_1}{(2\pi)^3 2E_1}\frac{d^3p_2}{(2\pi)^3 2E_2}\frac{d^3q}{(2\pi)^3 2q_0}(2\pi)^4\delta^4\left(p_a+p_b-p_1-p_2-q\right). \quad (131)$$

The cross section (130) will be integrated over the final pion momenta to obtain the differential photon spectrum $d\sigma/d^3q$. The δ-function allows to perform four integrations analytically and the remaining two are done numerically.

The matrix element M in (130) is a coherent sum of the diagrams presented in Fig. 20 – i.e. of the photon attached to each pion line π_a, π_b, π_1 and π_2 – and of contact terms, which account for the emission from the vertices and the internal lines:

$$|M(\gamma)|^2 = M^*_\mu(\gamma)M^\mu(\gamma) = |M^\mu_a + M^\mu_b + M^\mu_1 + M^\mu_2 + M^\mu_c|^2. \quad (132)$$

The complex matrix elements for the photon emission from each of the pion lines M^μ_i are calculated as sums of the three meson exchanges (σ, ρ, f_2). For instance:

$$M^\mu_1 = eJ^\mu_1\left[M^s_{el}(p_a,p_b,p_1+q,p_2) + M^t_{el}(p_a,p_b,p_1+q,p_2) + M^u_{el}(p_a,p_b,p_1+q,p_2)\right] \quad (133)$$

with

$$J^\mu_{a,b} = -Q_{a,b}\frac{(2p_{a,b}-q)^\mu}{2p_{a,b}\cdot q}, \qquad J^\mu_{1,2} = Q_{1,2}\frac{(2p_{1,2}-q)^\mu}{2p_{1,2}\cdot q}, \quad (134)$$

where Q_i are the charges of the pions in terms of the electron charge e. The matrix elements for the pion elastic subprocess $M_{el}(p_a,p_b,p_1+q,p_2)$ are the off-shell generalizations of the formulae (128).

The contact term M^μ_c is taken from Ref. [130], Eq. (14), where it was derived by demanding the gauge invariance of the resulting cross section. Indeed, the gauge invariance of the result has to be restored [135] in calculations within effective models. In the present work, we have used the contact terms in order to cancel the gauge-dependent parts in the matrix element as in Ref. [130]. Alternatively, one can take into account additional diagrams with the emission of photons from the internal lines (see Refs [129]) but this method does not always eliminate the need for contact terms (see Ref. [135]). We have verified that $q_\mu M^\mu(\gamma) = 0$ in our calculations and thus the resulting cross sections are gauge invariant.

The soft photon approximation is based on the first-order expansion in the Low theorem [128] and is valid at low photon energy and low $\sqrt{s_{mm}}$ of the meson+meson collision, as has been studied in detail for the production of dileptons in Ref. [129]. In this case the strong interaction part and the electromagnetic part can be separated, i.e. the soft-photon cross section for the reaction $m_1+m_2 \to m_1+m_2+\gamma$ can be written as

$$q_0\frac{d\sigma^\gamma(s)}{d^3q} = \frac{\alpha_{_{EM}}}{4\pi^2}\int\limits_{-\lambda(s,m_a^2,m_b^2)/s}^{0}|\epsilon\cdot J(q,t)|^2\frac{d\sigma_{el}(s)}{dt}dt, \quad (135)$$

where $\alpha_{_{EM}}$ is the fine structure constant, t is the momentum transfer squared in the $\pi+\pi\to\pi+\pi$ subprocess and ϵ is the photon polarization. In (135) J^μ is the electromagnetic current

$$J^\mu = -Q_a\frac{p^\mu_a}{(p_a\cdot q)} - Q_b\frac{p^\mu_b}{(p_b\cdot q)} + Q_1\frac{p^\mu_1}{(p_1\cdot q)} + Q_2\frac{p^\mu_2}{(p_2\cdot q)}.$$

The polarization sum

$$|\epsilon\cdot J|^2 = \left\{\sum_{pol\ \lambda} J\cdot\epsilon_\lambda J\cdot\epsilon_\lambda\right\} \quad (136)$$

depends on the photon momentum q, the charges of the pions Q_i as well as on the invariant kinematic variables,

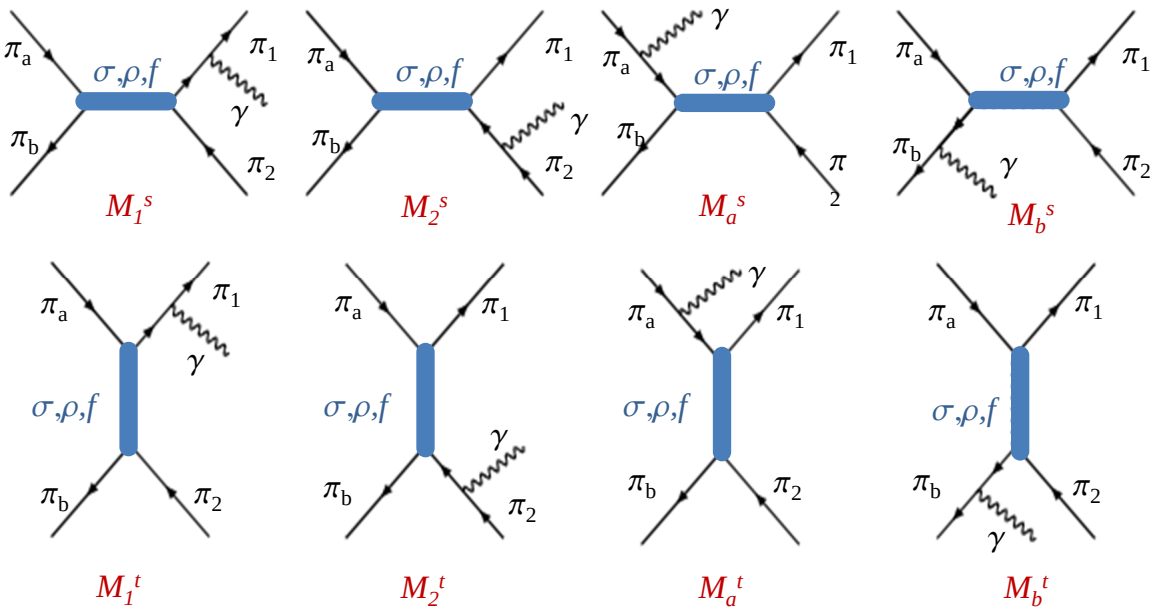


Figure 20: Feynman diagrams for photon production in the reaction $\pi+\pi\to\pi+\pi+\gamma$ in the one-boson exchange (OBE) model. The time goes from left to right. For identical pions, e.g. $\pi^+ + \pi^+$, the u-channel diagrams have to be added.

including t. For the case of equal-mass particle scattering ($m_a = m_b = m_1 = m_2 = m_\pi$) one obtains [96]:

$$
\begin{aligned}
|\epsilon\cdot J|^2 \;=\; & \frac{1}{q_0^2}\left\{ -(Q_a^2+Q_b^2+Q_1^2+Q_2^2) - 2(Q_aQ_b+Q_1Q_2)\frac{s-2m_\pi^2}{\sqrt{s(s-4m_\pi^2)}}\ln\left(\frac{\sqrt{s}+\sqrt{s-4m_\pi^2}}{\sqrt{s}-\sqrt{s-4m_\pi^2}}\right)\right. \\
& +2(Q_aQ_1+Q_bQ_2)\frac{2m_\pi^2-t}{\sqrt{t(t-4m_\pi^2)}}\ln\left(\frac{\sqrt{-t+4m_\pi^2}+\sqrt{-t}}{\sqrt{-t+4m_\pi^2}-\sqrt{-t}}\right) \\
& \left. +2(Q_aQ_2+Q_bQ_3)\frac{s-2m_\pi^2+t}{\sqrt{(s+t)(s+t-4m_\pi^2)}}\ln\left(\frac{\sqrt{s+t}+\sqrt{s+t-4m_\pi^2}}{\sqrt{s+t}-\sqrt{s+t-4m_\pi^2}}\right)\right\}. \qquad (137)
\end{aligned}
$$

In Eq. (135), $d\sigma_{el}(s)/dt$ is the on-shell differential elastic $\pi+\pi$ cross section, which is a function of the invariant energy $\sqrt{s}$ and the pion scattering angle via the four-momentum transfer squared t.

The expression (135) is considerably simpler in comparison to the "full" OBE formula (130) due to the factorization of the diagrams from Fig. 20 into an electromagnetic part and an elastic $\pi+\pi\to\pi+\pi$ subprocess, for the cross section of which the photon q-dependence is omitted. This corresponds to neglecting the off-shellness of the pion emitting the photon, e.g. for the pion a:

$$p_a - q \approx p_a. \qquad (138)$$

Consequently, the sub-process invariant energy $\sqrt{s_2}$ is also approximated by the total invariant energy $\sqrt{s}$ of the process $\pi+\pi\to\pi+\pi+\gamma$:

$$s_2 \equiv (p_a+p_b-q)^2 \approx (p_a+p_b)^2 = s, \qquad (139)$$

and the limits of integration over t are also taken as for the on-shell case, i.e. from $-\lambda(s,m_a^2,m_b^2)/s$ to 0, while the actual integration over the full 3-particle phase space R_3 in the exact treatment (130) involves different limits for t.

In Fig. 19 (r.h.s.) we show the resulting cross sections for the photon production in the process $\pi+\pi\to\pi+\pi+\gamma$ within the following models: the "full" OBE taking into account scalar, vector and tensor interactions via the exchange of σ, ρ and $f_2(1270)$-mesons (red line with star symbols), the soft photon approximation (135) to this model (blue dotted line); the OBE result employing only the scalar and vector interactions via the exchange of σ and ρ mesons (blue dashed line), and the soft photon approximation to this model (cyan dash-dot-dotted line). For the very low energy of the photon of $q_0 = 5$ MeV the SPA agrees with the "exact"

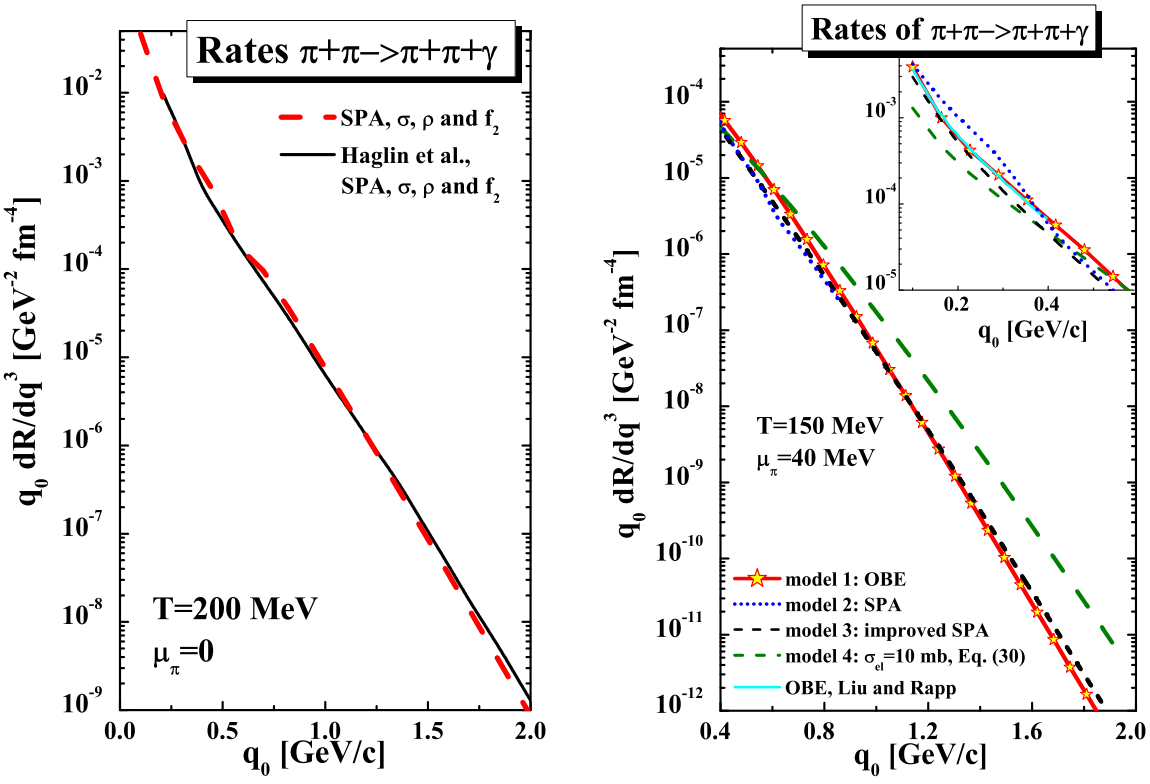


Figure 21: (l.h.s.) Invariant rate of the bremsstrahlung-photon production from an equilibrated pion gas at a temperature of $T = 200$ MeV and pion chemical potential $\mu_\pi = 0$ as calculated in the OBE model with three resonance exchange within the soft-photon approximation (red dashed line). The black solid line from Ref. [136] is shown for comparison and validation of our calculations. (r.h.s.) Invariant rate of bremsstrahlung photons produced from an equilibrated pion gas at $T = 150$ MeV and $\mu_\pi = 40$ MeV versus the photon energy q_0. The in-let shows the same quantity for the range of photon energies $q_0 = 0.1 - 0.4$ GeV. The calculations have been performed within the following models: (1) OBE model beyond the soft-photon approximation (red solid line with star symbols); (2) OBE model within the soft photon approximation (blue dotted line); (3) OBE model within the improved soft photon approximation (black short-dashed line) – the invariant energy $\sqrt{s_2}$ of the on-shell $\pi + \pi$ elastic process is not equal to the total invariant energy of the process $\sqrt{s}$: $s_2 = s - q_0\sqrt{s}$; (4) the soft photon approximation with the constant isotropic elastic cross section of $\sigma_{el} = 10$. The cyan solid line from Liu and Rapp [130] is shown for comparison. The figures are taken from Ref. [102].

cross section very well in the region of $\sqrt{s} < 0.9$ GeV (see Fig. 19, r.h.s.). However, the discrepancy to the OBE result is increasing rapidly with growing $\sqrt{s}$; the calculations for the higher photon energy of $q_0 = 0.5$ GeV show an even larger discrepancy between the SPA and the exact OBE result (cf. Ref. [102]).

Using the cross section for the $\pi + \pi \to \pi + \pi + \gamma$ reaction according to Eq. (135) as a function of the photon energy q_0 and the collision energy $\sqrt{s}$, the yield dN/d^3q and the invariant rate $q_0 dR/d^3q$ for bremsstrahlung photon production from an equilibrated pion gas can be evaluated in a straight forward manner. Within kinetic theory, the rate of photon production in the collisions of particles a and b in a thermalized medium (number of photons produced per unit space-time volume d^4x) is an integral over the three-momenta of the incoming particles (in the classical limit):

$$q_0 \frac{dN}{dx^4 d^3q} = g \int ds \int \frac{d^3p_a}{(2\pi)^3} \int \frac{d^3p_b}{(2\pi)^3} \, e^{-(E_a+E_b)/T} \; v_{rel} \; q_0 \, \frac{d\sigma^\gamma}{d^3q} \delta(s - (p_a + p_b)^2), \tag{140}$$

where T is the temperature, v_{rel} is the relative velocity given by

$$v_{rel} = \frac{\sqrt{(p_a \cdot p_b)^2 - m_a^2 m_b^2}}{E_a E_b}, \tag{141}$$

and $g = (2s_a + 1)(2s_b + 1)$ is the spin degeneracy factor. Integrating the expression (140) over the particle

momenta one obtains [96]:

$$q_0 \frac{dN}{d^4x d^3q} = \frac{T^6 g}{16\pi^4} \int\limits_{z_{min}}^{\infty} dz \frac{\lambda(z^2T^2, m_a^2, m_b^2)}{T^4} K_1(z) q_0 \frac{d\sigma^\gamma}{d^3q}, \tag{142}$$

where $z_{min} = (m_a + m_b)/T$, $z = \sqrt{s}/T$, and $K_1(z)$ is the modified Bessel function.

The expression (140) can be generalized to account for quantum effects such as Bose enhancement or Pauli blocking (depending on the particle type) by integrating additionally over the momenta of the final particles and changing the Boltzmann distributions to Fermi or Bose distribution functions $f_i(T)$:

$$q_0 \frac{dN}{dx^4 d^3q} = g \int ds \int \frac{d^3p_a}{(2\pi)^3} \int \frac{d^3p_b}{(2\pi)^3} \int \frac{d^3p_1}{(2\pi)^3} \int \frac{d^3p_1}{(2\pi)^3} f_a(T) f_b(T) (1 \pm f_1(T))(1 \pm f_2(T)) \times v_{rel}\ q_0 \frac{d\sigma^\gamma}{d^3q} \delta(s - (p_a + p_b)^2), \tag{143}$$

where the (-) sign has to be used in case of fermions. In the current Subsection we calculate the thermal rates according to formula (140). However, within the PHSD transport approach for the heavy-ion collisions in Section 6 the effects of the quantum statistics will be taken into account (although of subleading importance).

In Fig. 21 (l.h.s.) the rates are presented for a temperature $T = 200$ MeV and pion chemical potential $\mu_\pi = 0$ for the OBE model with three resonance exchanges adopting the soft-photon approximation (red dashed line). We confirm the results from Haglin [136] (black solid line) calculated within the same assumptions (SPA, three resonances) but with a slightly different parameter set of the Lagrangian. It is, however, questionable that the SPA is applicable at high photon energies.

We note that the accuracy of the SPA approximation can be significantly improved and the region of its applicability can be extended by slightly modifying the formula (135) – i.e. by evaluating the on-shell elastic cross section at the invariant energy $\sqrt{s_2}$ of the sub-process. The latter is kinematically fixed to

$$s_2 = s - q_0\sqrt{s} \neq s. \tag{144}$$

Thus the modified SPA formula is

$$q_0 \frac{d\sigma^\gamma(s)}{d^3q} = \frac{\alpha_{EM}}{4\pi} \int\limits_{-\lambda(s_2, m_a^2, m_b^2)/s_2}^{0} |\epsilon \cdot J(q,t)|^2 \frac{d\sigma_{el}(s_2)}{dt} dt. \tag{145}$$

In the following, we will denote the approximation (145) as "improved SPA" and will show below that it provides a fairly good description of the exact photon production rates.

It is instructive to compare the photon production rates beyond the soft photon approximation for the $\pi + \pi \to \pi + \pi + \gamma$ reaction to the rates from the exact OBE expression (130). We present the calculated invariant rate $q_0 dR/dq^3$ of bremsstrahlung photons produced from an equilibrated pion gas at $T = 150$ MeV and $\mu_\pi = 40$ MeV in Fig. 21 (r.h.s.). The results of the following models are compared:

- model 1 (red solid line): exact rates within the one-boson exchange model (OBE) *beyond* the soft-photon approximation – i.e. using the formula (130) for the photon production cross section $q_0\ d\sigma^\gamma/d^3q$;
- model 2 (blue dotted line): result within the soft photon approximation – i.e. using the formula (135) – while using the elastic $\pi + \pi$ cross section calculated within the OBE model as given by equations (125)-(128);
- model 3 (black short-dashed line): results of the *improved* soft photon approximation – i.e. using the formula (145) in stead of (135) – and the same pion elastic scattering cross section as in the model 2;
- model 4 (upper green dashed line): soft photon approximation using a constant isotropic elastic cross section of $\sigma_{el} = 10$ mb and assuming for the pion charges $Q_a = Q_1 = 1$, $Q_b = Q_2 = 0$. In this case the elastic cross section does not depend on $\sqrt{s}$ and thus there is no difference between the SPA and improved SPA.

The rate of bremsstrahlung photons at low transverse momenta $p_T < 0.4$ GeV has been calculated before by Liu and Rapp in Ref. [130] within the one-boson exchange model with the exchange of two resonances for the same system. This previous result is shown for comparison by the cyan dashed line and is confirmed by our present calculations. The agreement is expected, since our calculations differ only in the inclusion of the f_2-meson exchange, which is important for larger $\sqrt{s}$ and does not play an important role for the production of low transverse momentum photons, which is dominated by low $\sqrt{s}$ of the $\pi + \pi$ collisions.

On the other hand, the SPA (model 2) deviates from the exact OBE result (model 1) even at low q_0 because the former directly follows the $\sqrt{s}$ dependence of the elastic $\pi - \pi$ cross section. Since the formula (135) does not account for the off-shellness of the emitting pion, it overestimates the high-$\sqrt{s}$ regime of the elastic cross section in line with the findings of Refs. [96, 129]. We note that the OBE model presented here is constrained by the pion scattering data only up to $\sqrt{s_{\pi\pi}} = 1.4$ GeV and generally cannot be extended to larger $\sqrt{s}$. Thus the SPA scenario "model 2" is not reliable for large q_0 (approximately for $q_0 > 0.8$ GeV). This is not the case for the improved SPA (model 3).

One can see in Fig. 21 (r.h.s.) that the *improved* SPA (145) gives a very good approximation to the exact result at higher photon energies of up to $q_0 \approx 2$ GeV. This is because the $\sqrt{s_2}$ of the subprocess is always below $\sqrt{s}$, and the OBE model for the elastic cross section is sufficiently realistic in this region of $\sqrt{s_2}$. In comparison, the constant cross-section approximation overestimates the exact rates for $q_0 > 1$ GeV and underestimates for $q_0 < 0.4$ GeV. This model corresponds to the approximation used previously in the transport calculations in Refs. [98, 100, 101] for an estimate of the photon bremsstrahlung in meson+meson collisions. In the following we will report on results based on the exact OBE cross section $d\sigma^\gamma/d^3q$ for $\pi + \pi$ bremsstrahlung. The bremsstrahlung photon production in collisions of other meson types is treated in analogy to the $\pi + \pi$ collisions by means of mass-scaled cross sections.

We note that another important source of photons is the bremsstrahlung in *meson+ baryon* collisions. As we have shown above, the SPA gives a good approximation to the exact rates, if we use the correct invariant energy in the hadronic subprocess $s_2 = s - q_0\sqrt{s}$ and a realistic model for the differential cross section of the subprocess, i.e. for the elastic scattering of mesons on baryons. The cross sections for the meson+baryon elastic scatterings (implemented within the PHSD transport approach) have been previously adjusted to the data differentially in energy and angular distribution. Thus we evaluate the photon production in the processes $m + B \to m + B + \gamma$ in the PHSD by using realistic elastic scattering cross sections taken at the correct invariant energy $\sqrt{s_2}$ in the scope of the improved SPA.

5.5. Binary meson+meson and meson+nucleon reactions

We calculate the cross sections for the processes $\pi\pi \to \rho\gamma, \pi\rho \to \pi\gamma$ as in Ref. [100], i.e. the total cross section $\sigma_{\pi\pi\to\rho\gamma}(s, \rho_N)$ is obtained by folding the vacuum cross section $\sigma^0_{\pi\pi\to\rho\gamma}(s, M)$ with the (in-medium) spectral function of the ρ meson:

$$\sigma_{\pi\pi\to\rho\gamma}(s, \rho_N) = \int_{M_{min}}^{M_{max}} dM\ \sigma^0_{\pi\pi\to\rho\gamma}(s, M)\ A(M, \rho_N)\ P(s). \tag{146}$$

Here $A(M, \rho_N)$ denotes the meson spectral function for given total width Γ^*_V:

$$A_V(M, \rho_N) = C_1\ \frac{2}{\pi}\ \frac{M^2\ \Gamma^*_V(M, \rho_N)}{(M^2 - M_0^{*^2}(\rho_N))^2 + (M\Gamma^*_V(M, \rho_N))^2}, \tag{147}$$

with the normalization condition for any ρ_N, $\int_{M_{min}}^{M_{lim}} A_V(M, \rho_N)\ dM = 1$, where $M_{lim} = 2$ GeV is chosen as an upper limit for the numerical integration while the lower limit of the vacuum ρ spectral function corresponds to the 2π decay threshold $M_{min} = 2m_\pi$ in vacuum and $2m_e$ in medium. M^*_0 is the pole mass of the vector meson spectral function which is $M^*_0(\rho_N = 0) = M_0$ in vacuum, however, might be shifted in the medium (e.g. for the dropping mass scenario). Furthermore, the vector meson width is the sum of the vacuum total decay width and collisional width:

$$\Gamma^*_V(M, \rho_N) = \Gamma_V(M) + \Gamma_{coll}(M, \rho_N). \tag{148}$$

In Eq. (146) the function $P(S)$ accounts for the fraction of the available part of the full spectral function $A(M, \rho_N)$ at given energy $\sqrt{s}$, integrated over the mass M up to $M_{max} = \sqrt{s}$, with respect to the total phase space.

The cross section $\sigma^0_{\pi\pi\to\rho\gamma}(s,M)$ is taken in line with the model by Kapusta et al. [137] with the ρ-meson mass considered as a dynamical variable, i.e $m_\rho \to M$:

$$\frac{d\sigma}{dt}\left(\pi^\pm\pi^0 \to \rho^\pm\gamma\right) = -\frac{\alpha g_\rho^2}{16 s p_{CM}^2}\left[\frac{(s-2M^2)(t-m_\pi^2)^2}{M^2(s-M^2)^2} + \frac{m_\pi^2}{M^2} - \frac{9}{2} + \frac{(s-6M^2)(t-m_\pi^2)}{M^2(s-M^2)} + \frac{4(M^2-4m_\pi^2)s}{(s-M^2)^2} + \frac{4(M^2-4m_\pi^2)}{t-m_\pi^2}\left(\frac{s}{s-M^2}+\frac{m_\pi^2}{t-m_\pi^2}\right)\right]. \quad (149)$$

The photon production in the $\pi+\rho$ interaction is calculated analogously (cf. Ref. [100] for details).

We recall that the PHSD and HSD are off-shell transport approaches and thus allow to study the effect of the modification of the vector-meson spectral functions in the medium. In particular the photon production in secondary meson interactions is sensitive to the properties of the vector mesons at finite density and temperature [100, 138, 139]. In this respect, we stress here that the yields and the in-medium spectral functions of vector mesons in PHSD have been independently constrained by the comparison to the data on dilepton mass-spectra (see Refs. [140, 141, 142] and Section 7, respectively).

We have incorporated into the PHSD approach additionally the $2 \to 2$ processes $V + N \to N + \gamma$, where V stands for a vector meson while N denotes a proton or neutron [102]. These processes are the baryonic counterparts to the mesonic $2 \to 2$ reactions $\pi + \rho/\pi \to \gamma + \pi/\rho$. We consider the interaction of nucleons with the mesons $V = \rho$, ϕ, ω, taking into account the various possible charge combinations, e.g. $\rho^0 + p \to \gamma + p$, $\rho^- + p \to \gamma + n$, $\rho^+ + n \to \gamma + p$, etc. In order to evaluate the probabilities for photon production in the collisions of vector mesons with nucleons, we use the inverse photoproduction processes $\gamma + N \to \rho + N$, $\gamma + N \to \phi + N$, $\gamma + N \to \omega + N$ (controlled by data) and employ detailed balance to obtain the differential cross sections for the processes $\rho + N \to \gamma + N$, $\phi + N \to \gamma + N$, $\omega + N \to \gamma + N$, i.e.

$$\sigma(NV \to \gamma N) = \frac{g_\gamma}{g_V}\frac{p^{*2}_{N\gamma}}{p^{*2}_{NV}}\,\sigma(\gamma N \to NV), \quad (150)$$

where $g_\gamma = 2$ and $g_V = 3$ are the spin degeneracy factors of the photon and the vector meson V. In Eq. (150) $p^*_{N\gamma}$ is the center-of-mass momentum in the $N + \gamma$ system and p^*_{NV} is the center-of-mass momentum in the $N + V$ system.

The cross sections for the exclusive photo-production of ρ, ϕ and ω vector mesons on the nucleon have been measured by the Aachen-Berlin-Bonn-Hamburg-Heidelberg-Munich (ABBHHM) Collaboration and published in Ref. [143]. In the same work also parametrizations for these cross section have been given that are based on the vector-meson-dominance model with a non-relativistic Breit-Wigner (BW) spectral function for the ρ-meson. Later, the fits have been updated in Ref. [144] using relativistic BW spectral functions for ρ, ω and ϕ mesons. The total cross sections – fitted in Ref. [144] to the data from Ref. [143] – are given by

$$\sigma(\gamma N \to VN) = \frac{1}{p^*_{N\gamma} s}\int d\mu |M_V|^2 p^*_{NV} A_V(\mu), \quad (151)$$

where the mass μ of the vector meson is distributed according to the spectral function $A_V(\mu)$:

$$A_V(\mu) = \frac{2}{\pi}\frac{\mu^2\Gamma(\mu)}{(\mu^2 - M_i^2)^2 + \mu^2\Gamma^2(\mu)}, \quad (152)$$

with M_i denoting the pole mass of the meson. The matrix elements for the reactions $\gamma + N \to V + N$ are parametrized as

$$\begin{aligned} |M_\rho|^2 &= 0.16 \text{ mb GeV}^2, \\ |M_\omega|^2 &= \frac{0.08\ p^{*2}_{VN}}{2(\sqrt{s} - 1.73\ \text{GeV})^2 + p^{*2}_{VN}} \text{ mb GeV}^2, \\ |M_\phi|^2 &= 0.004 \text{ mb GeV}^2. \end{aligned} \quad (153)$$

The cross sections (151) with the parameters (153) are consistent with the dynamics of vector mesons in the PHSD/HSD, where also relativistic BW spectral functions for vector mesons are used and propagated off-shell.

For the angular distribution of the ρ-meson production in the process $\gamma+N \rightarrow N+\rho$, we follow the suggestion of Ref. [144],

$$\frac{d\sigma}{dt} \sim \exp(Bt), \tag{154}$$

with the photon-energy dependent parameter B (fitted to the data): $B = 5.7$ for $q_0 \leq 1.8$ GeV, $B = 5.43$ for $1.8 < q_0 \leq 2.5$ GeV, $B = 6.92$ for $2.5 < q_0 \leq 3.5$ GeV, $B = 8.1$ for $3.5 < q_0 \leq 4.5$ GeV, $B = 7.9$ for $q_0 > 4.5$ GeV. The data in Ref. [144] have shown that the cross section is dominated by the $t \approx 0$ region in line with the vector dominance model (VDM) where the process $\gamma + N \rightarrow V + N$ is described by the incident photon coupling to the vector meson of helicity ± 1, which consequently is scattered elastically by the nucleon.

5.6. Dilepton sources

Dileptons (e^+e^-, $\mu^+\mu^-$ pairs or virtual photons) can be emitted from all stages of the heavy-ion reactions as well as real photons. One of the advantages of dileptons – compared to photons – is an additional 'degree-of-freedom': the invariant mass M which allows to disentangle various sources. There are the following production sources of dileptons in $p+p, p+A$ and $A+A$ collisions:
1) Hadronic sources:
(i) at low invariant masses ($M < 1$ GeVc) – the Dalitz decays of mesons and baryons ($\pi^0, \eta, \Delta, ...$) and the direct decay of vector mesons (ρ, ω, ϕ) as well as hadronic bremsstrahlung [100];
(ii) at intermediate masses (1 GeV$< M < 3$ GeV) – leptons from correlated $D + \bar{D}$ pairs [140], radiation from multi-meson reactions ($\pi+\pi,\ \pi+\rho,\ \pi+\omega,\ \rho+\rho,\ \pi+a_1, ...$) denoted by "$4\pi$" contributions [138, 145, 146, 147];
(iii) at high invariant masses ($M > 3$ GeV) – the direct decay of vector mesons ($J/\Psi, \Psi'$) [148] and initial 'hard' Drell-Yan annihilation to dileptons ($q + \bar{q} \rightarrow l^+ + l^-$, where $l = e, \mu$) [113].
2) 'thermal' QGP dileptons radiated from the partonic interactions in heavy-ion collisions that contribute dominantly to the intermediate masses. The leading processes are the 'thermal' $q\bar{q}$ annihilation ($q+\bar{q} \rightarrow l^+ + l^-$, $q + \bar{q} \rightarrow g + l^+ + l^-$) and Compton scattering ($q(\bar{q}) + g \rightarrow q(\bar{q}) + l^+ + l^-$) in the QGP [137].

The dilepton production by a (baryonic or mesonic) resonance R decay can be schematically presented in the following way:

$$BB \rightarrow RX \tag{155}$$
$$mB \rightarrow RX \tag{156}$$
$$R \rightarrow e^+e^-X, \tag{157}$$
$$R \rightarrow mX,\ m \rightarrow e^+e^-X, \tag{158}$$
$$R \rightarrow R'X,\ R' \rightarrow e^+e^-X, \tag{159}$$

i.e. in a first step a resonance R might be produced in baryon-baryon (BB) or meson-baryon (mB) collisions (155), (156) or be formed in the hadronization process. Then this resonance can couple to dileptons directly (157) (e.g., Dalitz decay of the Δ resonance: $\Delta \rightarrow e^+e^-N$) or decays to a meson m (+ baryon) or in (158) produce dileptons via direct decays (ρ, ω) or Dalitz decays (π^0, η, ω). The resonance R might also decay into another resonance R' (159) which later produces dileptons via Dalitz decay.

The electromagnetic part of all conventional dilepton sources – π^0, η, ω Dalitz decays, direct decay of vector mesons ρ, ω and ϕ – are described in detail in Ref. [149] – where dilepton production in pp and pd reactions has been studied. Actual modifications – relative to Ref. [149] – are related to the Dalitz decay of baryonic resonances and especially the strength of the pp and pn bremsstrahlung since calculations by Kaptari and Kämpfer in 2006 [150] indicated that the latter channels might have been severely underestimated in previous studies on dilepton production at SIS energies. For the results reported here we adopt the parametrizations from Ernst et al. [151] (Eqs. (9) to (13)) for the Dalitz decays of the baryonic resonances which are also incorporated in the PLUTO simulation program of the HADES Collaboration. For the bremsstrahlung channels in pp and pn reactions we adopt the results from the OBE model calculations by Kaptari and Kämpfer in Ref. [150].

5.7. Vector-meson spectral functions

In order to explore the influence of in-medium effects on the vector-meson spectral functions we incorporate the effect of collisional broadening (as in Refs. [152, 153, 154]), i.e. the vector meson width has been implemented as:

$$\Gamma^*_V(M, |\vec{p}|, \rho_N) = \Gamma_V(M) + \Gamma_{coll}(M, |\vec{p}|, \rho_N). \tag{160}$$

Here $\Gamma_V(M)$ is the total width of the vector mesons ($V = \rho, \omega$) in the vacuum. For the ρ meson we use

$$\Gamma_\rho(M) \simeq \Gamma_{\rho\to\pi\pi}(M) = \Gamma_0 \left(\frac{M_0}{M}\right)^2 \left(\frac{q}{q_0}\right)^3 F(M), \qquad (161)$$
$$q = \frac{(M^2 - 4m_\pi^2)^{1/2}}{2}, \quad q_0 = \frac{(M_0^2 - 4m_\pi^2)^{1/2}}{2}.$$

In Eqs. (161) M_0 is the vacuum pole mass of the vector meson spectral function, $F(M)$ is a formfactor taken from Ref. [155] as

$$F(M) = \left(\frac{2\Lambda^2 + M_0^2}{2\Lambda^2 + M^2}\right)^2 \qquad (162)$$

with a cut-off parameter $\Lambda = 3.1$ GeV. This formfactor was introduced in Ref. [155] in order to describe the e^+e^- experimental data with better accuracy. For the ω meson a constant total vacuum width is used: $\Gamma_\omega \equiv \Gamma_\omega(M_0)$, since the ω is a narrow resonance in vacuum.

The collisional width in Eq. (160) is approximated as

$$\Gamma_{coll}(M, |\vec{p}|, \rho_N) = \gamma\ \rho_N < v\ \sigma_{VN}^{tot} > \approx\ \alpha_{coll}\ \frac{\rho_N}{\rho_0} .... \qquad (163)$$

Here $v = |\vec{p}|/E$; $\vec{p}$, E are the velocity, 3-momentum and energy of the vector meson in the rest frame of the nucleon current and $\gamma^2 = 1/(1 - v^2)$. Furthermore, ρ_N is the nuclear density and σ_{VN}^{tot} the meson-nucleon total cross section. The parameter α_{coll} is determined dynamically within the transport calculation by recording the ρ collision rate as a function of the baryon density ρ_N.

In order to explore the observable consequences of vector-meson mass shifts at finite nuclear density – as suggested by the CBELSA-TAPS data [156] for the ω meson – the in-medium vector meson pole masses are modeled (optionally) according to the Hatsuda and Lee [157] or Brown/Rho scaling [158, 159] as

$$M_0^*(\rho_N) = \frac{M_0}{(1 + \alpha\rho_N/\rho_0)}, \qquad (164)$$

where ρ_N is the nuclear density at the resonance decay position $\vec{r}$; $\rho_0 = 0.16$ fm^{-3} is the normal nuclear density and $\alpha \simeq 0.16$ for the ρ and $\alpha \simeq 0.12$ for the ω meson [160]. The parametrization (164) may be employed also at much higher collision energies (e.g. FAIR and SPS) and one does not have to introduce a cut-off density in order to avoid negative pole masses. Note that the effective mass (164) is uniquely fixed by the 'customary' expression $M_0^*(\rho_N) \approx M_0(1 - \alpha\rho_N/\rho_0)$ in the low density regime.

The resulting spectral functions for the ρ and ω meson are displayed in Fig. 22 for the case of 'collisional broadening' (upper part) as well as for the 'dropping mass + collisional broadening' scenario (lower part) for densities of 0,1,2,3,5 $\times\rho_0$. Note that in vacuum the hadronic widths vanish for the ρ below the two-pion mass and for the ω below the three-pion mass. With increasing nuclear density ρ_N elastic and inleastic interactions of the vector mesons shift strength to low invariant masses. In the 'collisional broadening' scenario we find a dominant enhancement of strength below the pole mass for the ρ meson while the ω meson spectral function is drastically enhanced in the low- and high-mass region with density (on expense of the pole-mass regime). In the 'dropping mass + collisional broadening' scenario both vector mesons dominantly show a shift of strength to low invariant masses with increasing ρ_N. Qualitatively similar pictures are obtained for the ϕ meson but quantitatively smaller effects are seen due to the lower effect of mass shifts and a substantially reduced ϕN cross section which is a consequence of the $s\bar{s}$ substructure of the ϕ meson. Since the ϕ dynamics turn out to be of minor importance for the dilepton spectra to be discussed below we discard an explicit representation. The 'family' of spectral functions shown in Fig. 22 allows for a sufficient flexibility with respect to the possible scenarios outlined above. A comparison to dilepton data is expected to provide further constraints on the possible realizations.

5.8. Off-shell propagation and the time-integration method

The propagation of broad resonances in the off-shell transport approach has been described in Section 2.7 above. In order to demonstrate the importance of off-shell transport dynamics we present in Fig. 23 the time

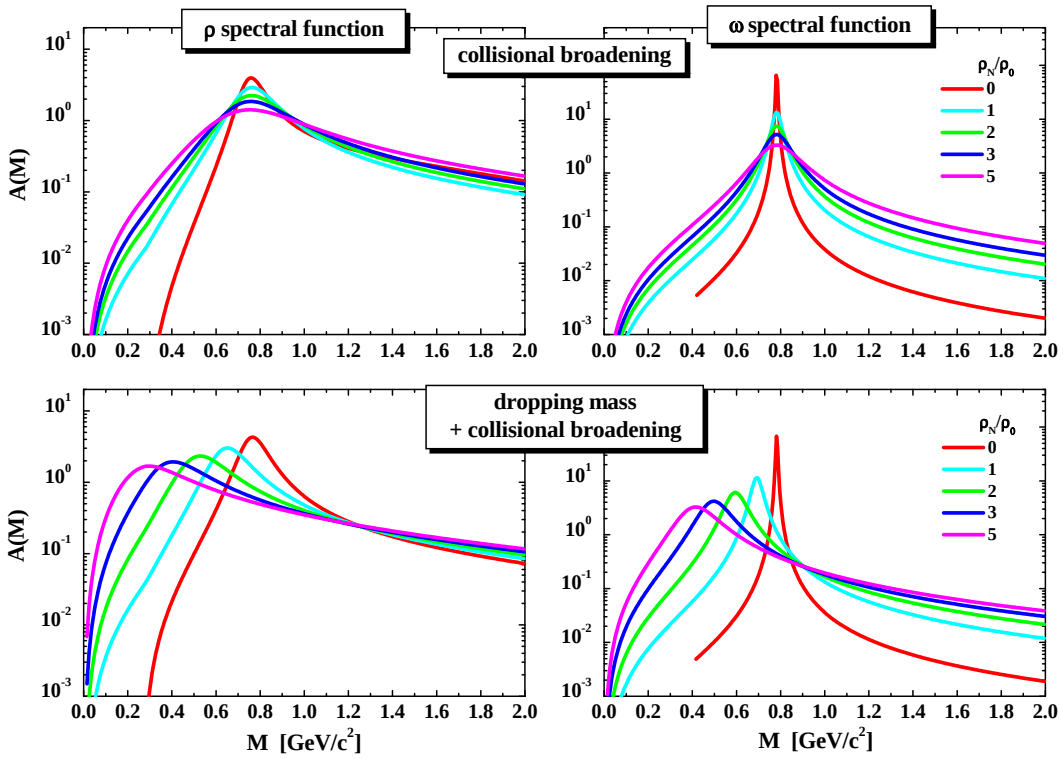


Figure 22: The spectral functions for the ρ and ω meson in the case of the 'collisional broadening' scenario (upper part) and the 'dropping mass + collisional broadening' scenario (lower part) for nuclear densities of 0,1,2,3,5$\times\rho_0$ as employed in the transport calculations (see text for details). The figures are taken from Ref. [161].

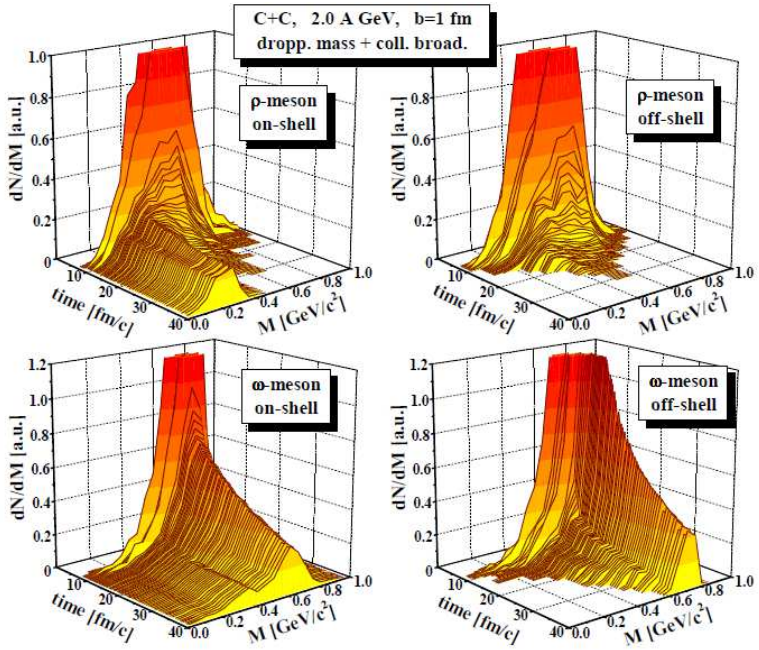


Figure 23: Time evolution of the mass distribution of ρ (upper part) and ω (lower part) mesons for central $C+C$ collisions (b=1 fm) at 2 A GeV for the dropping mass + collisional broadening scenario. The l.h.s. of Fig. 23 correspond to the calculations with on-shell dynamics whereas the r.h.s. show the off-shell results. The figures are taken from Ref. [161].

evolution of the mass distribution of ρ (upper part) and ω (lower part) mesons for central C+C collisions (b=1 fm) at 2 A GeV for the dropping mass + collisional broadening scenario (as an example). The l.h.s. of Fig. 23 corresponds to the calculations with on-shell propagation whereas the r.h.s. show the results for the off-shell dynamics. As seen from Fig. 23 the initial ρ and ω mass distributions are quite broad even for a small system such as $C + C$ where, however, the baryon density at 2 A GeV may reach (in some local cells) up to $2\rho_0$. The number of vector mesons decreases with time due to their decays and the absorption by baryons ($\rho N \to \pi N$ or $\rho N \to \pi\pi N$). Most of the ρ mesons decay/disappear already inside the "fireball" for density $\rho_N > 0$. Due to the "fireball" expansion the baryon density drops quite fast, so some amount of ρ (and ω) mesons reach the very low density zone or even the 'vacuum'. Since for the off-shell case (r.h.s. of Fig. 23) the ρ and ω spectral functions change dynamically by propagation in the dense medium according to Eqs. (59) and (60) they regain the vacuum shape for $\rho_N \to 0$. This does not happen for the on-shell treatment (l.h.s. of Fig. 23); the ρ spectral function does not change its shape by propagation but only by explicit collisions with other particles. Indeed, there is a number of ρ's which survive the decay or absorption and leave the "fireball" with masses below $2m_\pi$.

Accordingly, the approximate on-shell propagation leads to the appearance of ρ mesons in the vacuum with $M \leq 2m_\pi$, which can not decay to two pions; thus they live practically 'forever' since the probability to decay to other channels is very small. Indeed, such ρ's will continuously shine low mass dileptons which leads to an apparent 'enhancement/divergence' of the dilepton yield at low masses (note, that the dilepton yield is additionally enhanced by a factor $\sim 1/M^3$). The same statements are valid for the ω mesons (cf. lower part of Fig. 23): since the ω meson is a long living resonance, a larger amount of ω's survives with an in-medium like spectral function in the vacuum (in case of on-shell dynamics). Such ω's with $M < 3m_\pi$ can decay only to $\pi\gamma$ or electromagnetically (if $M < m_\pi$). Since such phenomena appearing in on-shell transport descriptions (including an explicit vector-meson propagation) contradict basic physical principles, an off-shell treatment is mandatory.

Since the dilepton production is a very rare process (e.g. the branching ratio for the vector meson decay is $\sim 10^{-5}$), a perturbative method is used in the transport calculation in order to increase statistics. In the PHSD approach (in this report as well as in earlier investigations [140, 142, 161, 162, 163, 148]) we use the time integration (or 'shining') method first introduced by Li and Ko in Ref. [164]. The main idea of this method is that dileptons can be emitted during the full lifetime of the resonance R before its strong decay into hadrons or absorption by the surrounding medium. For example, the ρ^0 decay (with invariant mass M) to e^+e^- during the propagation through the medium from the production time $t = 0$ up to the final ("death") time t_F – which might correspond to an absorption by baryons or to reactions with other hadrons as well as the strong decay into two pions – is calculated as

$$\frac{dN^{\rho\to e^+e^-}}{dM} = \sum_{t=0}^{t_F} \Gamma^{\rho^0\to e^+e^-}(M) \cdot \frac{\Delta t}{\gamma(\hbar c)} \cdot \frac{1}{\Delta M} \tag{165}$$

in the mass bin ΔM and time step Δt (in fm/c). In (165) γ is the Lorentz factor of the ρ-meson with respect to the calculational frame. The electromagnetic decay width is defined as

$$\Gamma^{\rho^0\to e^+e^-}(M) = C_\rho \frac{M_0^{*4}}{M^3}, \tag{166}$$

where $C_\rho = \Gamma^{\rho\to e^+e^-}(M_0)/M_0$. Here M_0 is the vacuum pole mass, M_0^* is the in-medium pole mass which is equal to the vacuum pole mass for the collisional broadening scenario, however, is shifted for the dropping mass scenario according to Eq. (164). The time integration method allows to account for the full in-medium dynamics of vector mesons from production ("birth") up to their "death". In case of the ρ propagation in the vacuum only the 2 pion-decay channel contributes and the default results are regained after time integration.

5.9. e^+e^- bremsstrahlung in $p + p$ and $p + n$ reactions

The soft-photon approximation (SPA) [105, 106, 107] has been discussed in detail in Section 5.4 in case of meson-meson collisions. In spite of the general limitation of the SPA it has been widely used for the calculation of the bremsstrahlung dilepton spectra by different transport groups [39, 92, 151, 165]. Note, at those early times the applicability of the SPA for an estimate of dilepton radiation from NN collisions at 1-2 GeV bombarding energies has been supported by independent One-Boson-Exchange (OBE) model calculations by Schäfer et al. [166] and later on by Shyam et al. [167]. In these models the effective parameters have been adjusted to describe

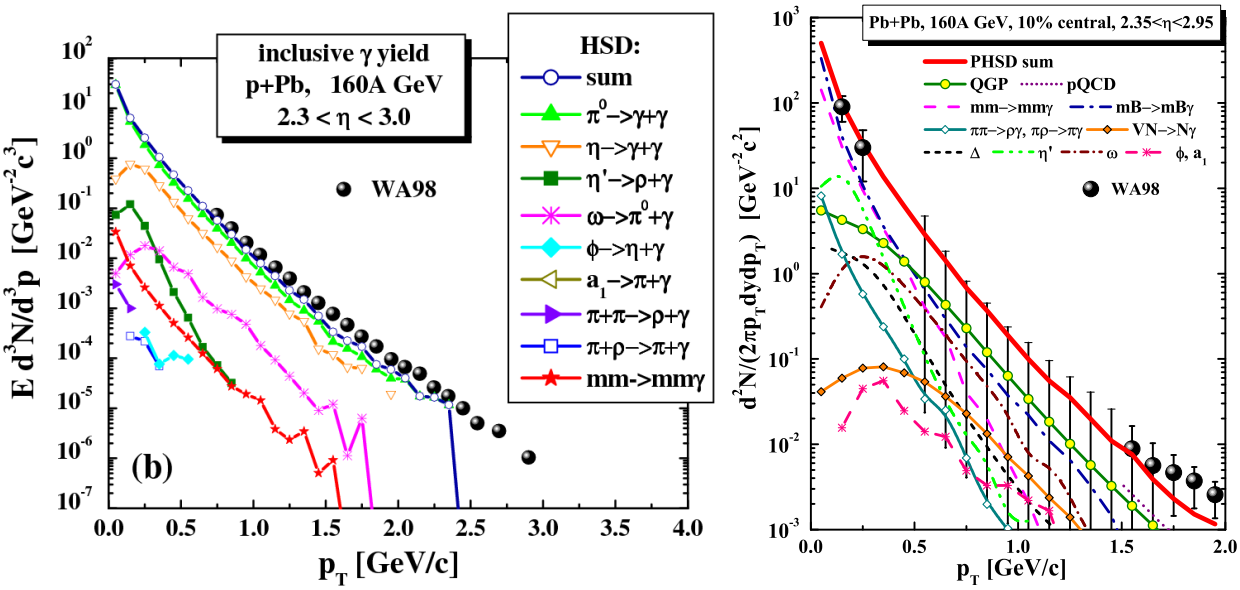


Figure 24: (l.h.s.) Comparison of the PHSD/HSD calculations for *inclusive* photons for p+Pb collisions at 160 GeV to the data of the WA98 Collaboration from Refs. [170, 171]. See legend for the contribution from the individual channels. (r.h.s.) Comparison of the PHSD calculations for *direct* photons from Pb+Pb at 158 A GeV collisions to the data of the WA98 Collaboration from Refs. [170, 171]. In comparison to the original HSD study [100]: (i) the meson+baryon bremsstrahlung (blue dash-dotted line), Δ decays (black short-dashed line) and the photons from QGP (green line with round symbols) are added (ii) and the meson+meson bremsstrahlung is now calculated beyond the SPA (magenta dashed line). The black line with diamond symbols labeled as "other" includes: ω, η', ϕ an d a_1-meson decays, binary channels $\pi + \rho/\pi \to \pi/\rho + \gamma$ and $N + V \to N + \gamma$. The figures are taken from Refs. [100, 102].

elastic NN scattering at intermediate energies. The models have then been applied to bremsstrahlung processes including the interference of different diagrams for the dilepton emission from all charged hadrons. As shown in Ref. [166] the pp bremsstrahlung is much smaller than pn bremsstrahlung due to a destructive interference of amplitudes from the initial and final radiation. We note that gauge invariant results have been obtained in Refs. [166, 167] by 'gauging' the phenomenological form factors at the meson-baryon vertices. However, there are different schemes to introduce gauge invariance in OBE models - as stressed by Kondratyuk and Scholten [168] - which lead to sizeably different cross sections. One also has to point out that already in 1997 an independent study by de Jong et al. [169] - based on a full T-matrix approach - has indicated that the validity of the SPA for e^+e^- bremsstrahlung at intermediate energies of 1-2 GeV may be very questionable. However, in Ref. [169] only the pp reaction has been considered; indeed, the bremsstrahlung in the full T-matrix approach is larger by a factor of about 3 than the corresponding SPA calculations (and OBE results).

In 2005 new covariant OBE calculations for dilepton bremsstrahlung have been performed by Kaptari and Kämpfer [150]. The effective parameters for NN scattering have been taken similar to Ref. [167], however, the restoration of gauge invariance has been realized in a different way. As mentioned above, there are several prescriptions for restoring gauge invariance in effective theories including momentum-dependent form factors in interactions with charged hadrons [168] and the actual results depend on the prescription employed. The scheme in Ref. [150] is to include explicitly the vertex form factors into the Ward-Takahashi identity for the full meson-exchange propagators, which is different from the method used in Refs. [166, 167]. In this review we will report on results based on the bremsstrahlung calculations from Kaptari and Kämpfer in Ref. [150].

6. Results on photon production in $p + A$ and $A + A$ collisions

Direct photons are expected to provide a powerful probe of the quark-gluon plasma (QGP) as created in ultra-relativistic nuclear collisions. The photons interact only electromagnetically and thus escape to the detector almost undistorted through the dense and strongly interacting medium. Thus the photon transverse-momentum spectra and their azimuthal asymmetry carry information on the properties of the matter under extreme conditions, existing in the first few fm/c of the collisional evolution. On the other hand, the measured

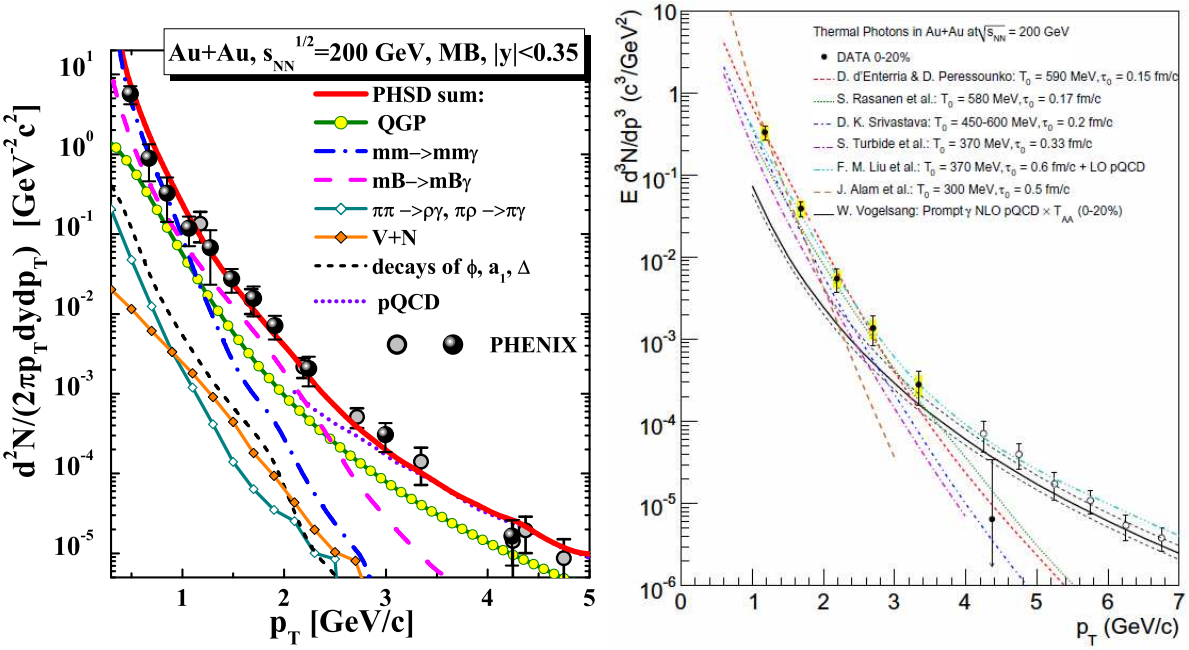


Figure 25: (l.h.s.) PHSD results for the spectrum of *direct* photons produced in 0-40% most central Au+Au collisions at $\sqrt{s_{NN}} = 200$ GeV as a function of the transverse momentum p_T at midrapidity $|y| < 0.35$. The data of the PHENIX Collaboration are adopted from Refs. [194, 195]. For the individual lines see the legend in the figure. The figure is taken from Ref. [102]. (r.h.s.) A compilation of various predictions for the *direct* photon yield in hydrodynamical models (see legend) in comparison to the data of the PHENIX collaboration. The figure is taken from Ref. [196].

photons provide a time-integrated picture of the heavy-ion collision dynamics and are emitted from every moving electric charge – partons or hadrons. Therefore, a multitude of photon sources has to be differentiated in order to access the signal of interest. The dominant contributions to the *inclusive* photon production are the decays of mesons, dominantly pions, η- and ω-mesons. Experimental collaborations subtract the "*decay* photons" from the inclusive photon spectrum using a cocktail calculation [172, 173] and obtain the "direct" photons.

In particular the *direct* photons at transverse momenta $p_T < 3$ GeV/c are expected to be dominated by "thermal" sources, i.e. the radiation from the strongly interacting Quark-Gluon-Plasma (sQGP) [174, 175] and the secondary meson+meson and meson+baryon interactions in the hadronic phase [138, 145]. These partonic and hadronic channels have been studied within PHSD in detail in Refs. [98, 101] at Relativistic-Heavy-Ion-Collider energies and it was found that the partonic channels constitute up to half of the observed *direct* photon spectrum for central collisions. Other theoretical calculations also find a significant or even dominant contribution of the photons produced in the QGP to the *direct* photon spectrum [176, 177, 178, 179, 180, 181].

The low-p_T *direct* photons probe not only the temperature [172, 173, 181] of the produced QCD-matter, but also its (transport) properties, for instance, the shear viscosity η (cf. Section 4.4). Using the *direct* photon elliptic flow v_2 (a measure of the azimuthal asymmetry in the photon distribution) as a viscosimeter was first suggested by Dusling in Ref. [182]; this idea was later supported by the calculations in Refs. [178, 179, 181, 183]. It was also suggested that the photon spectra and v_2 are sensitive to the collective directed flow of the system [184, 185], to the equation of state [184, 186], to the possible production of a Glasma [187, 188, 189], to the rate of chemical equilibration in the QGP [55, 60, 190] and to the asymmetry induced by the strong magnetic field (flash) in the very early stage of the heavy-ion collision [191, 192, 193].

However, the observation by the PHENIX Collaboration [172] that the elliptic flow $v_2(p_T)$ of *direct* photons produced in minimum bias Au+Au collisions at $\sqrt{s_{NN}} = 200$ GeV is comparable to that of the produced pions was a surprise and in contrast to the theoretical expectations and predictions. Indeed, the photons produced by partonic interactions in the quark-gluon plasma phase have not been expected to show considerable flow because they are dominated by the emission in the initial phase before the elliptic flow fully develops. We here report about the studies within the PHSD approach on this issue and compare to other models in context of the available data from the different collaborations.

6.1. Direct photon spectra from SPS to LHC energies

We start with the system p+Pb at 160 GeV, i.e. at the top SPS energy. Fig. 24 (l.h.s.) shows the comparison of the HSD/PHSD calculations to the data of the WA98 Collaboration from Ref. [170, 171] in the pseudorapidity interval $2.3 < \eta < 3.0$. In this case almost the entire photon spectrum is described by the contribution from pion and η decays while the contribution from the heavier mesons is not leading. The successful description of these data by PHSD is dominantly due to the fact that the meson production itself is described very well in p+A reactions [100].

We continue with Pb+Pb collisions at $\sqrt{s_{NN}} = 17.3$ GeV. Fig. 24 (r.h.s.) shows the comparison of the PHSD calculations [102] for the *direct* photon p_T-spectrum to the data of the WA98 Collaboration from Ref. [170, 171] for 10% centrality in the pseudorapidity interval $2.35 < \eta < 2.95$. In addition to the sources, which had been incorporated in the original HSD study in 2008, the meson+baryon bremsstrahlung, $VN \to N\gamma$, $\Delta \to N\gamma$ decay and the QGP channels are added. Compared to the earlier results of Ref. [100], the description of the data is further improved and the conclusions remain unchanged: the bremsstrahlung contributions are essential for describing the data at low p_T. This interpretation is shared by the authors of Refs. [130, 136, 197], who also stressed the importance of the meson+meson bremsstrahlung in view of the WA98 data using hydrodynamical or fireball models. Note that the photon contribution from the QGP is practically negligible at this bombarding energy for low p_T and reaches at most 25% at $p_T > 0.5$ GeV.

We now step on to the top RHIC energy of $\sqrt{s_{NN}} = 200$ GeV and report on PHSD results for the differential photon spectra for the system Au+Au. The *direct* photon spectrum – as a sum of partonic as well as hadronic sources – in 0-40% central Au+Au collisions is presented in Fig. 25 (l.h.s.) as a function of the transverse momentum p_T at midrapidity $|y| < 0.35$. While the 'hard' p_T spectra are dominated by the 'prompt' (pQCD) photons, the 'soft' spectra are filled by the 'thermal' sources: the QGP gives up to 50% of the *direct* photon yield below 2 GeV/c, a sizeable contribution stems from hadronic sources such as meson-meson (mm) and meson-Baryon (mB) bremsstrahlung while the contribution from binary mm reactions is of subleading order. Thus, according to the PHSD results the mm and mB bremsstrahlung turn out to be an important source of *direct* photons also at the top RHIC energy. We note, that the bremsstrahlung channels are not included in the mm binary 'HG' rate by Turbide et al. in Ref. [198] used in the hydro calculations addressed above. We stress that mm and mB bremsstrahlung can not be subtracted experimentally from the photon spectra and have to be included in theoretical models.

The right panel of Fig. 25 shows a compilation of various predictions for the *direct* photon yield in hydrodynamical models (see legend) in comparison to the data of the PHENIX collaboration from Ref. [196]. The NLO pQCD calculations for the prompt photon production from Vogelsang have been added to the *thermal* photon spectra. The actual results for the *direct* photon spectra depend on the initial temperature T_0 (varying by about a factor of 2) and the hydro starting time τ_0 which are fitted differently to final hadronic spectra, respectively. All these models only give a very low elliptic flow for the *direct* photons.

As an example for more recent calculations we show in Fig. 26 (l.h.s.) the results from the model of van Hees et al. [184] which is describing the PHENIX data [194] with a good accuracy. The calculations of Ref. [184] are based on a hydrodynamical model for the "fireball" evolution with the hypothesis that the rates of photon production are amplified for temperatures close to the hadronization transition and adding to the thermal spectra (calculated with the amplified rates) the photon contribution from final-state ω-mesons at thermal freeze-out. The spectra presented on the right hand side of Fig. 26 have been calculated by Shen et al. [181] using a viscous hydrodynamical evolution and taking into account viscous effects in the photon rates. In this approach – that reproduces the final hadron spectra and hadron v_2 – the data are underestimated considerably. The discrepancy becomes enhanced when an alternative scenario of a gluon-dominated initial state is considered since the gluons do not carry electric charge.

Photon sources: QGP vs. HG

The question: "what dominates the photon spectra - *QGP radiation or hadronic contributions*" can be addressed experimentally by investigating the centrality dependence of the photon yield since the QGP contribution is expected to decrease when going from central to peripheral collisions where the hadronic channels are dominant. Fig. 27 (l.h.s.) shows the centrality dependence of the *direct* photon p_T-spectra for 0-20%, 20-40%, 40-60%, 60-92% central Au+Au collisions at $\sqrt{s} = 200$ GeV. The solid dots stand for the recent PHENIX data [195, 199] whereas the lines indicate the model predictions: solid line - PHSD (denoted as 'Linnyk et al.') [98, 101, 102], dashed and dashed-dotted lines ('Shen et al. (KLN)' and 'Shen et al.' (MCGib)') are the

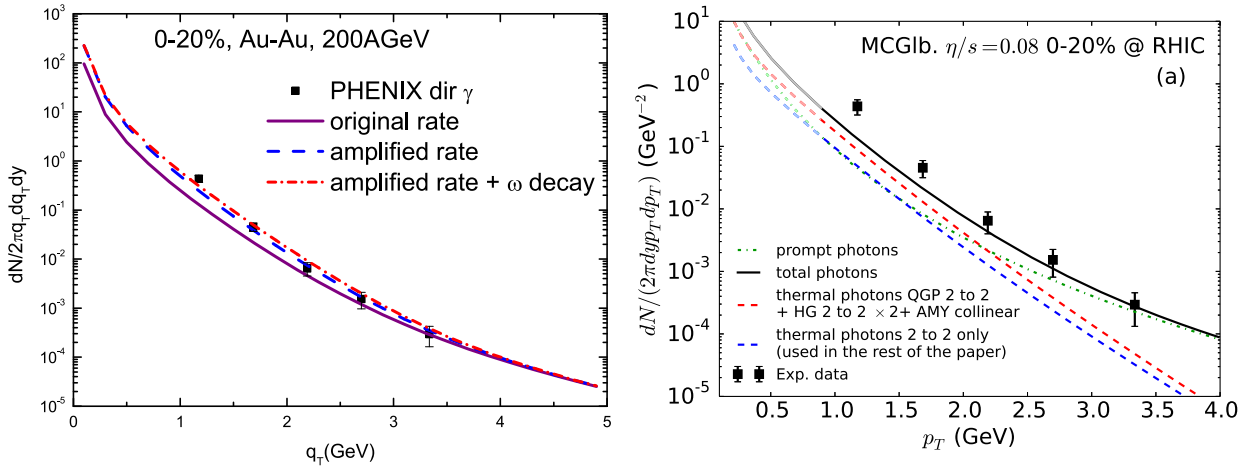


Figure 26: (l.h.s.) *Direct* photon spectra from the model of van Hees et al. [184] at RHIC when adding $\omega \to \pi^0 + \gamma$ decays at thermal freeze-out to a scenario with amplified rates at temperatures close to the pseudo-critical transition temperature T_c (dash-dotted line), compared to the amplified rate (dashed line) and default-rate (solid line) scenarios. The figure is taken from Ref.[184]. (r.h.s.) Calculated photon spectra in the viscous hydrodynamical model from Shen et al. [181] in comparison to the data from the PHENIX Collaboration [194].

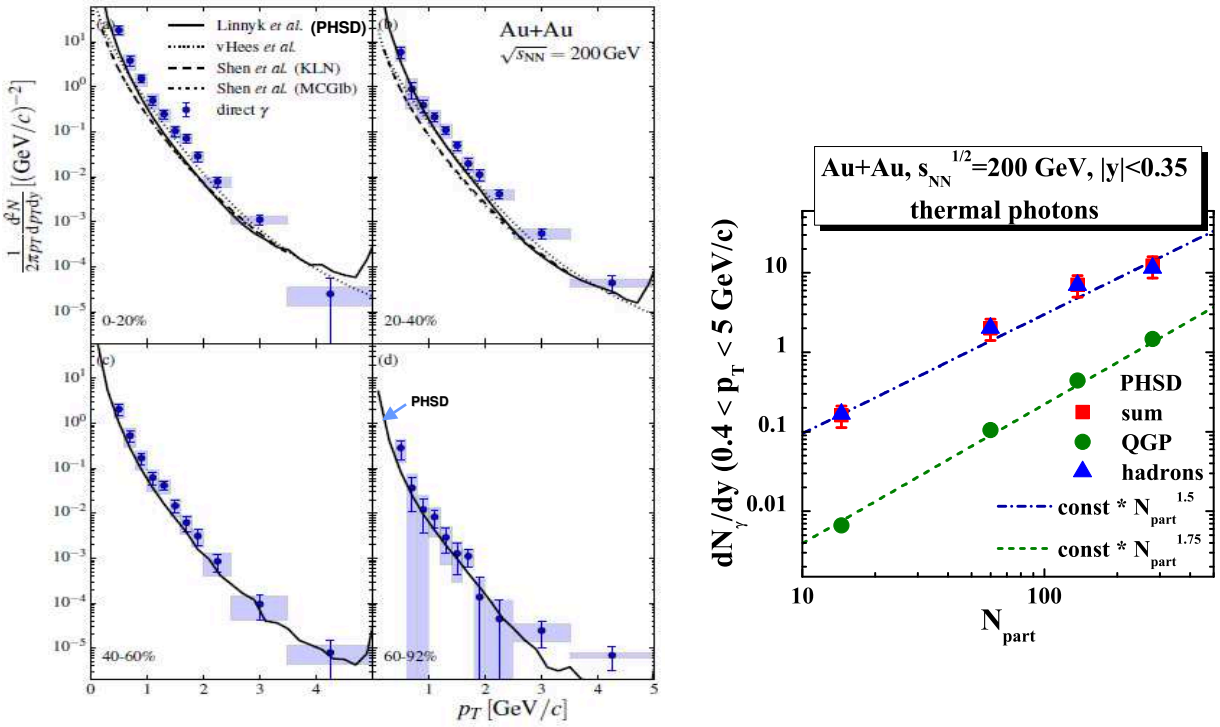


Figure 27: (*l.h.s*) Centrality dependence of the *direct* photon p_T-spectra for 0-20%, 20-40%, 40-60%, 60-92% central Au+Au collisions at $\sqrt{s}$ = 200 GeV: model predictions vs. the PHENIX data [195]. The PHSD predictions are denoted by 'Linnyk et al.' (solid lines). The figure is taken from Ref. [199]. (*r.h.s*) The scaling of the integrated *thermal* photon yield from PHSD as a function of the number of participating nucleons in Au+Au collisions at $\sqrt{s_{NN}}$ = 200 GeV for the hadronic channels (upper symbols) and partonic channels (lower symbols). The figure is taken from Ref. [101].

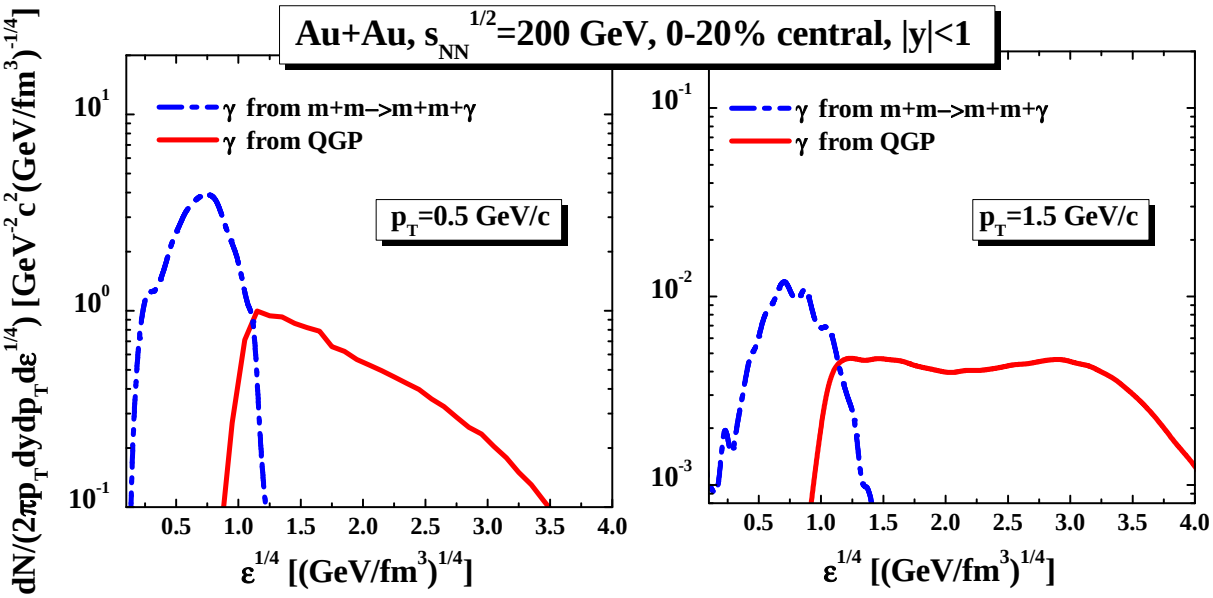


Figure 28: (l.h.s.) Photon yield with a transverse momentum $p_T = 0.5$ GeV/c at midrapidity produced in 0-20 % most central $Au + Au$ collisions as a function of the approximate local "temperature" (the fourth-root of the energy density) from the PHSD from meson-meson bremsstrahlung (dash-dotted lines) and gluon Compton scattering (solid lines). (r.h.s.) Same as in the left panel for photons with a transverse momentum $p_T = 1.5$ GeV/c.

results from viscous (2+1)D VISH2+1 [185] and (3+1)D MUSIC [178, 179] hydro models whereas the dotted line ('vHees et al.') stands for the results of the expanding fireball model [200]. As seen from Fig. 27 (l.h.s.) for the central collisions the models deviate up to a factor of 2 from the data and each other due to the different dynamics and sources included (as discussed above); for the (semi-)peripheral collisions the PHSD results - dominated by mm and mB bremsstrahlung - are consistent with the data which favor these hadronic sources. Presently, no results from the other models for peripheral reactions are known.

The centrality dependence of the *direct* photon yield, integrated over different p_T ranges, has been measured by the PHENIX Collaboration, too [195, 199]. It has been found that the midrapidity 'thermal' photon yield scales with the number of participants as $dN/dy \sim N_{part}^{\alpha}$ with $\alpha = 1.48 \pm 0.08$ and only very slightly depends on the selected p_T range (which is still in the 'soft' sector, i.e. < 1.4 GeV/c). Note that the 'prompt' photon contribution (which scales as the pp 'prompt' yield times the number of binary collisions in $A + A$) has been subtracted from the data. The PHSD predictions [98, 101, 102] for the minimum bias Au+Au collisions give $\alpha(total) \approx 1.5$ (cf. Fig. 27, r.h.s.) which is dominated by hadronic contributions while the QGP channels scale with $\alpha(QGP) \sim 1.75$. A similar finding has been obtained by the viscous (2+1)D VISH2+1 and (3+1)D MUSIC hydro models [181]: $\alpha(HG) \sim 1.46$, $\alpha(QGP) \sim 2$, $\alpha(total) \sim 1.7$. Thus, the QGP photons show a centrality dependence significantly stronger than that of hadron gas (HG) photons.

Next, let us investigate the photon production across the phase transition in the heavy-ion collision to check whether the observed yield of *direct* photons is produced dominantly in some particular region of the energy-density or in some particular phase of matter. Fig. 28 shows the yield of photons produced at midrapidity in 0-20 % most central $Au + Au$ collisions at $\sqrt{s_{NN}} = 200$ GeV as a function of the approximate local "temperature" (i.e. the fourth-root of the energy density) from the PHSD. The left panel of Fig. 28 presents the calculations for photons with a transverse momentum $p_T = 0.5$ GeV/c, while the right panel corresponds to photons with a transverse momentum $p_T = 1.5$ GeV/c. We observe that the early, hot state does not dominate the photon production in the QGP contrary to expectations of the static thermal fireball model, where photon production is roughly proportional to a power of the temperature ($\sim T^4$). The integration over the dynamical evolution of the heavy-ion collision leads to similar contributions of the different energy density regions for transverse momenta in the order of 1 – 1.5 GeV/c since the rate decreases but the space-time volume increases. For the low p_T=0.5 GeV/c, i.e. at the lower end of the experimental spectra, the hadronic contribution is clearly larger than the partonic one. The photon production in the hadronic phase is dominated by the lower energies/temperatures

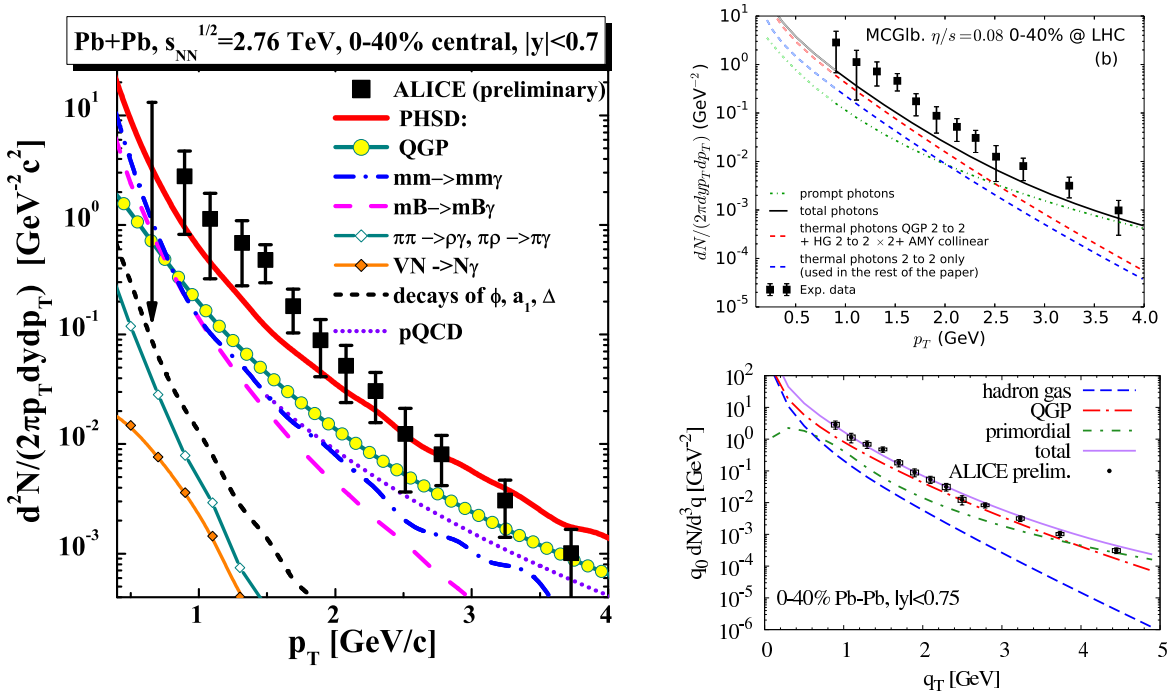


Figure 29: (l.h.s.) The yield of *direct* photons at midrapidity in Pb+Pb collisions at the invariant energy $\sqrt{s_{NN}}$ = 2.76 TeV for 0-40% centrality as predicted within the PHSD in comparison to the preliminary data from the ALICE Collaboration [173]. The figure is taken from Ref. [102]. (r.h.s., upper panel:) Photon spectra in 0−40% centrality Pb+Pb collisions at the LHC as calculated within the viscous hydrodynamics by Shen et al. [183]. The Pb+Pb data are from the ALICE Collaboration [173]. The figure is taken from Ref. [183]. (r.h.s., lower panel:) The same observable as calculated in the upper panel with an ideal hydrodynamical evolution and amplified photon rates around the transition temperature by van Hees et al. [184]. The figure is taken from Ref. [184].

because of the very long times over which the produced hadrons continue to interact elastically, which is accompanied by the photon bremsstrahlung in case of charged hadrons.

We now increase the invariant collision energy $\sqrt{s_{NN}}$ by a factor of 13.8. In Fig. 29 (l.h.s.) we show the *direct* photon yield from PHSD in Pb+Pb collisions at the invariant energy $\sqrt{s_{NN}}$ = 2.76 TeV for 0-40% centrality in comparison to the preliminary data of the ALICE Collaboration from Ref. [173]. We find a rather good overall agreement with the data within about a factor of 2 in the range of transverse momenta p_T from 1 to 4 GeV. On the other hand, the calculations tend to underestimate the preliminary data in the low-p_T region [202]. However, the significance of the comparison is not robust until the final data will be available. We, furthermore, present in Fig. 29 (r.h.s.) the photon spectra for 0−40% centrality Pb+Pb collisions at the LHC as calculated within the viscous hydrodynamics by Shen et al. [183] in comparison to the Pb+Pb data from the ALICE Collaboration [173] (upper right panel). In the right bottom panel we show the same observable as calculated in the ideal hydrodynamical model with amplified photon rates around the transition temperature by van Hees et al. [184]. Similar to RHIC energies the viscous hydro calculations [183] underestimate the measured photon yield for $p_T < 2$ GeV/c while the model of van Hees et al. [184] with amplified rates at T_c performs better.

An actual overview on the current situation with respect to the *direct* photon yields at different centralities has been provided by the ALICE Collaboration in Ref. [201] and is displayed in Fig. 30. The figure shows the centrality dependence of the *direct* photon p_T-spectra for 0-20%, 20-40%, 40-80% central Pb+Pb collisions at $\sqrt{s_{NN}}$=2.76 TeV in comparison to various model predictions. The PHSD predictions are denoted by 'Linnyk et al.' (dotted lines) and are compatible with the measurements within the error bars. This roughly holds also for the other models.

In conclusion, we have found that from SPS to LHC energies the radiation from the sQGP constitutes less than half of the observed number of *direct* photons for central reactions in the PHSD. The hydrodynamical and fireball models predict a larger fraction of the QGP photons to the total yield and are substantially lower in the hadronic contributions. The radiation from hadrons and their interaction – which are not measured separately

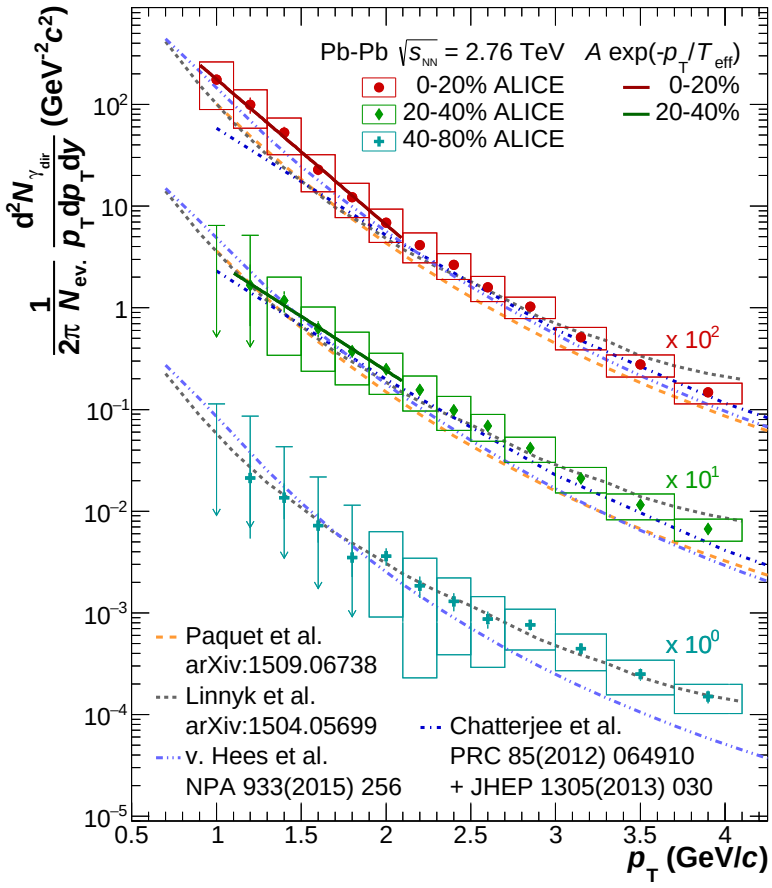


Figure 30: Centrality dependence of the *direct* photon p_T-spectra for 0-20%, 20-40%, 40-80% central Pb+Pb collisions at $\sqrt{s_{NN}}$=2.76 TeV: model predictions vs. the ALICE data [201]. The PHSD predictions are denoted by 'Linnyk et al.' (dotted lines). The figure is taken from Ref. [201].

so far – give a considerable contribution in the PHSD especially at low transverse momentum. The dominant hadronic sources are the meson decays, the meson-meson bremsstrahlung and the meson-baryon bremsstrahlung. While the first (e.g. the decays of ω, η', ϕ and a_1 mesons) can be subtracted from the photon spectra once the mesonic yields are determined independently by experiment, the reactions $\pi + \rho \to \pi + \gamma$, $\pi + \pi \to \rho + \gamma$, $V + N \to N + \gamma$, $\Delta \to N + \gamma$ as well as the meson-meson and meson-baryon bremsstrahlung can be 'separated' from the partonic sources only with the assistance of theoretical models (and corresponding uncertainties).

6.2. Elliptic flow of direct *photons*

We recall that the azimuthal momentum distribution of the photons is expressed in the form of a Fourier series as,

$$E\frac{d^3N}{d^3p} = \frac{d^2N}{2\pi p_T dp_T dy}\left(1+\sum_{n=1}^{\infty} 2v_n(p_T)\cos[n(\psi-\Psi_n)]\right), \tag{167}$$

where v_n is the magnitude of the n'th order harmonic term relative to the angle of the initial-state fluctuating spatial plane of symmetry Ψ_n and $p = (E, \vec{p})$ is the four-momentum of the photon. We here focus on the coefficients v_2 and v_3 which implies that we have to perform event by event calculations in order to catch the initial fluctuations in the shape of the interaction zone and the event plane Ψ_{EP}. We calculate the triangular flow v_3 with respect to Ψ_3 as $v_3\{\Psi_3\} = \langle\cos(3[\psi - \Psi_3])\rangle/\mathrm{Res}(\Psi_3)$. The event plane angle Ψ_3 and its resolution $\mathrm{Res}(\Psi_3)$ are evaluated as described in Ref. [83] via hadron-hadron correlations by the two-sub-events method [84, 85].

We note again that the second flow coefficient v_2 carries information on the interaction strength in the system – and thus on the state of matter and its properties – at the space-time point, from which the measured

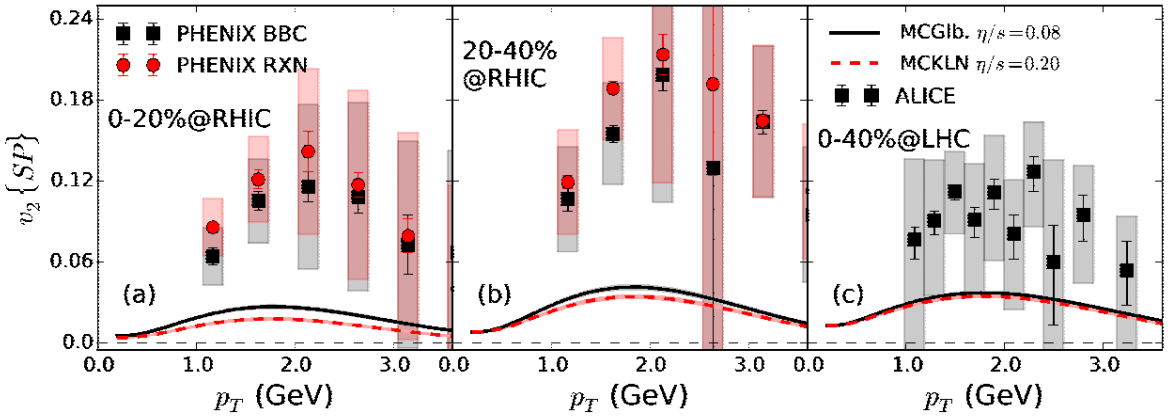


Figure 31: Comparison of *direct* photon (prompt + thermal (QGP+HG)) elliptic flow from event-by-event viscous hydrodynamics with recent experimental data from (a) 0-20% and (b) 20-40% central Au+Au collisions at RHIC [172] and (c) from 0-40% central Pb+Pb collisions at the LHC [204]. The solid black (dashed red) lines correspond to MCGlb (MCKLN) initial conditions evolved with a shear viscosity $\eta/s = 0.08$ (0.2), respectively. The figure is taken from Ref. [183].

particles are emitted. The elliptic flow v_2 reflects the azimuthal asymmetry in the momentum distribution of the produced particles (p_x vs p_y), which is correlated with the geometrical azimuthal asymmetry of the initial reaction region. If the produced system is a weakly-interacting gas, then the initial spatial asymmetry is not effectively transferred into the final distribution of the momenta. On the other hand, if the produced matter has the properties of a liquid, then the initial geometrical configuration is reflected in the final particle momentum distribution.

More than a decade ago, the WA98 Collaboration has measured the elliptic flow v_2 of photons produced in $Pb + Pb$ collisions at the beam energy of $E_{beam} = 158$ AGeV [203], and it was found that the $v_2(\gamma^{incl})$ of the low-transverse-momentum inclusive photons was about equal to the $v_2(\pi)$ of pions within the experimental uncertainties. This observation lead to the conclusion that either (Scenario a:) the contribution of the *direct* photons to the inclusive ones is negligible in comparison to the *decay* photons, i.e. dominantly the π^0 decay products, or (Scenario 2:) the elliptic flow of the *direct* photons is comparable in magnitude to the $v_2(\gamma^{incl})$, $v_2(\gamma^{decay})$ and $v_2(\pi)$. However, in view of the *direct* photon spectrum from WA98, which we described in Section 6.1, there is a significant finite yield of *direct* photons at low transverse momentum. Thus the scenario 1 can be ruled out. Furthermore, the observed *direct* photons of low p_T must have a significant elliptic anisotropy v_2 of the same order of magnitude as the hadronic flow since they dominantly stem from hadronic sources. Thus the interpretation [100, 130] of the low-p_T *direct* photon yield measured by WA98 – as dominantly produced by the bremsstrahlung process in the mesonic collisions $\pi + \pi \to \pi + \pi + \gamma$ – is in accord also with the data on the photon elliptic flow $v_2(\gamma^{incl})$ at the top SPS energy.

Let us note that the same conclusions apply also to the most recent studies of the photon elliptic flow at RHIC and LHC. The PHENIX and ALICE Collaborations have measured the inclusive photon v_2 and found that at low transverse momenta it is comparable to the $v_2(p_T)$ of *decay* photons as calculated in cocktail simulations based on the known mesonic $v_2(p_T)$. Therefore, either (a) the yield of the *direct* photons to the inclusive ones is not statistically significant in comparison to the *decay* photons or (b) the elliptic flow of the *direct* photons must be as large as $v_2(\gamma^{decay})$ and $v_2(\gamma^{incl})$.

The direct photon v_2 "puzzle"

The recent observation by the PHENIX Collaboration [172] that the elliptic flow $v_2(p_T)$ of *direct* photons produced in minimum bias Au+Au collisions at $\sqrt{s_{NN}} = 200$ GeV is comparable to that of the produced pions was a surprise and in contrast to the theoretical expectations and predictions [176, 177, 178, 179, 180]. Indeed, the photons produced by partonic interactions in the quark-gluon plasma phase have not been expected to show a considerable flow because - in a hydrodynamical picture - they are dominated by the emission at high temperatures, i.e. in the initial phase before the elliptic flow fully develops. Since the *direct* photon $v_2(\gamma^{dir})$ is

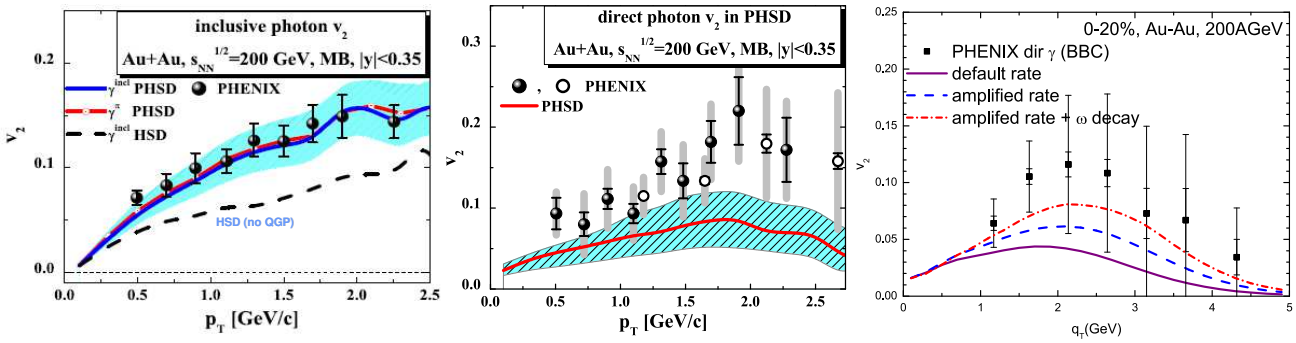


Figure 32: *Inclusive* (left) and *direct* (middle) photon elliptic flow coefficient $v_2(p_T)$ from the PHSD approach in comparison to the PHENIX data [172] for midrapidity minimum bias Au+Au collisions at $\sqrt{s} = 200$ GeV. The figures are taken from Ref. [98, 101, 102]. (r.h.s.) *Direct* photon spectra v_2 from the fireball model at RHIC when adding $\omega \to \pi^0 + \gamma$ decays at thermal freeze-out to the scenario with amplified rates (dash-dotted line), compared to the amplified-rate (dashed line) and default-rate (solid line) scenarios. The figure is taken from Ref.[184].

a 'weighted average' (w_i) of the elliptic flow of individual contributions i,

$$v_2(\gamma^{dir}) = \sum_i v_2(\gamma^i) w_i(p_T) = \frac{\sum_i v_2(\gamma^i) N_i(p_T)}{\sum_i N_i(p_T)}, \tag{168}$$

a large QGP contribution gives a smaller $v_2(\gamma^{dir})$.

A sizable photon v_2 has been observed also by the ALICE Collaboration [173, 204] at the LHC. None of the theoretical models could describe simultaneously the photon spectra and v_2 which may be noted as a "puzzle" for theory (cf. Fig. 31 in case of viscuous hydro calculations by Shen et al. in Ref. [183]). Moreover, the PHENIX and ALICE Collaborations have reported recently the observation of non-zero triangular flow v_3 (see Refs. [205, 206]). Thus, the consistent description of the photon experimental data remains a challenge for theory and has stimulated a couple of new ideas and developments that are briefly outlined in the following.

Developments in hydrodynamical models

The following developments in the hydrodynamical modeling of the heavy-ion collision evolution and the photon rates were stimulated by the puzzling disagreement between the models and the photon data (cf. Fig. 31).

I.) The first hydrodynamical calculations on photon spectra were based on ideal hydrodynamics with smooth Glauber-type initial conditions (cf. Ref. [112]). The influence of *event-by-event (e-b-e) fluctuating initial conditions* on the photon observables was investigated within the (2+1)D Jyväskylä ideal hydro model [180] which includes the equilibrated QGP and Hadron Gas (HG) fluids. It has been shown that 'bumpy' initial conditions based on the Monte-Carlo Glauber model lead to a slight increase at high p_T (> 3 GeV/c) for the yield and v_2 which is, however, not sufficient to explain the experimental data – see the comparison of model calculations with the PHENIX data in Figs. 7,8 of Ref. [180] and with the ALICE data in Figs. 9,10 of Ref. [180].

II.) The influence of *viscous corrections* on photon spectra and anisotropic flow coefficients v_n has been investigated in two independent viscous hydro models: 1) (3+1)D MUSIC [178, 179] which is based on "bumpy" e-b-e fluctuating initial conditions from IP-Glasma and includes viscous QGP (with lQCD EoS) and HG fluids; 2) (2+1)D VISH2+1 [185] with 'bumpy' e-b-e fluctuating initial conditions from the Monte-Carlo Glauber model and viscous QGP (with lQCD EoS) and HG fluids. The photon rate has been modified in Refs. [178, 179, 185] in order to account for first order non-equilibrium (viscous) corrections to the standard equilibrium rates (i.e. the thermal QGP [99] and HG [198] rates). It has been found that the viscous corrections only slightly increase the high p_T spectra compared to the ideal hydro calculations while they have a large effect on the anisotropic flow coefficients v_n. Interesting to note that the viscous suppression of hydrodynamic flow for photons is much stronger than for hadrons. Also the photon v_n coefficients are more sensitive to the QGP shear viscosity which might serve the photon flow observables as a *QGP viscometer* as suggested in Ref. [185].

It is important to stress that the state-of-art hydro models discussed above reproduce well the hadronic 'bulk' observables (e.g. rapidity distributions, p_T spectra and v_2, v_3 of hadrons). However, in spite of definite

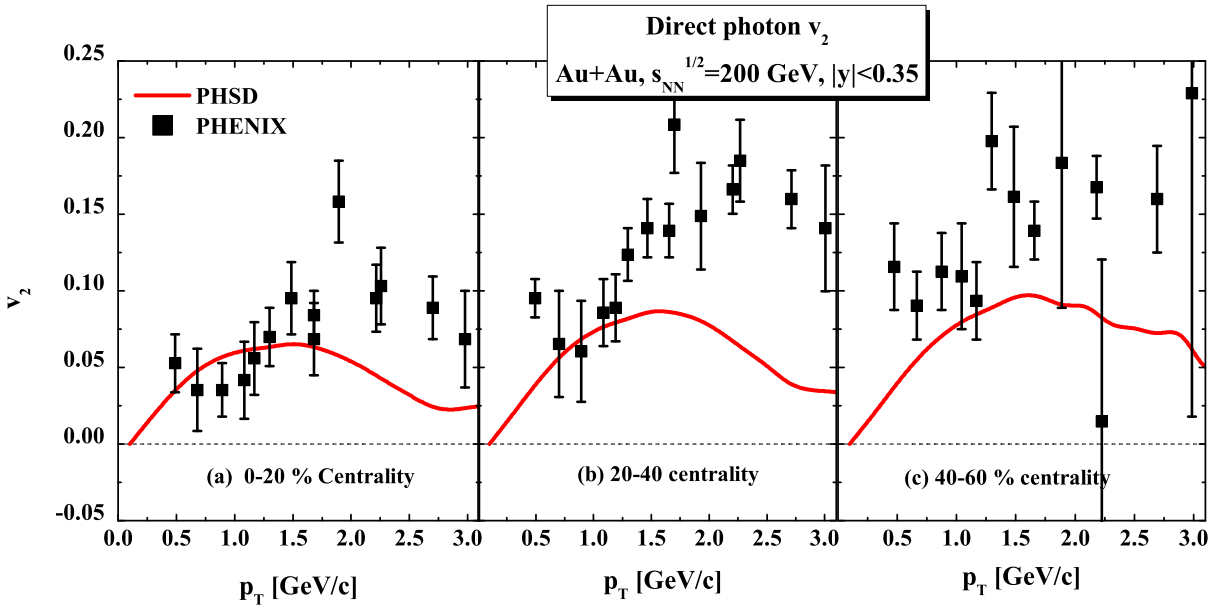


Figure 33: Centrality dependence of the *direct* photon v_2 for Au+Au collisions at $\sqrt{s_{NN}} = 200$ GeV for different centralities (see legend); the data from the PHENIX Collaboration [195, 208] are compared to the earlier PHSD predictions from Ref. [101].

improvements of the general dynamics by including the fluctuating initial conditions (IP-Glasma or MC-Glauber type) and viscous effects, the hydro models underestimate the spectra and v_2 of photons at RHIC and LHC energies.

III.) Another idea, which has been checked recently within the (2+1)D VISH2+1 viscous hydro model by Shen et al. [185], corresponds to the generation of *'pre-equilibrium' flow* (see Ref. [207]). The idea of 'initial' flow has been suggested in Ref. [200] and modeled as a rapid increase of bulk v_2 in the expanding fireball model which leads to a substantial enhancement of photon v_2. In a viscous hydro model [207] the generation of pre-equilibrium flow has been realized using a free-streaming model to evolve the partons to 0.6 fm/c where the Landau matching takes over to switch to viscous hydro. Such a scenario leads to a quick development of momentum anisotropy with saturation near the critical temperature T_c. Although the pre-equilibrium flow effect increases the photon v_2 slightly this is not sufficient to reproduce the ALICE data (the same holds for the PHENIX data at RHIC energies). Note, that the actual strength of such an effect depends on the way of its modeling (cf. Ref. [200]). Moreover, the physical origin of such 'initial' (pre-equilibrium) flow has to be justified/found first before robust conclusions can be drown.

One may speculate about the possible effects on photon observables from further improvements of hydro models such as an inclusion of the finite bulk viscosity as well as other transport coefficients and their temperature dependence etc. However, the failure of the state-of-art viscous hydro models to describe the photon observables is striking although the hadronic 'bulk' dynamics is well reproduced.

Photons from non-equilibrium transport

In order to shed some light on the photon v_2 puzzle outlined above, we consider the influence of *non-equilibrium dynamics* on the photon production in the following. As a 'laboratory' for that we will employ the microscopic PHSD transport approach that has been derived and described in Sections 2-4, while the implementation of photon production by the various partonic and hadronic channels has been explained in Section 5. Since the elliptic flow of pions (or charged hadrons) is under control in PHSD in comparison to the data from the PHENIX, STAR and ALICE Collaborations (cf. Refs. [67, 98, 172, 209, 210]); also the spectrum of their *decay* photons is predicted reliably by the approach. This allows for a solid computation of the *direct* photon yield at all energies from SPS to LHC.

In the PHSD the *direct* photon $v_2(\gamma^{dir})$ is calculating by building the weighted sum of the channels, which are not subtracted by the data-driven methods, as follows: the photons from the quark-gluon plasma, from the initial hard parton collisions (pQCD photons), from the decays of short-living resonances (a_1-meson, ϕ-meson,

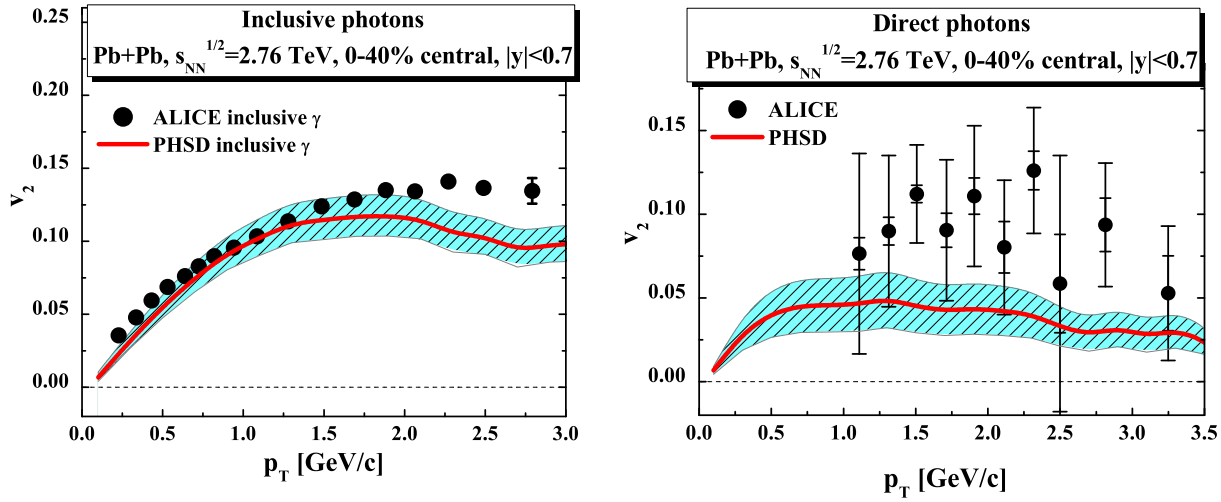


Figure 34: (l.h.s.) Elliptic flow v_2 versus transverse momentum p_T for the *inclusive* photons produced in 0-40% central Pb+Pb collisions at $\sqrt{s_{NN}} = 2.76$ TeV as calculated by the PHSD (solid red line); the blue error band reflects the finite statistics and the uncertainty in the modeling of the cross sections for the individual channels. (r.h.s.) Elliptic flow v_2 versus transverse momentum p_T for the *direct* photons produced in 0-40% central Pb+Pb collisions at $\sqrt{s_{NN}} = 2.76$ TeV as predicted by the PHSD (solid red line); the blue error band is dominated by the uncertainty in the modeling of the cross sections for the individual channels. The data from the ALICE Collaboration are taken from Ref. [211].

Δ-baryon), from the binary meson+meson and meson+baryon channels ($\pi + \rho \to \pi + \gamma$, $\pi + \pi \to \rho + \gamma$, $V + p/n \to n/p + \gamma$), and from the bremsstrahlung in the elastic meson+meson and meson+baryon collisions ($m + m \to m + m + \gamma$, $m + B \to m + B + \gamma$). The *direct* photon v_2 is extracted by summing up the elliptic flow of the individual channels contributing to the *direct* photons, using their contributions to the spectrum as the relative p_T-dependent weights, $w_i(p_T)$, cf. Eq. 168.

The results for the elliptic flow $v_2(p_T)$ of *direct photons* produced in Au+Au collisions at the top RHIC energy are shown in the middle panel of Fig. 32 while the elliptic flow in the left panel in comparison to the PHENIX data [172]. Since the inclusive photons dominantly stem from π^0 decay the left panel of Fig. 32 demonstrates again that the pion v_2 is under control in PHSD while HSD calculations (dashed line) fail substantially. According to the PHSD calculations for the *direct* photon spectra almost half of the *direct* photons measured by PHENIX (in central collisions) stems from the collisions of quarks and gluons in the deconfined medium created in the initial phase of the collision. The photons produced in the QGP carry a very small v_2 and lead to an overall *direct* photon v_2 about a factor of 2 below the pion $v_2(\pi)$ even though the other channels in the sum (168) have large elliptic flow coefficients v_2 of the order of $v_2(\pi)$ (cf. Fig. 7 of Ref. [98]). This leads to a final elliptic flow for *direct* photons which is about half of the measured v_2 in PHSD. The right panel of Fig. 32 shows the photon v_2 from the fireball model of van Hees et al. [184] for different scenarios: the solid line corresponds to the 'default scenario', which is comparable to the PHSD results for v_2 (middle panel). The dashed line is obtained when amplifying the production rate close to T_c while the dash-dotted line additionally includes the photons from ω-decay at freeze-out. We note that in PHSD we do not find an enhanced photon rate close to T_c (cf. Fig. 27) and the ω-decay contributions are included by default. In summary, we conclude that the PHSD results lead to a *direct* photon v_2 at RHIC which is substantially larger that that from hydro calculations (cf. Fig. 29) but still underestimates the PHENIX data at RHIC.

The PHSD results are readily understood as follows: the partonic collisions – producing photons in the QGP – take place throughout the evolution of the collision. The initial high partonic collision rate falls rapidly with time in PHSD and is followed up by a significant amount of hadronic production channels. Thus the production of photons from the QGP is no longer dominated by the early times. As a consequence, the elliptic flow 'picked up' by the photons from the parent parton collisions saturates after about 5 fm/c and reaches a relatively low value of about 0.02, only. We note that a delayed production of charges from the strong gluon fields ('glasma' [214, 215, 216, 217]) might shift the QGP photon production to somewhat later times when the elliptic flow is built up more but this also decreases the amount of QGP photons! However, we cannot quantitatively answer whether the additional evolution in the pre-plasma state could generate considerable

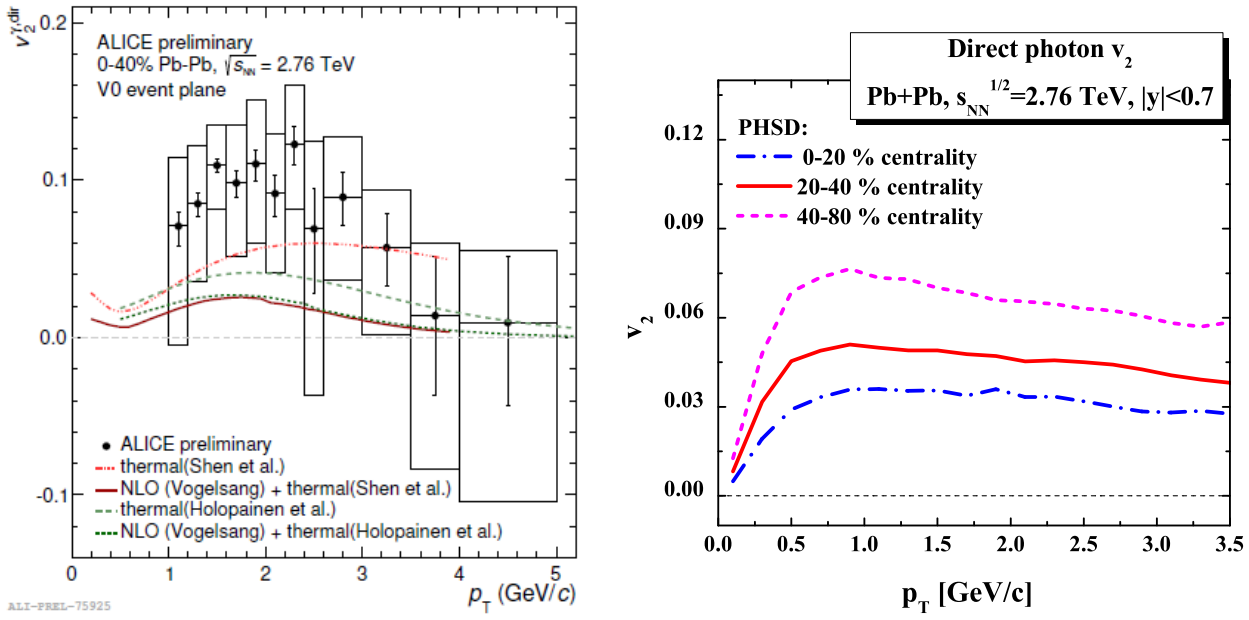


Figure 35: (l.h.s.) Preliminary data of the ALICE Collaboration for the *direct* photon elliptic flow v_2 in comparison to theoretical calculations from Refs. [183, 212, 213]. The figure is taken from Ref. [211]. (r.h.s.) Predictions for the elliptic flow v_2 of *direct* photons from PHSD versus transverse momentum p_T produced in Pb+Pb collisions at $\sqrt{s_{NN}} = 2.76$ TeV for different centrality classes (see legend).

additional v_2 while reproducing the photon spectra.

A preliminary summary of the current situation is displayed in Fig. 33 where the photon elliptic flow from PHENIX is compared to the PHSD predictions for different centrality classes 0-20% (a), 20-40% (b) and 40-60% (c). Whereas the elliptic flow is roughly described in the most central class there is an increasing tendency to underestimate in the PHSD the strong elliptic flow especially for peripheral collisions where some additional source might be present. Thus the observed centrality dependence of the elliptic flow is roughly in agreement with the interpretation that a large fraction of the *direct* photons is of hadronic origin (in particular from the bremsstrahlung in meson+meson and meson+baryon collisions); the latter contribution becomes stronger or even dominant in more peripheral collisions. But more precise data will be mandatory for a robust conclusion.

We finally present the PHSD predictions/calculations for the elliptic flow of inclusive and *direct* photons produced in $Pb + Pb$ collisions at the energy of $\sqrt{s_{NN}} = 2.76$ TeV at the LHC within the acceptance of the ALICE detector. Since the pion v_2 is described well within the PHSD at $\sqrt{s_{NN}} = 2.76$ TeV this is expected also for the inclusive photon v_2 due to the dominance of photons from π^0 decay. The left panel of Fig. 34 presents predictions/calculations for the elliptic flow v_2 versus transverse momentum p_T for the *inclusive* photons produced in 0-40% central Pb+Pb collisions at $\sqrt{s_{NN}} = 2.76$ TeV (solid red line) with the blue error band reflecting the finite statistics and the theoretical uncertainty in the modeling of the cross sections for the individual channels. The elliptic flow $v_2(p_T)$ of *direct* photons produced in 0-40% central Pb+Pb collisions at $\sqrt{s_{NN}} = 2.76$ TeV as predicted by the PHSD (solid red line) is shown in the right panel of Fig. 34, the blue error band is dominated by the uncertainty in the modeling of the cross sections for the individual channels. As in case of the PHENIX data at RHIC the preliminary data of the ALICE Collaboration for the *direct* photon elliptic flow v_2 for the same centrality are slightly higher than the PHSD predictions (although compatible within error bars). The different lines in Fig. 35 (l.h.s.) show the *direct* photon $v_2(p_T)$ from the theoretical calculations in Refs. [183, 212, 213] (see legend) which are similar to the PHSD predictions or even below. The situation at the LHC energy of $\sqrt{s_{NN}} = 2.76$ TeV is thus comparable to the one at the top RHIC energy and the v_2 puzzle remains.

We, furthermore, provide predictions for the centrality dependence of the *direct* photon $v_2(p_T)$ in Pb+Pb collisions at $\sqrt{s_{NN}} = 2.76$ TeV in the centrality classes 0-20%, 20-40% and 40-80% which are of relevance for the upcoming measurements by the ALICE Collaboration at the LHC. The actual results from PHSD are displayed in Fig. 35 (r.h.s.) and show a very similar centrality dependence as in case of Au+Au collisions at the top

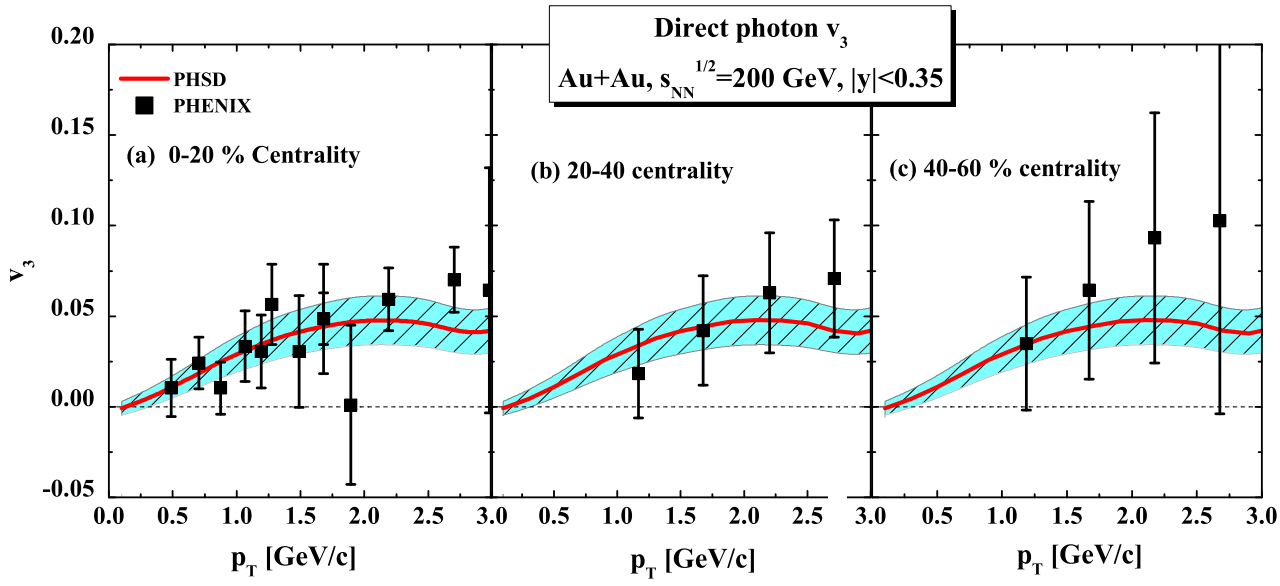


Figure 36: (Color on-line) Triangular flow v_3 versus transverse momentum p_T for the *direct* photons produced in Au+Au collisions at $\sqrt{s_{NN}} = 200$ GeV in three centrality classes (see legends). The PHSD results are shown by the solid red lines in comparison to the data of the PHENIX Collaboration (black symbols) taken from Ref. [221, 208].

RHIC energy.

We note that there are other scenarios towards the solution of the *direct* photon v_2 puzzle proposed during the 'Quark Matter-2014 Conference': early-time magnetic field effects [218, 219], Glasma effects [187], or non-perturbative effects of a 'semi-QGP' [220]. We discard an explicit discussion of these suggestions.

6.3. Triangular flow of direct photons

We have seen in the previous Subsections that the measured spectra of *direct* photons could be reproduced by the PHSD calculations at least within a factor of 2 (which is comparable with the current accuracy of the measurements). Also, the *inclusive* photon v_2 was well described and the elliptic flow of *direct* photons was qualitatively in line with the data and attributed essentially to hadronic sources although still underestimating the data.

On the other hand, there exists an alternative interpretation of the strong elliptic flow of *direct* photons, in which the azimuthal asymmetry of the photons is due to the initial strong magnetic field essentially produced by spectator charges (protons). Indeed, the magnetic field strength in the very early reaction stage reaches up to $eB_y \approx 5m_\pi^2$ in semi-peripheral $Au+Au$ collisions at $\sqrt{s_{NN}} = 200$ GeV (see the calculations within the PHSD in Ref. [222]; comparable estimates have been obtained also in Refs. [192, 193, 223]). These strong magnetic fields might influence the photon production via the polarization of the medium, e.g. by influencing the motion of charged quarks in the QGP, or by directly inducing a real photon radiation via the virtual photon ($\vec{B}$-field) coupling to a quark loop and (multiple) gluons; the photons are then produced azimuthal asymmetrically with positive v_2.

The photon production under the influence of magnetic fields has been calculated in Refs. [187, 191, 192, 193, 218, 224]. The observed spectra and elliptic flow of *direct* photons could be explained using suitable assumptions on the conductivity, bulk viscosity or degree of chemical equilibration in the early produced matter. The common feature of these calculations was that the *triangular* flow coefficient v_3 of the *direct* photons was expected to be very small. Indeed, the magnetic field may lead to an azimuthal asymmetry v_2 but not to a triangular mode v_3.

Consequently, it is of interest to measure experimentally the third flow coefficient $v_3(p_T)$ and to compare it to the calculations in the different classes of models: (a) those attributing the large elliptic flow and strong yield of *direct* photons dominantly to hadronic sources, e.g. the PHSD transport approach; (b) the models suggesting the large azimuthal asymmetry and additional yield of *direct* photons to be caused by the early magnetic fields; (c) the models assuming that the yield of *direct* photons at low p_T is dominated by partonic channels.

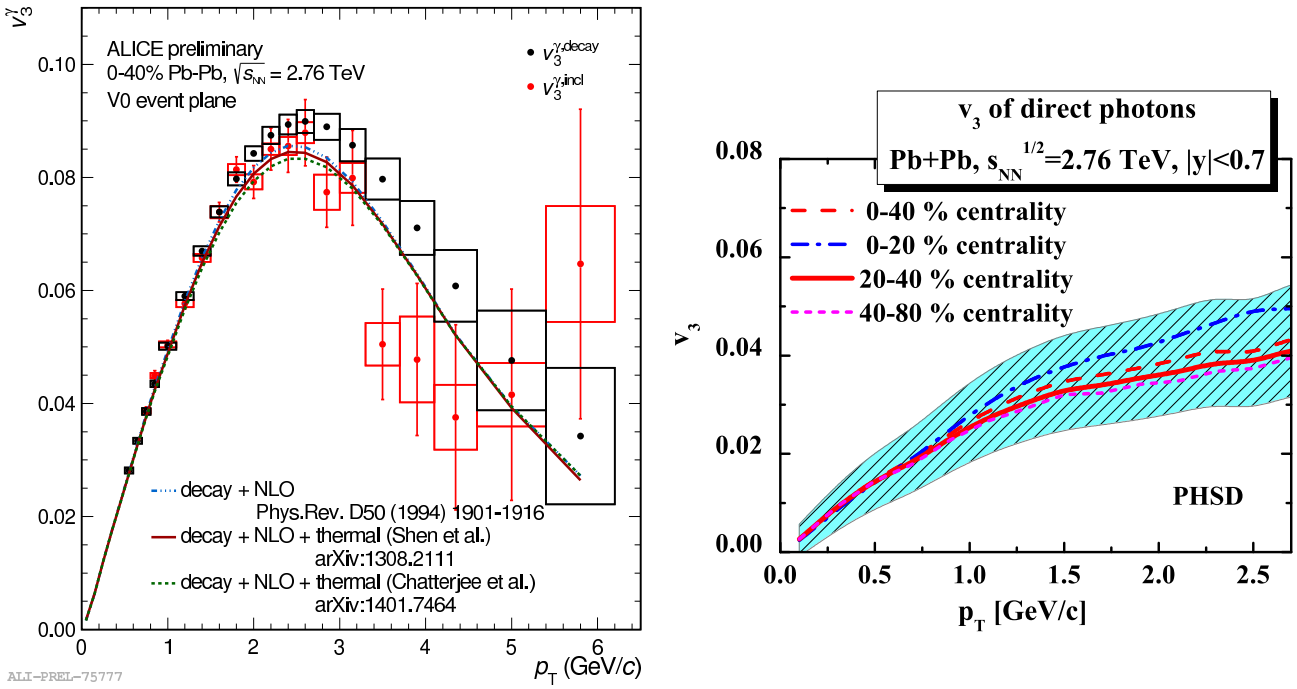


Figure 37: (l.h.s.) Preliminary data of the ALICE Collaboration for the inclusive photon $v_3(p_T)$. The lines represent contributions of *decay* photons with added theoretical calculations from Refs. [183, 212, 213]. The figure is taken from Ref. [225]. (r.h.s.) Predictions for the triangular flow v_3 versus transverse momentum p_T for the *direct* photons produced in different centrality classes for Pb+Pb collisions at $\sqrt{s_{NN}} = 2.76$ TeV from the PHSD (see legend); the blue band reflects the uncertainty in the modeling of the cross sections for the individual channels and give a measure of the present level of accuracy. The figure is taken from Ref. [102].

In Fig. 36 we present our results for the triangular flow v_3 versus transverse momentum p_T for the *direct* photons produced in Au+Au collisions at $\sqrt{s_{NN}} = 200$ GeV from the PHSD (solid red lines) for 0-20% (a), 20-40% (b) and 40-60% (c) centrality. The PHSD gives a positive non-zero triangular flow of *direct* photons up to 6% with very little centrality dependence on the level of the present accuracy ($\sim 25\%$). The PHSD results are in agreement with the data of the PHENIX Collaboration from Refs. [199, 205, 221] which suggests that the scenario (a) is at least compatible with the measurements.

The preliminary data of the ALICE Collaboration for the v_3 of inclusive photons in Fig. 37 (l.h.s.) do not seem to point towards an interpretation of the *direct* photons being dominantly produced in the early stage under the influence of the magnetic field (b), because the v_3 of these photons is expected to be close to zero. Of course, the photon production in the magnetic fields occurs on top of other channels, which may carry finite triangular flow v_3. But the weighted sum of all the channels including the magnetic-field-induced photons will give a smaller $v_3 \neq 0$ than the sum without this channel. The scenario (c) has been studied by other groups within a hydrodynamic modeling of the collision in Refs. [183, 226]. The triangular flow $v_3(p_T)$ of *direct* photons from Refs. [183, 226] is about a factor of 2 smaller than that obtained in the PHSD approach.

In Fig. 37 (r.h.s.) we present predictions for the triangular flow v_3 versus transverse momentum p_T for the *direct* photons produced in different centrality classes for Pb+Pb collisions at $\sqrt{s_{NN}} = 2.76$ TeV from the PHSD (see legend); the blue band reflects the uncertainty in the modeling of the cross sections for the individual channels and give a measure of the present level of accuracy. The centrality dependence of $v_3(p_T)$ turns out to be low and is practically constant within the accuracy of the present PHSD calculations. An experimental confirmation of this expectation could further affirm the notion of large hadronic contributions to the *direct* photons and in particular the photon production via the bremsstrahlung in meson and baryon collisions. It should be possible to differentiate between the scenarios in the future, when data of higher accuracy and information on the centrality dependence of *direct* photons (especially on v_2 and v_3) will become available.

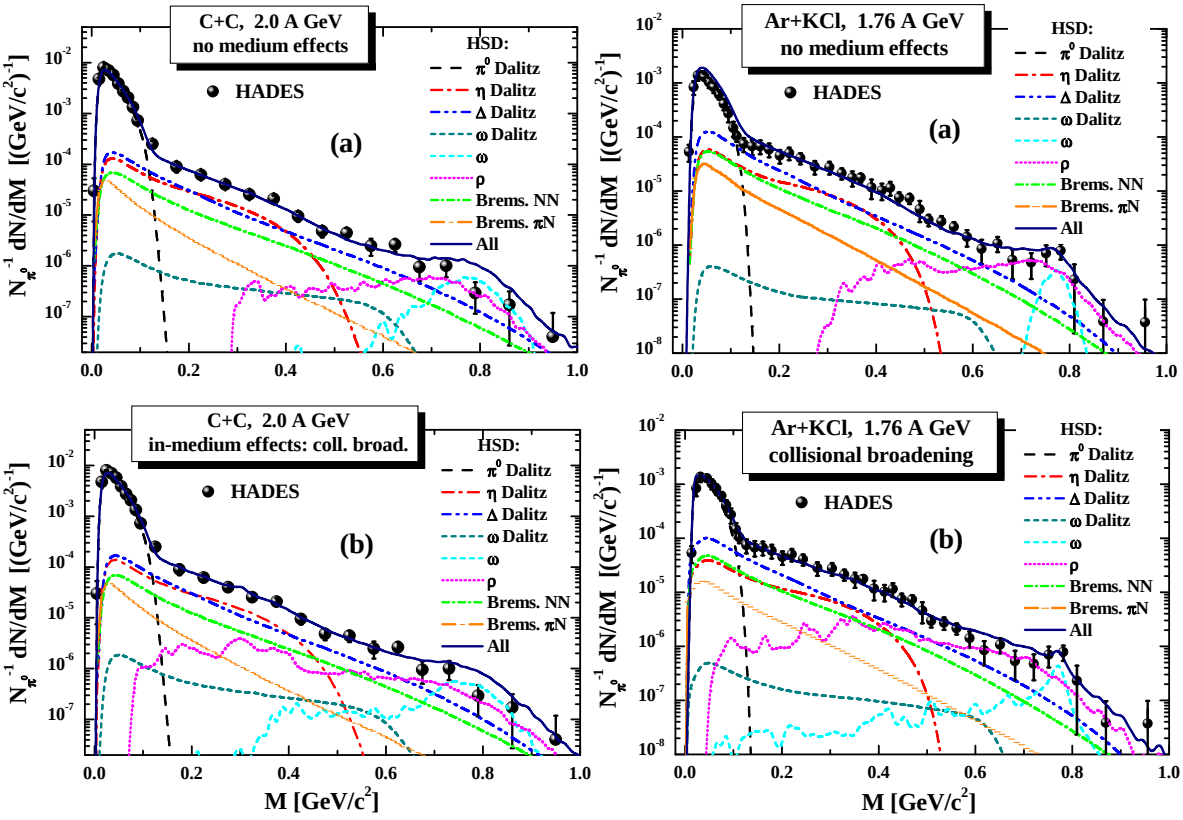


Figure 38: The mass differential dilepton spectra - normalized to the π^0 multiplicity - from PHSD/HSD calculations for C+C at 2 AGeV (l.h.s.) and Ar+KCl at 1.76 AGeV (r.h.s.) in comparison to the HADES data [236, 237]. The upper parts (a) shows the case of 'free' vector-meson spectral functions while the lower parts (b) give the result for the 'collisional broadening' scenario. The different colour lines display individual channels in the transport calculation (see legend). The theoretical calculations passed through the corresponding HADES acceptance filter and mass/momentum resolutions. The figures are taken from Ref. [241].

7. Results on dilepton production in heavy-ion collisions

7.1. SIS energies

The dileptons produced in low energy heavy-ion collisions have been measured first by the DLS Collaboration at Berkeley [227, 228, 229]. The observed dilepton yield [229] in the mass range from 0.2 to 0.5 GeV in C+C and Ca+Ca collisions at 1 A GeV was about of five times higher than the calculations by different transport models using the 'conventional' dilepton sources as bremsstrahlung, $\pi^0-, \eta-, \omega-$ and Δ-Dalitz decays and direct vector mesons (ρ, ω, ϕ) decays [165, 230, 231]. Even when including the different in-medium scenarios such as 'collisional broadening' and 'dropping mass' for the ρ-meson spectral function did not solve the "DLS puzzle" [151, 152, 232, 233].

The recent experimental data from the HADES Collaboration at GSI [234, 235, 236, 237], however, confirmed the measurement of the DLS Collaboration for C+C at 1.0 A GeV [235] as well as for the elementary reactions [238]. In the mean time also the theoretical transport approaches as well as effective models for the elementary NN reactions have been further developed. A possible solution of the "DLS puzzle" from the theoretical side has been suggested in Ref. [161] by incorporating stronger pn and pp bremsstrahlung contributions in line with the updated One-Boson-Exchange (OBE) model calculations from Kaptari and Kämpfer [150]. As shown in Ref. [161] the results from the HSD approach with 'enhanced' bremsstrahlung cross sections agree very well with the HADES data for C+C at 1 and 2 A GeV as well as with the DLS data for C + C and Ca + Ca at 1 A GeV, especially when including a collisional broadening in the vector-meson spectral functions. A similar finding has been obtained by other independent transport groups, i.e. the IQMD [239] and the Rossendorf BUU [240] collaborations.

Since all (relevant) elementary dilepton channels have been described in Section 5 we may step on with the actual results for A+A reactions. Note that at SIS energies of 1–2 AGeV the HSD and PHSD results are

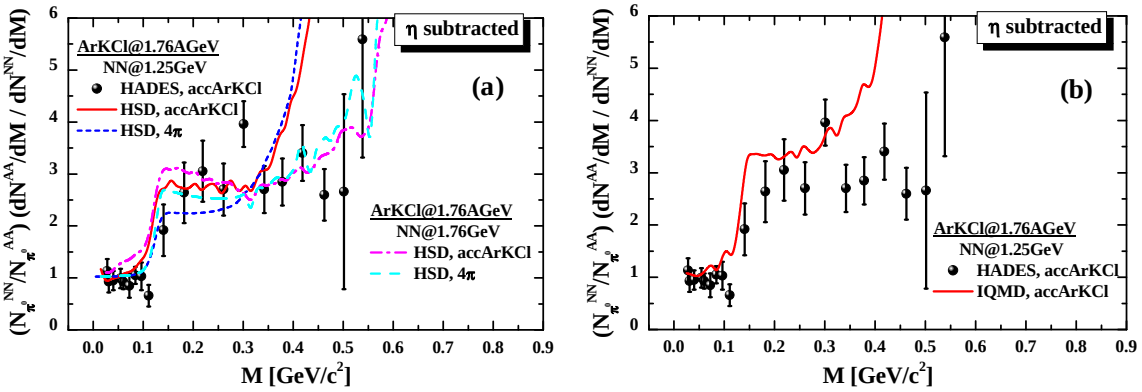


Figure 39: The PHSD/HSD (l.h.s.) and IQMD (r.h.s.) results for the ratio of the dilepton differential spectra – normalized to the π^0 multiplicity and after η Dalitz yield subtraction – to the isospin-averaged reference spectra $NN = (pp + pn)/2$ taken at 1.25 GeV, involving Ar+KCl experimental acceptance (solid line) and for 4π (short dashed line). Also the PHSD/HSD results for the ratio to the reference NN spectra taken at 1.76 GeV are shown, with the Ar+KCl experimental acceptance (dash-dotted line) and in 4π (dashed line). The figures are taken from Ref. [241].

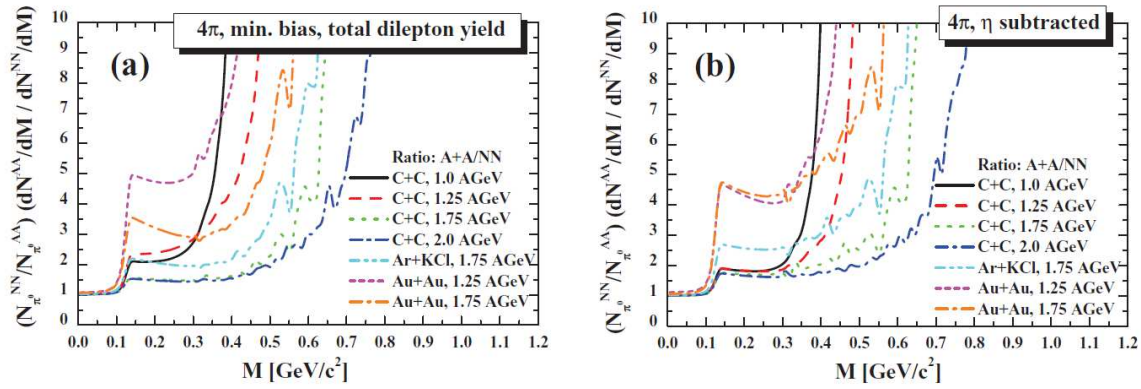


Figure 40: (l.h.s.) The ratio $(1/N_{\pi^0}^{AA} dN^{AA}/dM)/(1/N_{\pi^0}^{NN} dN^{NN}/dM)$ of the invariant mass differential dilepton 4π spectra - normalized to the π^0 multiplicity - from HSD/PHSD calculations for minimum bias $A + A$ collisions: We display C+C, Ar+KCl, Au+Au collisions in comparison to the isospin-averaged reference spectra $NN = (pn + pp)/2$ at 1.0, 1.25, 1.75, 2.0 AGeV. (r.h.s.) the same ratios but for the dilepton spectra after η Dalitz decay subtraction. The figures are taken from Ref. [241].

equivalent because no partonic subsystems are formed. Fig. 38 (l.h.s.) shows the mass differential dilepton spectra – normalized to the π^0 multiplicity – from PHSD/HSD calculations for C+C at 2 AGeV in comparison to the HADES data [236]. The theoretical calculations passed through the corresponding HADES acceptance filters and mass/momentum resolutions which leads to a smearing of the spectra at high invariant mass and particularly in the ω-resonance region. The upper part shows the case of 'free' vector-meson spectral functions while the lower part presents the result for the 'collisional ρ broadening' scenario. Here the difference between the in-medium scenarios is of minor importance and partly due to the limited mass resolution which smears out the spectra. Fig. 38 (r.h.s.) displays the mass differential dilepton spectra - normalized to the π^0multiplicity - from HSD calculations for the heavier system Ar+KCl at 1.76 AGeV in comparison to the HADES data [237]. The upper part shows again the case of 'free' vector-meson spectral functions while the lower part gives the result for the collisional broadening of the ρ-meson. Also in this data set the enhancement around the ρ mass is clearly visible. For the heavier system the 'collisional broadening' scenario shows a slightly better agreement with experiment than the 'free' result and we expect that for even heavier systems the difference between the two approaches increases.

Some rather model independent results are expected when comparing the dilepton mass spectra from A+A to 1/2 (pp+pn) reactions normalized to the π^0 multiplicity and subtracting the (known) η-Dalitz decay contribution. The left panel of Fig. 39 shows the PHSD/HSD results for the ratio of the dilepton differential spectra - normalized to the π^0 multiplicity and after η Dalitz yield subtraction - to the isospin-averaged reference spectra

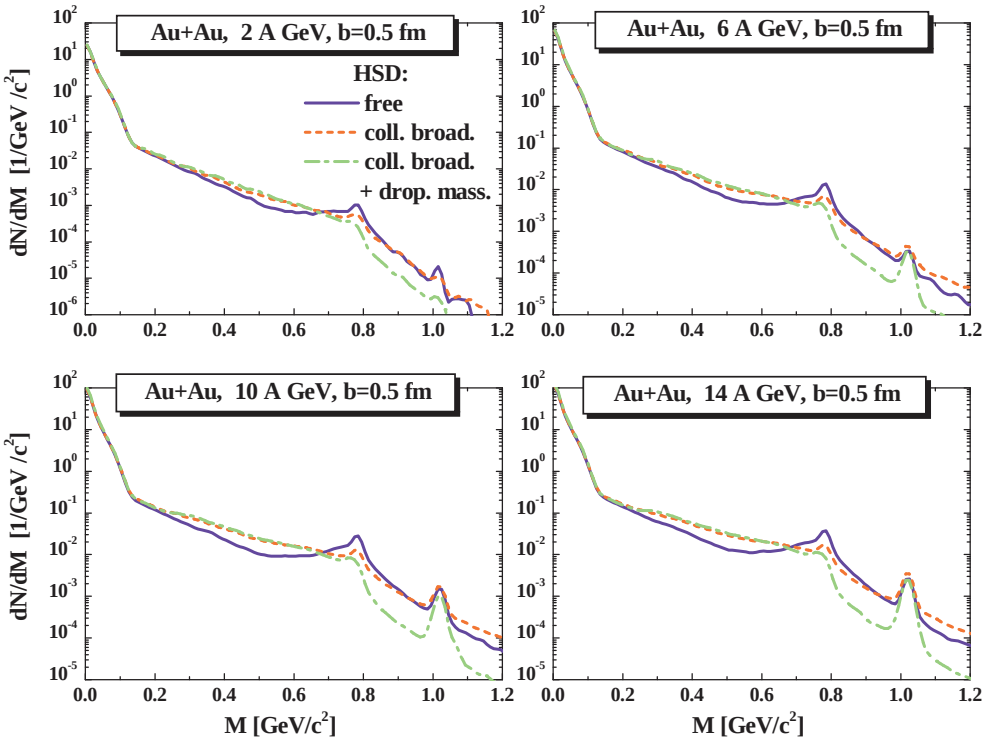


Figure 41: Predictions of the HSD/PHSD transport calculation for the mass differential dilepton spectra for very central Au+Au collisions from 2 to 14 A GeV calculated for different in-medium scenarios - collisional broadening and the combined scenario (dropping mass + collisional broadening). Figure is taken from Ref. [242].

$NN = (pp+pn)/2$ taken at 1.25 GeV and employing the Ar+KCl experimental acceptance (solid line) and in 4π (short dashed line). We display as well the ratio of Ar+KCl at 1.76 AGeV to the reference NN spectrum at the same energy, including the experimental Ar + KCl acceptance (dash-dotted line) and in 4π (dashed line). These results show clearly that for invariant masses of 0.1 $GeV < M <$ 0.35 GeV the data as well as theory are not a mere superposition of the elementary spectra. The comparison also excludes that this enhancement, observed in heavy-ion collisions, is due to acceptance since the results with acceptance and in 4π are very similar. At larger invariant masses theory and data do not agree because the bump at the invariant masses around $M \approx 0.5$ GeV, seen in the experimental pd reactions, is not reproduced by theory. Taking the reference spectra at the same nominal energy the theory predicts that this enhancement is constant up to energies of $M \approx 0.5$ GeV. Then the Fermi motion becomes important and yields a strong increase of the ratio. These PHSD/HSD results are confirmed by the IQMD calculations shown in the right panel of Fig. 39.

We note that with increasing mass A+A of the system the low mass dilepton regime from roughly 0.15 to 0.5 GeV in the transport calculations increases due to multiple Δ-resonance production and Dalitz decay. The dileptons from intermediate Δ's, which are part of the reaction cycles $\Delta \to \pi N; \pi N \to \Delta$ and $NN \to N\Delta; N\Delta \to NN$, escape from the system while the decay pions do not [241]. With increasing system size more generations of intermediate Δ's are created and the dilepton yield is enhanced accordingly. In inclusive C+C collisions there is only a moderate enhancement relative to scaled p+p and p+n collisions due to the small size of the system while in Ar+KCl reactions already several (3-4) reaction cycles become visible. A similar finding has been obtained within the IQMD transport model (cf. Figs. 25, 27, 29 in Ref. [241]). This effect enhances with the system size and reaches a factor of 4.5-5.0 for Au+Au minimum bias at 1.25 A GeV as illustrated in Fig. 40 which presents the ratio $(1/N_{\pi^0}^{AA} dN^{AA}/dM)/(1/N_{\pi^0}^{NN} dN^{NN}/dM)$ of the mass differential dilepton spectra - normalized to the π^0 multiplicities - obtained in HSD/PHSD calculations. Displayed are the ratios of minimum bias C+C, Ar+KCl, Au+Au collisions and of the isospin-averaged reference spectra $NN = (pn + pp)/2$ at the same energy (l.h.s.). The right hand side depicts the same ratios but for the dilepton spectra after η-Dalitz

yield subtraction. Additionally to the Δ regeneration, the pN bremsstrahlung – which scales with the number of collisions and not with the number of participants, i.e. pions – contributes to the enhancement of the ratio in Fig. 40.

Based on the study in Ref. [241] this enhancement can be attributed to two effects: i) the bremsstrahlung radiation from pn and pp reactions which does not scale with the pion number (i.e. the number of participants) but rather with the number of elementary elastic collisions; ii) the shining of dileptons from the 'intermediate' Δ's, which take part in the $\Delta \to \pi N$ and $\pi N \to \Delta$ reaction cycle. This cycle produces a number of generations of Δ's during the reaction which increases with the size of the system. At the end only one pion is produced but each intermediate Δ has contributed to the dilepton yield because the emitted dileptons are not absorbed (unlike pions). This leads to an enhancement of the dilepton yield when compared to the final number of pions. Thus, the enhancement confirms the predictions of transport theories that in heavy-ion collisions several generations of Δ's are formed which decay and are recreated by $\pi N \to \Delta$ reactions. Accordingly, the dilepton data from $A + A$ reactions shed light on the Δ-resonance dynamics in the medium especially at SIS energies.

7.2. AGS energies

In the AGS energy regime from 2 to 14 A GeV no dilepton data have been taken so far but are foreseen in the HADES and CBM experiments at FAIR. We thus show in Fig. 41 the HSD/PHSD predictions for the dilepton yields from central Au + Au collisions calculated for different energies from 2 to 14 A GeV applying the different in-medium scenarios: collisional broadening and the combined approach (dropping mass + collisional broadening). One can see from Fig. 41 that both scenarios lead to an enhancement of the dilepton yield in the mass region $M = 0.3 - 0.8$ GeV by a factor of about 2. The largest in-medium effect is, however, attributed to the reduction of the dilepton yield between the ω and ϕ peaks due to the downward shift of the poles of the ρ and ω spectral functions in case of the dropping mass scenario. However, the latter scenario is not consistent with existing experimental data at higher energies (see Subsection 7.3), so one has to rely most likely on the relatively modest in-medium effects due to a collisional broadening of the vector mesons in the medium (dashed line).

7.3. SPS energies

We step up in energy and compare model results with experimental data for dileptons from In+In collisions at 160 A GeV measured by the NA60 Collaboration. In Fig. 42 we present PHSD results for the dilepton excess over the known hadronic sources as produced in In+In reactions at 158 A GeV compared to the acceptance corrected data. We find here that the spectrum at invariant masses in the vicinity of the ρ-meson peak is well reproduced by the ρ meson yield, if a broadening of the meson spectral function in the medium is assumed, while the partonic sources account for the yield at high masses. Our analysis shows that the contributions of the "4π" processes (shown by the lines with symbols) – as first noted by the authors of Ref. [138] – are very much suppressed.

One concludes from Fig. 42 that the measured spectrum for $M > 1$ GeV is dominated by the *partonic* sources. Indeed, the dominance of the radiation from the QGP over the hadronic sources in PHSD is related to a rather long – of the order or 3 fm/c – evolution in the partonic phase (in co-existence with the space-time separated hadronic phase) on one hand (cf. Fig. 10 of Ref. [31]) and the rather high initial energy densities created in the collision on the other hand (cf. Fig. 6 of Ref. [248]). In addition, we find from Fig. 42 that in PHSD the partonic sources also have a considerable contribution to the dilepton yield for $M < 0.6$ GeV. The yield from the two-to-two process $q + \bar{q} \to g + l^+l^-$ is especially important close to the threshold (≈ 0.211 GeV). This conclusion from the microscopic calculation is in qualitative agreement with the findings of an early (more schematic) investigation in Ref. [249]. For related results from alternative models we refer the reader to the right panel of Fig. 42.

The comparison of the mass dependence of the slope parameter evolution in PHSD and the data from NA60 is shown explicitly in Fig. 43. Including the partonic dilepton sources allows to reproduce in PHSD the m_T-spectra as well as the finding of the NA60 Collaboration [243, 244, 245, 246, 247] that the effective temperature of the dileptons (slope parameters) in the intermediate mass range is lower than that of the dileptons in the mass bin $0.6 < M < 1$ GeV, which is dominated by hadronic sources (cf. Fig. 43). The softening of the transverse mass spectrum with growing invariant mass implies that the partonic channels occur dominantly before the collective radial flow has developed. Also, the fact that the slope in the lowest mass bin and the highest one are approximately similar – both in the data and in the PHSD – can be traced back to the two windows of the

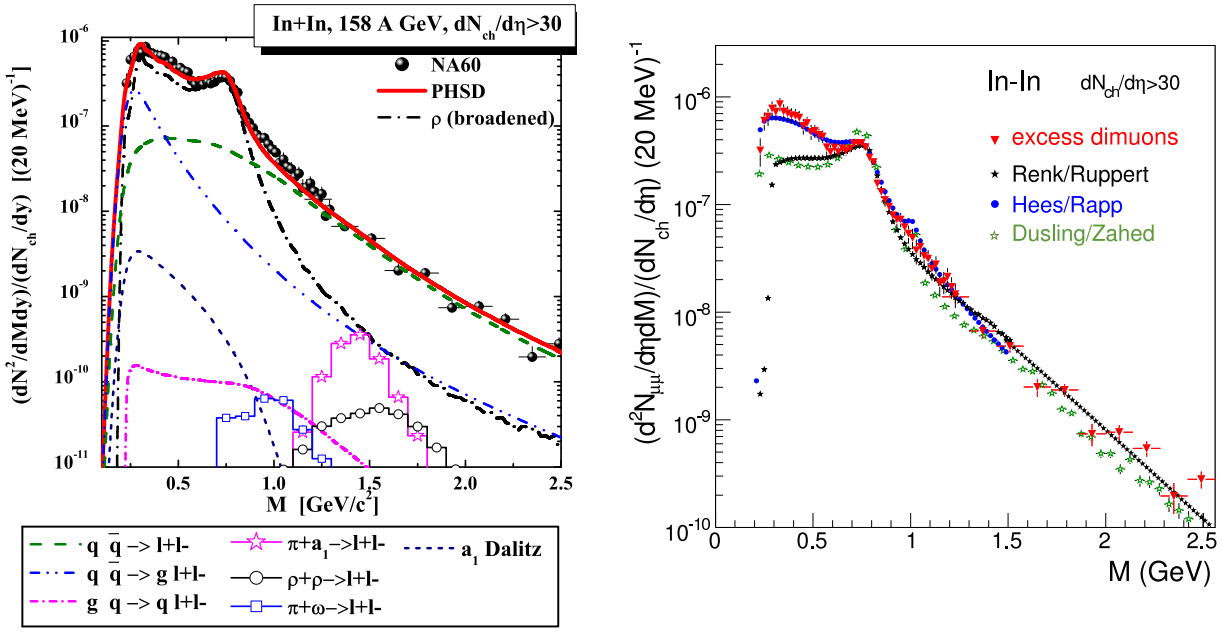


Figure 42: (l.h.s.) Acceptance corrected mass spectra of excess dimuons from In+In at 158 A GeV integrated over p_T in $0.2 < p_T < 2.4$ GeV from PHSD compared to the data of NA60 [243]. The dash-dotted line shows the dilepton yield from the in-medium ρ with a broadened spectral function, the dashed line presents the yield from the $q + \bar{q}$ annihilation, the dash-dot-dot line gives the contribution of the gluon Bremsstrahlung process ($q\bar{q} \to gl^+l^-$), while the solid line is the sum of all contributions. For the description of the other lines, which correspond to the non-dominant channels, we refer to the figure legend. The figure is taken from Ref. [140]. (r.h.s.) Acceptance-corrected invariant mass spectrum of excess dimuons in In+In collisions at 158 A GeV in comparison to model results from Renk and Ruppert, van Hees and Rapp as well as Dusling and Zahed. The figure is taken from Refs. [244, 245, 246, 247, 243].

mass spectrum that in our picture are influenced by the radiation from the sQGP: $M = 2M_\mu - 0.6$ GeV and $M > 1$ GeV. For more details we refer the reader to Ref. [140].

7.4. RHIC energies

Now we are coming to the top RHIC energy of $\sqrt{s_{NN}} = 200$ GeV and present the most important findings from the PHSD study in Ref. [141]. In the left part of Fig. 44 we show the PHSD results for the invariant mass spectra of inclusive dileptons in Au+Au collisions for the acceptance cuts on single electron transverse momenta p_{eT}, pseudorapidities η_e, azimuthal angle ϕ_e, and dilepton pair rapidity y: $p_{eT} > 0.2$ GeV, $|\eta_e| < 0.35$, $-3\pi/16 < \phi_e < 5\pi/16$, $11\pi/16 < \phi_e < 19\pi/16$, $|y| < 0.35$.

In the low mass region $M = 0-1.2$ GeV, the dilepton yield in the PHSD is dominated by hadronic sources and roughly coincides with the earlier HSD result in Ref. [142]. Note that the collisional broadening scenario for the modification of the ρ-meson was used in the calculations presented in Fig. 44 that underestimates the PHENIX data from the run 2004 in the mass range from 0.2 to 0.7 GeV substantially. In contrast, the partonic radiation as well as the yield from correlated D-meson decays dominate and saturate the mass region $M = 1 - 3$ GeV as seen in Fig. 44 (left panel), i.e. between the ϕ and J/Ψ peaks. The dileptons generated by the quark-antiquark annihilation in the sQGP from PHSD constitute about half of the observed yield in this intermediate-mass range. For $M > 2.5$ GeV the partonic yield is even higher than the D-meson contribution. Thus, the inclusion of the partonic radiation in the PHSD fills up the gap between the hadronic model results [142] and the data of the PHENIX Collaboration for $M > 1$ GeV. However, the early expectation of a strong partonic signal in the low mass dilepton spectrum is not substantiated by the microscopic PHSD calculations.

In order to investigate the "low-mass dilepton problem", the PHENIX Collaboration has performed a new measurement in 2010 with a different magnetic field setting, addition of the Hadron-Blind Detector, and modified analysis. The results of this experimental effort (very recently presented in Ref. [253]) are shown in the right hand side of Fig. 44. The new measurements suggest that the dilepton yield in the low-mass region from 0.2

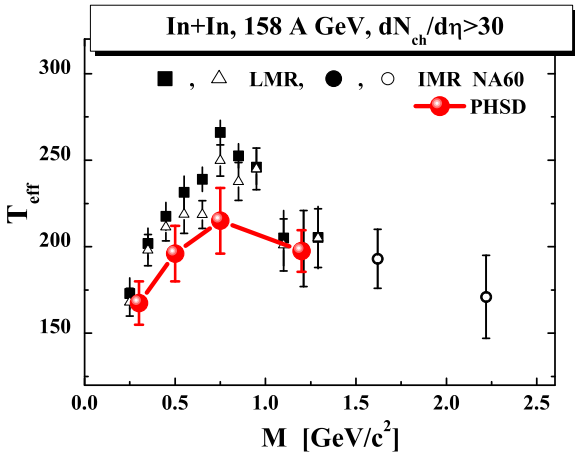


Figure 43: The inverse slope parameter T_{eff} of the dimuon yield from In+In at 158 A GeV as a function of the dimuon invariant mass M in PHSD (solid line with full dots) compared to the data of the NA60 Collaboration [243, 244, 245, 246, 247]. The figure is taken from Ref. [140].

to 0.7 GeV does no longer show such a strong enhancement over the cocktail of hadronic decay sources as assumed based on the earlier PHENIX analysis in Ref. [112, 250, 251, 252]. In fact, the new PHENIX data are in agreement with the theoretical expectations from the PHSD calculations.

In order to shed some further light on the "PHENIX puzzle", we compare the PHSD predictions with the data independently measured for Au+Au collisions at $\sqrt{s_{NN}} = 200$ GeV by the STAR Collaboration. The calculations are performed for the same model assumptions and parameters as those used for the comparison to the PHENIX data, only the different acceptance cuts on single electron transverse momenta p_{eT}, single electron pseudorapidities η_e and the dilepton pair rapidity y, i.e. $0.2 < p_{eT} < 5$ GeV, $|\eta_e| < 1$, $|y| < 1$. The PHSD predictions for the dilepton yield within these cuts are shown in Fig. 45 for 0-80%. One can observe generally a good agreement with the data from the STAR Collaboration [254] in the whole mass regime. Notably, our calculations are also roughly in line with the low mass dilepton spectrum from STAR in case of the most central collisions, whereas the PHSD results severely underestimated the PHENIX data from the Run 2004 analysis for central collisions. The observed dilepton yield from STAR can be accounted for by the known hadronic sources, i.e. the decays of the π_0, η, η', ω, ρ, ϕ and a_1 mesons, of the Δ particle and the semi-leptonic decays of the D and $\bar{D}$ mesons, where the collisional broadening of the ρ-meson is taken into account.

More recently, the STAR Collaboration has released information on the explicit centrality dependence of the dilepton spectra. Fig. 46 shows the comparison of the STAR data of midrapidity dilepton yields (l.h.s.) and its ratios (r.h.s.) to the 'cocktail' for 0-10%, 10-40%, 40-80%, 0-80% central Au+Au collisions at $\sqrt{s_{NN}} = 200$ GeV in comparison to the predictions from the PHSD approach and the expanding fireball model of Rapp and collaborators. As seen from Fig. 46 the excess of the dilepton yield over the expected cocktail is larger for very central collisions and consistent with the model predictions including the collisional broadening of the ρ-meson spectral function at low invariant mass and QGP dominated radiations at intermediate masses. Accordingly, the tension between the PHENIX and STAR dilepton data (as well as PHSD predictions) no longer persists.

Moreover, the recent STAR dilepton data for Au+Au collisions from the Beam Energy Scan (BES) program for $\sqrt{s_{NN}} = 19.6, 27, 39$ and 62.4 GeV [205, 255] are also in line with the PHSD (as well as the expanding fireball model) predictions with a ρ-meson collisional broadening. According to the PHSD calculations the excess is increasing with decreasing energy due to a longer ρ-meson propagation in the high-baryon density phase (see Fig. 3 in Ref. [205]).

7.5. LHC energies

On the other hand, the upcoming ALICE data [256] for heavy-ion dileptons for Pb+Pb at $\sqrt{s} = 2.76$ TeV might give a further access to the dileptons emitted from the QGP [257, 258]. In Fig. 47 (l.h.s.) we present the PHSD predictions for central Pb+Pb collisions [258] in the low mass sector for a lepton p_T cut of 1 GeV/c. It is clearly seen that the QGP sources and the contribution from correlated $D\bar{D}$ pairs are non-leading in the

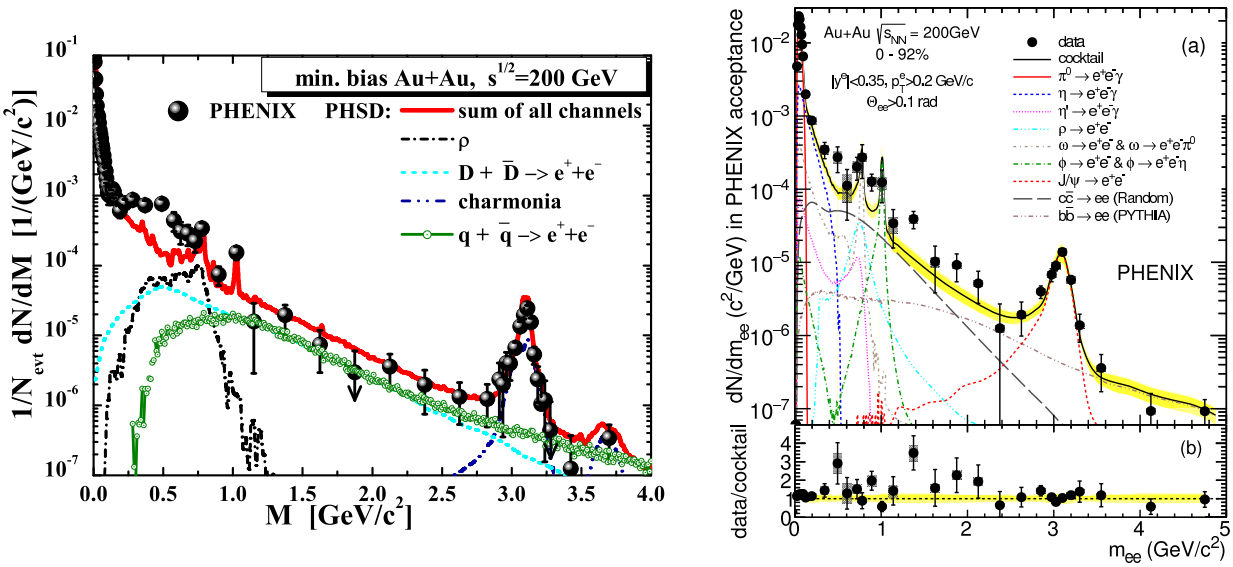


Figure 44: (l.h.s.) The PHSD results for the invariant mass spectra of inclusive dileptons in Au+Au collisions at $\sqrt{s_{NN}} = 200$ GeV within the PHENIX acceptance cuts in comparison to the data from the PHENIX Collaboration [112, 250, 251, 252] based on the data from 2004. The different lines indicate the contributions from different channels as specified in the figure, which is taken from Ref. [141]. (r.h.s.) New data of the PHENIX Collaboration measured in 2010 with the Hadron-Blind Detector compared to the cocktail of hadron decays. The figure is taken from Ref. [253].

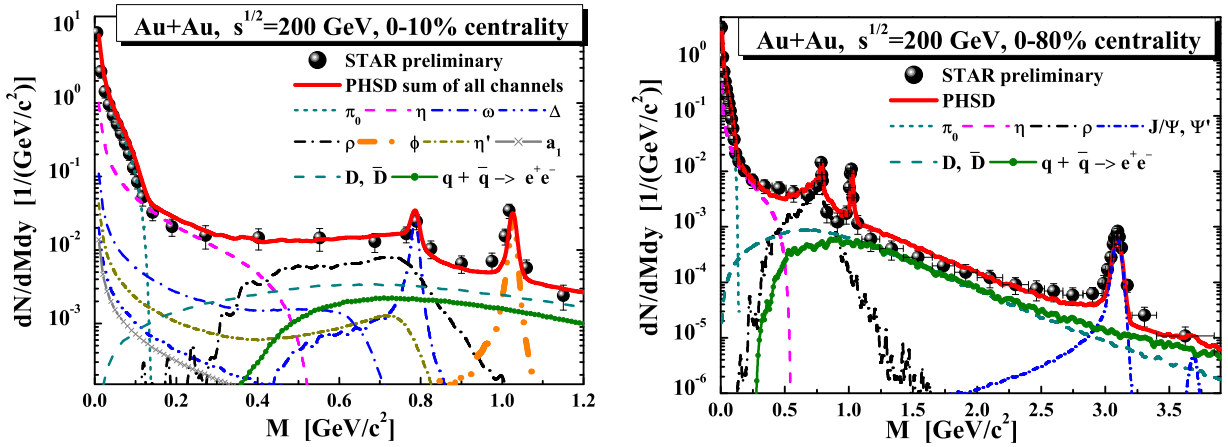


Figure 45: The PHSD results for the invariant mass spectra of dileptons in Au+Au collisions at $\sqrt{s_{NN}} = 200$ GeV for $M = 0$–1.2 GeV (left panel) and for $M = 0 - 4$ GeV (right panel) for 0 - 10 % or 0 - 80% centrality within the cuts of the STAR experiment. The data of the STAR Collaboration are adopted from Ref. [254]. The figures are taken from Ref. [141].

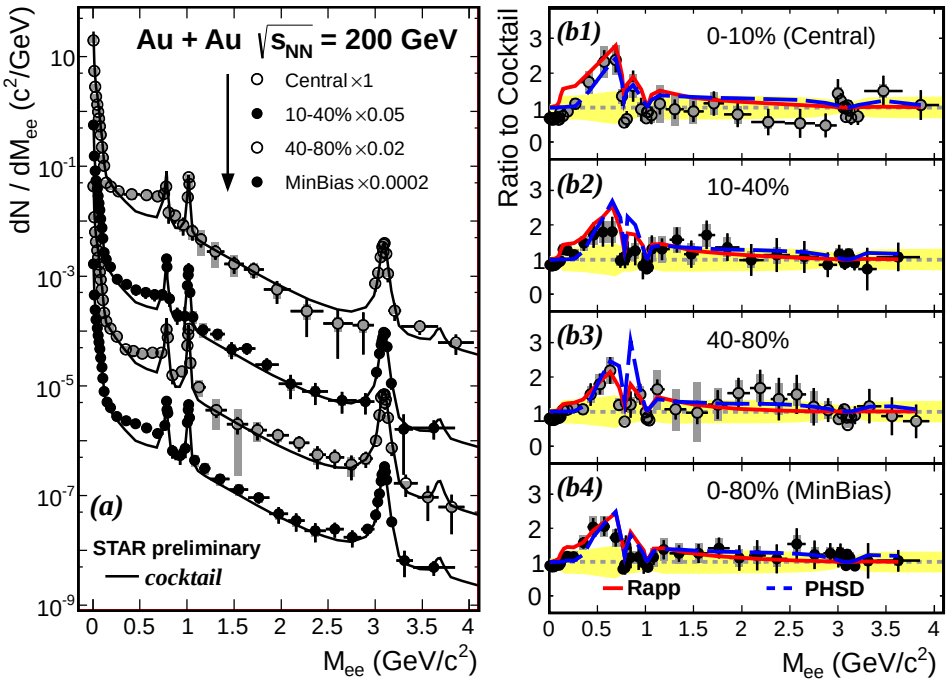


Figure 46: Centrality dependence of the midrapidity dilepton yields (left) and its ratios (right) to the 'cocktail' for 0-10%, 10-40%, 40-80%, 0-80% central Au+Au collisions at $\sqrt{s} = 200$ GeV: comparison of STAR data with theoretical predictions from the PHSD ('PHSD' - dashed lines) and the expanding fireball model ('Rapp' - solid lines). The figures are taken from Ref. [255].

low mass regime where we find the conventional hadronic sources. For a lepton p_T cut of 1 GeV/c (l.h.s.) one practically cannot identify an effect of the ρ-meson collisional broadening in the dilepton spectra in the PHSD calculations. Only when applying a low p_T cut of 0.15 GeV/c a small enhancement of the dilepton yield from 0.3 to 0.7 GeV becomes visible (r.h.s. of Fig. 47). This low sensitivity to hadronic in-medium effects at LHC energies from the PHSD is due to the fact that the hadrons appear late (after hadronization) in central Pb+Pb collisions and are boosted to high velocities due to the high pressure in the early partonic phase.

In the end, we mention that promising perspectives with dileptons have been suggested in Ref. [259] to measure the flow anisotropy coefficients v_n ($n = 2, 3$) similar to photons. The calculations with the viscous (3+1)d MUSIC hydro for central Au+Au collisions at RHIC energies show that the flow coefficients v_2, v_3 are sensitive to the dilepton sources and to the EoS and η/s ratio. The main advantage of measuring flow coefficients v_n with dileptons compared to photons is the fact that the extra degree-of-freedom M might allow to disentangle the sources additionally.

8. Summary

In this report we have addressed the dynamics of relativistic heavy-ion reactions and in particular the information obtained from electromagnetic probes that stem from the partonic and hadronic phases. While the out-of-equilibrium description of strongly interacting relativistic fields has been based on the theory of Kadanoff and Baym (Section 2), the description of QCD in equilibrium has been performed within an effective dynamical quasiparticle model (DQPM) (Section 3). The width of the dynamical quasiparticles is controlled by transport coefficients in equilibrium that can be compared to the same quantities from lattice QCD (Section 4). The resulting off-shell transport approach is denoted by Parton-Hadron-String Dynamics (PHSD) and reproduces the equation of state, the sound velocity squared $c_s^2(T)$ as well as the relevant transport coefficients such as the shear viscosity η, the bulk viscosity ζ and the electrical conductivity σ_0 in the partonic phase from lattice QCD. Furthermore, it includes dynamical transition rates for hadronization, i.e. for the change of colored partonic to color-neutral hadronic degrees-of-freedom, that satisfy all conservation laws and do not violate the second law of thermodynamics. It has been shown that the PHSD captures the bulk dynamics of heavy-ion collisions from lower SPS to LHC energies and thus provides a solid ground for the evaluation of the electromagnetic

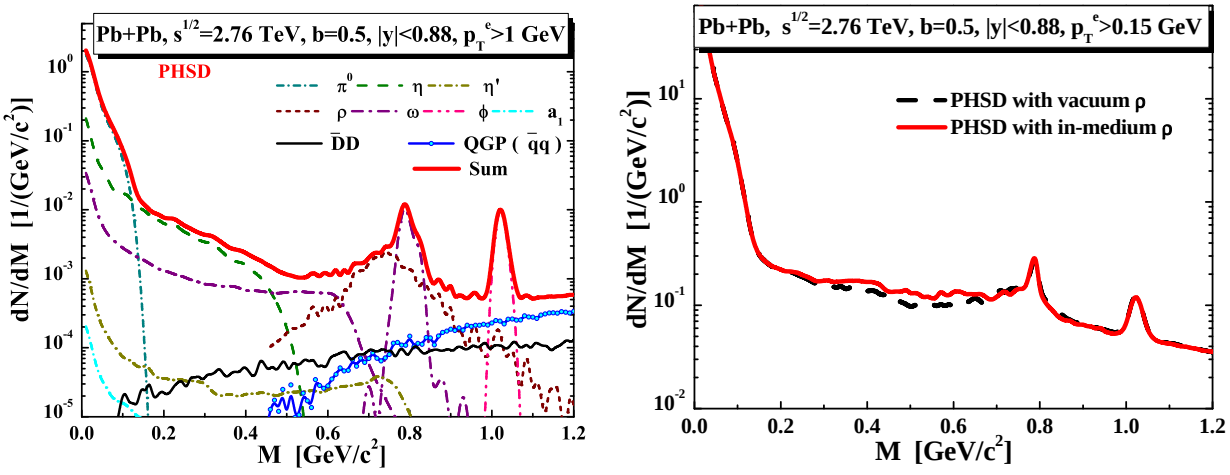


Figure 47: (l.h.s.) Midrapidity dilepton yields for Pb+Pb at $\sqrt{s_{NN}}$ = 2.76 TeV for a lepton p_T cut of 1 GeV/c. The channel decomposition is explained in the legend. (r.h.s.) Same as for the l.h.s. but for a lepton p_T cut of 0.15 GeV/c for a 'free' ρ spectral function (dashed line) and the collisional broadening scenario (solid line). The figures are taken from Ref. [258].

emissivity on the basis of the same dynamical propagators in the partonic phase that are employed for the dynamical evolution of the partonic system (Section 5). The PHSD 'tests' indicate that the 'soft' physics at LHC in central A-A reactions is very similar to the top RHIC energy regime although the invariant energy is higher by more than an order of magnitude. Furthermore, the PHSD approach is seen to work from lower SPS energies up to LHC energies for p-p, p-A as well as A-A collisions, i.e. over a range of more than two orders in $\sqrt{s_{NN}}$. Note that for even lower bombarding energies the PHSD approach merges to the HSD model, which has been successfully tested for p-A and A-A reactions from the SIS to the SPS energy regime in the past [39].

The main messages from the *photon* studies in Section 6 can be summarize in short as:

- the photons provide a critical test for the theoretical models: the standard dynamical models - constructed to reproduce the 'hadronic world' - fail to explain the photon experimental data;
- the details of the hydro models (fluctuating initial conditions, viscosity, pre-equilibrium flow) have a small impact on the photon observables;
- as suggested by the PHSD transport model calculations, the role of such background sources as mm and mB bremsstrahlung has been underestimated in the past and was found to be dominant at low photon p_T;
- the dynamics of the initial phases of the reaction might turn out to be important (pre-equilibrium /'initial' flow, Glasma effect etc.).

Finally, one must conclude that the photons are one of the most sensitive probes for the dynamics of HIC and for the role of the partonic phase. We also mention that in an initial 'glasma' phase the photon/dilepton production is suppressed by about an order of magnitude since the gluon fields do not carry electric charge. In this case the *direct* photons would practically stem for the hadronic stages and carry the full hadronic elliptic flow v_2.

The main messages from the dilepton studies in Section 7 are:

- at low masses ($M = 0.2 - 0.6$ GeV/c^2) the dilepton spectra show sizable changes due to hadronic in-medium effects, i.e. multiple hadronic resonance formation or a modification of the properties of vector mesons (such as collisional broadening) in the hot and dense hadronic medium (partially related to chiral symmetry restoration); these effects can be observed at all energies from SIS to LHC but are most pronounced in the FAIR/NICA energy regime;

- at intermediate masses the QGP ($q\bar{q}$ thermal radiation) dominates for $M > 1.2$ GeV/c^2. The fraction of QGP sources grows with increasing energy and becomes dominant at the LHC energies.

- The tension between the PHENIX and STAR dilepton data at the top RHIC energy (as well as PHSD predictions) no longer persists.

Finally, the dilepton measurements within the future experimental energy and system scan (pp, pA, AA) from low to top RHIC energies as well as new ALICE data at LHC energies will extend our knowledge on the properties of hadronic and partonic matter via its electromagnetic radiation and show if the very initial degrees-of-freedom in relativistic heavy-ion collisions are electrically charged (quarks and antiquarks) or not (gluons).

Acknowlegements

The authors are grateful to J. Aichelin, H. Berrehrah, M. Bleicher, C. Gale, G. David, A. Drees, H. v. Hees, U. Heinz, B. Jacak, B. Kämpfer, C. M. Ko, V. Konchakovski, J. Manninen, V. Ozvenchuk, A. Palmese, J.-F. Paquet, K. Reygers, E. Seifert, C. Shen, T. Song, J. Stachel, T. Steinert, V. Toneev and K. Werner for valuable discussions and their contributions to this review. The computational resources have been provided by the LOEWE-CSC as well as by the SKYLLA cluster at the Univ. of Giessen. This work in part has been supported by DFG as well as by the LOEWE center HIC for FAIR.

References

References

[1] J. S. Schwinger, J. Math. Phys. 2 (1961) 407.

[2] P. M. Bakshi, K. T. Mahanthappa, J. Math. Phys. 4 (1963) 12.

[3] L. Keldysh, Zh. Eksp. Teor. Fiz. 47 (1964) 1515.

[4] L. Keldysh, Sov. Phys. JETP. 20 (1965) 1018.

[5] R. A. Craig, J. Math. Phys. 9 (1968) 650.

[6] L. P. Kadanoff, G. Baym, Quantum statistical mechanics, Benjamin, New York, 1962.

[7] M. Bonitz, Quantum kinetic theory, B.G. Teubner, Stuttgart, 1998.

[8] D. F. DuBoi, in Lectures in Theoretical Physics, edited by W. E. Brittin, Gordon and Breach, New York, 1967.

[9] P. Danielewicz, Annals Phys. 152 (1984) 239.

[10] K.-C. Chou, Z.-B. Su, B.-L. Hao, L. Yu, Phys. Rept. 118 (1985) 1.

[11] J. Rammer, H. Smith, Rev. Mod. Phys. 58 (1986) 323.

[12] E. Calzetta, B. Hu, Phys. Rev. D37 (1988) 2878.

[13] H. Haug, A. P. Jauho, Quantum Kinetics in Transport and Optics of Semiconductors, Springer, New York, 1999.

[14] B. Bezzerides, D. F. DuBois, Ann. Phys. 70 (1972) 10.

[15] W. Botermans, R. Malfliet, Phys. Rept. 198 (1990) 115.

[16] S. Mrowczynski, P. Danielewicz, Nucl. Phys. B342 (1990) 345.

[17] A. Makhlin, Phys. Rev. C52 (1995) 995–1021.

[18] A. Makhlin, E. Surdutovich, Phys. Rev. C58 (1998) 389.

[19] K. Geiger, Phys. Rev. D54 (1996) 949.

[20] K. Geiger, Phys. Rev. D56 (1997) 2665.

[21] D. A. Brown, P. Danielewicz, Phys. Rev. D58 (1998) 094003.

[22] J.-P. Blaizot, E. Iancu, Nucl. Phys. B557 (1999) 183–236.

[23] Y. Ivanov, J. Knoll, D. Voskresensky, Nucl. Phys. A657 (1999) 413.

[24] J. Knoll, Y. Ivanov, D. Voskresensky, Annals Phys. 293 (2001) 126.

[25] S. Wang, W. Cassing, Annals Phys. 159 (1985) 328.

[26] S. Juchem, W. Cassing, C. Greiner, Phys. Rev. D69 (2004) 025006.

[27] K. Morawetz, H. Köhler, Eur. Phys. J. A4 (1999) 291.

[28] H. Köhler, K. Morawetz, Phys. Rev. C64 (2001) 024613.

[29] S. Juchem, W. Cassing, C. Greiner, Nucl. Phys. A743 (2004) 92.

[30] L. Rauber, W. Cassing, Phys. Rev. D89 (2014) 065008.

[31] W. Cassing, E. L. Bratkovskaya, Nucl. Phys. A 831 (2009) 215.

[32] E. L. Bratkovskaya, W. Cassing, V. P. Konchakovski, O. Linnyk, Nucl. Phys. A856 (2011) 162.

[33] W. Cassing, Eur. Phys. J. ST 168 (2009) 3.

[34] A. Peshier, W. Cassing, Phys. Rev. Lett. 94 (2005) 172301.

[35] Y. Aoki, S. Borsanyi, S. Durr, Z. Fodor, S. D. Katz, S. Krieg, K. K. Szabo, JHEP 06 (2009) 088.

[36] B. Vanderheyden, G. Baym, J. Stat. Phys. 93 (1998) 843.

[37] C. Bonati, M. D'Elia, M. Mariti, M. Mesiti, F. Negro, F. Sanfilippo, Phys. Rev. D90 (2014) 114025.

[38] W. Ehehalt, W. Cassing, Nucl. Phys. A 602 (1996) 449.

[39] W. Cassing, E. L. Bratkovskaya, Phys. Rept. 308 (1999) 65.

[40] A. Peshier, Phys. Rev. D 70 (2004) 034016.

[41] W. Cassing, Nucl. Phys. A791 (2007) 365.

[42] W. Cassing, Nucl. Phys. A795 (2007) 70.

[43] H.-U. Bengtsson, T. Sjostrand, Comput. Phys. Commun. 46 (1987) 43.

[44] W. Cassing, E. L. Bratkovskaya, Phys. Rev. C 78 (2008) 034919.

[45] C. B. Dover, U. W. Heinz, E. Schnedermann, J. Zimanyi, Phys. Rev. C44 (1991) 1636–1654.

[46] S. A. Bass, et al., Prog. Part. Nucl. Phys. 41 (1998) 255.

[47] M. Bleicher, et al., J. Phys. G25 (1999) 1859–1896.

[48] T. Sjostrand, et al., Comput. Phys. Commun. 135 (2001) 238.

[49] Z.-W. Lin, C. M. Ko, B.-A. Li, B. Zhang, S. Pal, Phys. Rev. C72 (2005) 064901.

[50] A. Lang, et al., J. of Comp. Phys. 106 (1993) 391.

[51] W. Cassing, Nucl. Phys. A700 (2002) 618.

[52] Z. Xu, C. Greiner, Phys. Rev. C79 (2009) 014904.

[53] Z. Xu, C. Greiner, Nucl. Phys. A774 (2006) 787–790.

[54] Z. Xu, C. Greiner, Phys. Rev. C71 (2005) 064901.

[55] V. Ozvenchuk, O. Linnyk, M. Gorenstein, E. Bratkovskaya, W. Cassing, Phys. Rev. C87 (2013) 024901.

[56] R. Kubo, J. Phys. Soc. Jap. 12 (1957) 570.

[57] R. Kubo, Rep. Prog. Phys. 29 (1966) 255.

[58] P. Chakraborty, J. I. Kapusta, Phys. Rev. C83 (2011) 014906.

[59] S. Mattiello, W. Cassing, Eur. Phys. J. C70 (2010) 243.

[60] V. Ozvenchuk, O. Linnyk, M. Gorenstein, E. Bratkovskaya, W. Cassing, Phys. Rev. C87 (2013) 064903.

[61] W. Cassing, O. Linnyk, T. Steinert, V. Ozvenchuk, Phys. Rev. Lett. 110 (2013) 182301.

[62] T. Steinert, W. Cassing, Phys. Rev. C89 (2014) 035203.

[63] C. Blume, et al., J. Phys. G 35 (2008) 044004.

[64] H. Ströbele, et al., Proceedings of the CPOD-2009: Workshop on 'Critical Point and Onset of Deconfinemet', Brookhaven, June 8-12 (2009).

[65] L. McLerran, Nucl. Phys. A 787 (2007) 1.

[66] L. McLerran, Int. J. Mod. Phys. A 21 (2006) 694.

[67] V. Konchakovski, W. Cassing, V. Toneev, J. Phys. G 42 (2015) 055106.

[68] C. Alt, et al., Phys. Rev. C 66 (2002) 054902.

[69] C. Alt, et al., Phys. Rev. C 77 (2008) 024903.

[70] S. S. Adler, et al., Phys. Rev. C 69 (2004) 034909.

[71] J. Adams, et al., Phys. Rev. Lett. 92 (2004) 112301.

[72] E. L. Bratkovskaya, S. Soff, H. Stöcker, M. van Leeuwen, W. Cassing, Phys. Rev. Lett. 92 (2004) 032302.

[73] E. L. Bratkovskaya, et al., Phys. Rev. C69 (2004) 054907.

[74] B. B. Abelev, et al., Phys. Lett. B727 (2013) 371.

[75] K. Aamodt, et al., Phys. Rev. Lett. 107 (2011) 032301.

[76] V. Konchakovski, W. Cassing, V. Toneev, J. Phys. G41 (2014) 105004.

[77] B. Abelev, et al., Phys. Lett. B720 (2013) 52.

[78] B. B. Abelev, et al., Eur. Phys. J. C73 (2013) 2662.

[79] B. B. Abelev, et al., Phys. Lett. B736 (2014) 196.

[80] J. Adams, et al., Phys. Rev. Lett. 92 (2004) 052302.

[81] J. Adams, et al., Phys. Rev. Lett. 95 (2005) 122301.

[82] A. Adare, et al., Phys. Rev. Lett. 98 (2007) 162301.

[83] A. Adare, et al., Phys. Rev. Lett. 107 (2011) 252301.

[84] A. M. Poskanzer, S. Voloshin, Phys. Rev. C58 (1998) 1671–1678.

[85] A. Bilandzic, R. Snellings, S. Voloshin, Phys. Rev. C83 (2011) 044913.

[86] B. B. Back, et al., Phys. Rev. C72 (2005) 051901.

[87] E. L. Bratkovskaya, W. Cassing, H. Stöcker, Phys. Rev. C67 (2003) 054905.

[88] W. Cassing, E. L. Bratkovskaya, S. Juchem, Nucl. Phys. A674 (2000) 249.

[89] J. Geiss, W. Cassing, C. Greiner, Nucl. Phys. A644 (1998) 107.

[90] J. Beringer, et al., Phys. Rev. D86 (2012) 010001.

[91] H. Jones, M. Scadron, Annals Phys. 81 (1973) 1.

[92] G. Wolf, G. Batko, W. Cassing, U. Mosel, K. Niita, et al., Nucl. Phys. A517 (1990) 615.

[93] M. Krivoruchenko, A. Faessler, Phys. Rev. D65 (2002) 017502.

[94] M. Zetenyi, G. Wolf, Heavy Ion Phys. 17 (2003) 27.

[95] J. Koch, N. Ohtsuka, E. Moniz, Annals Phys. 154 (1984) 99.

[96] K. Haglin, C. Gale, V. Emel'yamnov, Phys. Rev. D47 (1993) 973.

[97] O. Linnyk, J. Phys. G38 (2011) 025105.

[98] O. Linnyk, et al., Phys. Rev. C88 (2013) 034904.

[99] P. B. Arnold, G. D. Moore, L. G. Yaffe, JHEP 0112 (2001) 009.

[100] E. L. Bratkovskaya, S. M. Kiselev, G. B. Sharkov, Phys. Rev. C78 (2008) 034905.

[101] O. Linnyk, W. Cassing, E. Bratkovskaya, Phys. Rev. C89 (2014) 034908.

[102] O. Linnyk, V. Konchakovski, T. Steinert, W. Cassing, E. Bratkovskaya, Phys. Rev. C92 (2015) 054914.

[103] W. Bauer, G. F. Bertsch, W. Cassing, U. Mosel, Phys. Rev. C34 (1986) 2127.

[104] W. Cassing, V. Metag, U. Mosel, K. Niita, Phys. Rept. 188 (1990) 363–449.

[105] C. Gale, J. Kapusta, Phys. Rev. C 35 (1987) 2107.

[106] C. Gale, J. Kapusta, Phys. Rev. C 38 (1988) 2659.

[107] C. Gale, J. Kapusta, Nucl. Phys. A 495 (1989) 423c.

[108] N. P. M. Holt, P. M. Hohler, R. Rapp, Nucl. Phys. A945 (2016) 1.

[109] S. Marzani, R. D. Ball, Nucl. Phys. B 814 (2009) 246.

[110] C.-Y. Wong, H. Wang, Phys. Rev. C 58 (1998) 376.

[111] O. Linnyk, S. Leupold, U. Mosel, Phys. Rev. D71 (2005) 034009.

[112] A. Adare, et al., Phys. Rev. C 81 (2010) 034911.

[113] O. Linnyk, S. Leupold, U. Mosel, Phys. Rev. D75 (2007) 014016.

[114] L. D. McLerran, T. Toimela, Phys. Rev. D31 (1985) 545.

[115] T. H. West, Comp. Phys. Comm. 77 (1993) 286.

[116] S. Wolfram, The Mathematica Book, Fifth Edition, Champaign, USA: Wolfram Media, 2003.

[117] J. Ghiglieri, J. Hong, A. Kurkela, E. Lu, G. D. Moore, D. Teaney, JHEP 05 (2013) 010.

[118] G. Vujanovic, et al., Nucl. Phys. A 932 (2014) 230.

[119] J. Ghiglieri, Nucl. Phys. A 932 (2014) 326.

[120] L. Landau, I. Pomeranchuk, Dokl. Akad. Nauk Ser. Fiz. 92 (1953) 535.

[121] L. Landau, I. Pomeranchuk, Dokl. Akad. Nauk Ser. Fiz. 92 (1953) 735.

[122] A. B. Migdal, Phys. Rev. 103 (1956) 1811.

[123] J. Cleymans, V. Goloviznin, K. Redlich, Phys. Rev. D47 (1993) 173.

[124] J. Cleymans, V. Goloviznin, K. Redlich, Phys. Lett. B319 (1993) 520.

[125] J. Cleymans, V. Goloviznin, K. Redlich, Phys. Rev. D47 (1993) 989.

[126] J. Knoll, R. Lenk, Nucl. Phys. A561 (1993) 501.

[127] Y. Yin, Phys. Rev. C90 (2014) 044903.

[128] F. Low, Phys. Rev. 110 (1958) 974.

[129] H. Eggers, R. Tabti, C. Gale, K. Haglin, Phys. Rev. D53 (1996) 4822.

[130] W. Liu, R. Rapp, Nucl. Phys. A796 (2007) 101.

[131] H. van Dam, M. Veltman, Nucl. Phys. B22 (1970) 397.

[132] V. Srinivasan, et al., Phys. Rev. D12 (1975) 681.

[133] S. Protopopescu, et al., Phys. Rev. D7 (1973) 1279.

[134] D. Aston, et al., Nucl. Phys. Proc. Suppl. 21 (1991) 105.

[135] K. Haglin, J. I. Kapusta, C. Gale, Phys. Lett. B224 (1989) 433.

[136] K. L. Haglin, J. Phys. G30 (2004) L27.

[137] J. I. Kapusta, P. Lichard, D. Seibert, Phys. Rev. D44 (1991) 2774.

[138] C. Song, C. M. Ko, C. Gale, Phys. Rev. D50 (1994) 1827.

[139] C. Song, Phys. Rev. C 47 (1993) 2861.

[140] O. Linnyk, et al., Phys. Rev. C84 (2011) 054917.

[141] O. Linnyk, W. Cassing, J. Manninen, E. Bratkovskaya, C. Ko, Phys. Rev. C85 (2012) 024910.

[142] E. L. Bratkovskaya, W. Cassing, O. Linnyk, Phys. Lett. B670 (2009) 428.

[143] ABBHHM, Phys. Rev. 175 (1968) 1669.

[144] M. Effenberger, E. Bratkovskaya, U. Mosel, Phys. Rev. C60 (1999) 044614.

[145] G.-Q. Li, C. Gale, Phys. Rev. C58 (1998) 2914–2927.

[146] H. van Hees, R. Rapp, Phys. Rev. Lett. 97 (2006) 102301.

[147] H. van Hees, R. Rapp, Nucl. Phys. A806 (2008) 339–387.

[148] O. Linnyk, E. L. Bratkovskaya, W. Cassing, Nucl. Phys. A830 (2009) 491c–494c.

[149] E. L. Bratkovskaya, W. Cassing, U. Mosel, Nucl. Phys. A686 (2001) 568.

[150] L. Kaptari, B. Kämpfer, Nucl. Phys. A764 (2006) 338.

[151] C. Ernst, S. Bass, M. Belkacem, H. Stöcker, W. Greiner, Phys. Rev. C58 (1998) 447.

[152] E. L. Bratkovskaya, C. M. Ko, Phys. Lett. B 445 (1999) 265.

[153] W. Cassing, Y. S. Golubeva, A. S. Iljinov, L. A. Kondratyuk, Phys. Lett. B 396 (1997) 26.

[154] Y. S. Golubeva, L. A. Kondratyuk, W. Cassing, Nucl. Phys. a 625 (1997) 832.

[155] R. Rapp (2002). arXiv:nucl-th/0204003.

[156] D. Trnka, et al., Phys. Rev. Lett. 94 (2005) 192303.

[157] T. Hatsuda, S. Lee, Phys. Rev. C 46 (1992) R34.

[158] G. E. Brown, M. Rho, Phys. Rev. Lett. 66 (1991) 2720.

[159] G. E. Brown, M. Rho, Phys. Rept.. 363 (2002) 85.

[160] V. Metag, Prog. Part. Nucl. Phys. 61 (2008) 245.

[161] E. Bratkovskaya, W. Cassing, Nucl. Phys. A807 (2008) 214.

[162] E. L. Bratkovskaya, W. Cassing, Nucl. Phys. A 619 (1997) 413.

[163] W. Cassing, E. L. Bratkovskaya, R. Rapp, J. Wambach, Phys. Rev. C 57 (1998) 916.

[164] G.-Q. Li, C. M. Ko, Nucl. Phys. A582 (1995) 731–748.

[165] L. Xiong, Z. Wu, C. Ko, J. Wu, Nucl. Phys. A512 (1990) 772.

[166] M. Schäfer, T. S. Biro, W. Cassing, U. Mosel, Phys. Lett. B221 (1989) 1–5.

[167] R. Shyam, U. Mosel, Phys. Rev. C67 (2003) 065202.

[168] S. Kondratyuk, O. Scholten, Nucl. Phys. A677 (2000) 396–422.

[169] F. de Jong, U. Mosel, Phys. Lett. B392 (1997) 273–277.

[170] M. Aggarwal, et al., Phys. Rev. Lett. 85 (2000) 3595.

[171] M. Aggarwal, et al. (2000) arXiv:nucl–ex/0006007.

[172] A. Adare, et al., Phys. Rev. Lett. 109 (2012) 122302.

[173] M. Wilde, Nucl. Phys. A904 (2013) 573c.

[174] E. V. Shuryak, Phys. Lett. B78 (1978) 150.

[175] E. V. Shuryak, Sov. J. Nucl. Phys. 28 (1978) 408. Yad. Fiz. 28 (1978) 796.

[176] R. Chatterjee, et al., Phys. Rev. Lett. 96 (2006) 202302.

[177] F.-M. Liu, T. Hirano, K. Werner, Y. Zhu, Nucl. Phys. A830 (2009) 587C.

[178] M. Dion, et al., J. Phys. G38 (2011) 124138.

[179] M. Dion, et al., Phys. Rev. C84 (2011) 064901.

[180] R. Chatterjee, et al., Phys. Rev. C 88 (2013) 034901.

[181] C. Shen, U. W. Heinz, J.-F. Paquet, C. Gale, Phys. Rev. C89 (2014) 044910.

[182] K. Dusling, Nucl. Phys. A839 (2010) 70.

[183] C. Shen, U. W. Heinz, J.-F. Paquet, I. Kozlov, C. Gale, Phys. Rev. C91 (2015) 024908.

[184] H. van Hees, M. He, R. Rapp, Nucl. Phys. A933 (2014) 256.

[185] C. Shen, U. Heinz, J.-F. Paquet, C. Gale, Nucl. Phys. A 932 (2014) 184.

[186] V. Goloviznin, A. Snigirev, G. Zinovjev, JETP Lett. 61 (2013) 054906.

[187] L. McLerran, B. Schenke, Nucl. Phys. A929 (2014) 71.

[188] A. Monnai, Phys. Rev. C90 (2014) 021901.

[189] F.-M. Liu, S.-X. Liu, Phys. Rev. C89 (2014) 034906.

[190] G. A. Almasi, G. Wolf, arXiv:1407.2047 (2014).

[191] A. Bzdak, V. Skokov, Phys. Rev. Lett. 110 (2013) 192301.

[192] K. Tuchin, Phys. Rev. C91 (2015) 014902.

[193] K. Tuchin, Phys. Rev. C87 (2013) 024912.

[194] A. Adare, et al., Phys. Rev. Lett. 104 (2010) 132301.

[195] A. Adare, et al., Phys. Rev. C91 (2015) 064904.

[196] A. Drees, Nucl. Phys. A910 (2013) 179.

[197] K. Dusling, I. Zahed, Phys. Rev. C82 (2010) 054909.

[198] S. Turbide, R. Rapp, C. Gale, Phys. Rev. C69 (2004) 014903.

[199] S. Mizuno, Nucl. Phys. A931 (2014) 686.

[200] H. van Hees, C. Gale, R. Rapp, Phys. Rev. C84 (2011) 054906.

[201] J. Adam, et al. (2015) arXiv:1509.07324.

[202] O. Linnyk, E. Bratkovskaya, W. Cassing, PoS (Baldin ISHEPP XXII), 084 (2015).

[203] M. Aggarwal, et al., Eur. Phys. J. C41 (2005) 287.

[204] D. Lohner, J. Phys. Conf. Ser. 446 (2013) 012028.

[205] L. Ruan, Nucl. Phys. A931 (2014) 185.

[206] F. Bock (2014). Direct-photon spectra and flow in PbPb collisions at the LHC measured with the ALICE experiment, contributed talk at the Quark Matter 2014, https://indico.cern.ch/event/219436/session/16/contribution/152.

[207] C. Shen, J.-F. Paquet, J. Liu, G. Denicol, U. Heinz, C. Gale, Nucl. Phys. A931 (2014) 675–680.

[208] A. Adare, et al. (2015) arXiv:1509.07758.

[209] J. Adams, et al., Phys. Rev. C 72 (2005) 014904.

[210] S. Adler, et al., Phys. Rev. Lett. 91 (2003) 182301.

[211] A. Morreale (2014) arXiv:1409.4456.

[212] L. E. Gordon, W. Vogelsang, Phys. Rev. D50 (1994) 1901–1916.

[213] H. Holopainen, S. Rasanen, K. J. Eskola, Phys. Rev. C84 (2011) 064903.

[214] L. McLerran, Phys. Part. Nucl. Lett. 8 (2011) 673.

[215] M. Chiu, et al., Nucl. Phys. A 900 (2013) 16.

[216] J.-P. Blaizot, et al., Nucl. Phys. A 904-905 (2013) 829c.

[217] C. Gale, et al., Phys. Rev. Lett. 110 (2013) 012302.

[218] G. Basar, D. Kharzeev, V. Skokov, Phys. Rev. Lett. 109 (2012) 202303.

[219] G. Basar, D. E. Kharzeev, E. V. Shuryak, Phys. Rev. C90 (2014) 014905.

[220] Y. Hidaka, S. Lin, R. D. Pisarski, D. Satow, V. V. Skokov, Nucl. Phys. A931 (2014) 681–685.

[221] B. Bannier, Nucl. Phys. A931 (2014) 1189.

[222] V. Voronyuk, et al., Phys. Rev. C83 (2011) 054911.

[223] V. Skokov, A. Y. Illarionov, V. Toneev, Int. J. Mod. Phys. A24 (2009) 5925.

[224] V. Skokov, J. Phys. Conf. Ser. 432 (2013) 012021.

[225] D. Peressounko, in: Proceedings, 30th International Workshop on High Energy Physics: Particle and Astroparticle Physics, Gravitation and Cosmology: Predictions, Observations and New Projects (IHEP 2014), pp. 181–188.

[226] R. Chatterjee, D. K. Srivastava, T. Renk, Nucl. Phys. A 931 (2014) 670.

[227] W. Wilson, et al., Phys. Rev. C57 (1998) 1865.

[228] W. Wilson, et al., Phys. Lett. B316 (1993) 245.

[229] R. Porter, et al., Phys. Rev. Lett. 79 (1997) 1229.

[230] G. Wolf, W. Cassing, U. Mosel, Nucl. Phys. A552 (1993) 549.

[231] E. Bratkovskaya, W. Cassing, U. Mosel, Phys. Lett. B376 (1996) 12.

[232] E. L. Bratkovskaya, W. Cassing, R. Rapp, J. Wambach, Nucl. Phys. A634 (1998) 168–189.

[233] C. Fuchs, A. Faessler, D. Cozma, B. Martemyanov, M. Krivoruchenko, Nucl. Phys. A755 (2005) 499.

[234] G. Agakishiev, et al., Phys. Lett. B663 (2008) 43–48.

[235] Y. Pachmayer, et al., J. Phys. G35 (2008) 104159.

[236] G. Agakishiev, et al., Phys. Lett. B690 (2010) 118.

[237] G. Agakishiev, et al., Phys. Rev. C84 (2011) 014902.

[238] G. Agakishiev, et al., Phys. Rev. C85 (2012) 054005.

[239] M. Thomere, C. Hartnack, G. Wolf, J. Aichelin, Phys. Rev. C75 (2007) 064902.

[240] H. Barz, B. Kämpfer, G. Wolf, M. Zetenyi, Open Nucl. Part. Phys. J. 3 (2010) 1.

[241] E. L. Bratkovskaya, et al., Phys. Rev. C87 (2013) 064907.

[242] B. Friman, C. Hohne, J. Knoll, S. Leupold, J. Randrup, R. Rapp, P. Senger, Lect. Notes Phys. 814 (2011).

[243] R. Arnaldi, et al., Eur. Phys. C 59 (2009) 607.

[244] R. Arnaldi, Phys. Rev. Lett. 96 (2006) 162302.

[245] J. Seixas, et al., J. Phys. G34 (2007) S1023.

[246] S. Damjanovic, Nucl. Phys. A 783 (2007) 327c.

[247] R. Arnaldi, Eur. Phys. J C61 (2009) 711.

[248] O. Linnyk, E. L. Bratkovskaya, W. Cassing, Int. J. Mod. Phys. E17 (2008) 1367.

[249] J. K. Nayak, J.-e. Alam, T. Hirano, S. Sarkar, B. Sinha, Phys. Rev. C85 (2012) 064906.

[250] A. Toia, Nucl. Phys. A774 (2006) 743.

[251] A. Toia, Eur. Phys. J. C49 (2007) 243.

[252] S. Afanasiev, et al. (2007) arXiv:0706.3034.

[253] A. Adare, et al. (2015) arXiv:1509.04667.

[254] J. Zhao, J. Phys. G38 (2011) 124134.

[255] P. Huck, Nucl. Phys. A931 (2014) c659.

[256] M. K. Köhler, Nucl. Phys. A931 (2014) c665.

[257] R. Rapp, Adv. High Energy Phys. 2013 (2013) 148253.

[258] O. Linnyk, et al., Phys. Rev. C87 (2013) 014905.

[259] G. Vujanovic, S. Young, B. Schenke, R. Rapp, S. Jeon, C. Gale, Phys. Rev. C89 (2014) 034904.